

Computer Simulation of Electronic Excitation in
Atomic Collision Cascades

vom Fachbereich Physik
der Universität Duisburg-Essen
zur Erlangung des akademischen Grades eines
Doktor der Naturwissenschaften
(Dr. rer. nat)
genehmigte
Dissertation
von
ANDREAS DUVENBECK aus Dorsten

Referent: Prof. Dr. A. Wucher
Korreferent: Prof. Dr. M. Schleberger

Tag der Einreichung: 20.12.2006
Tag der mündlichen Prüfung: 05.04.2007

Contents

1	Introduction	5
2	Fundamentals	11
2.1	Sputtering Models	11
2.1.1	Single Knock-On Regime	12
2.1.2	Linear Cascade Regime	12
2.1.3	Spike Regime	14
2.2	Formation of Ions in Sputtering	17
3	MD-Simulation	25
3.1	History of MD-Simulations	25
3.2	Today's Role of MD	26
3.3	MD-Simulation of Collision Cascades	28
3.3.1	Potentials	29
3.3.2	Numerical Integration	34
4	SPUT93	39
4.1	Model Crystal	40
4.2	Initial and Boundary Conditions	40
4.3	Impact Zone	41
4.4	Numerical Integration	43
4.5	Trajectory Analysis	43
4.6	Visualization	45
5	Linear Transport Model	49
5.1	Introduction	49
5.2	Description	51
5.2.1	Excitation: Principle	52
5.2.2	Excitation: Numerical Implementation	58
5.3	Application of the Model	59
5.3.1	Diffusion Coefficient	59
5.3.2	Application on Ag	61
5.4	Conclusion	68

6	Nonlinear Transport Model	69
6.1	Description of the Model	70
6.1.1	Diffusion Coefficient	70
6.1.2	Numerical Implementation	74
6.2	Application on Silver	76
6.3	Conclusion	82
7	Nonlinear Transport Model II	85
7.1	Description of the Model	85
7.2	Results	91
7.3	Conclusion	99
8	Energy Partitioning	101
8.1	Description of the Calculation	101
8.2	Results	101
8.3	Conclusion	105
9	Conclusion	107
A	Snapshots of Traj. 207	109

Chapter 1

Introduction

Everybody knows the game "pool billiard", which is most commonly played on a rectangular table with a length of 7 feet and a width of 3.5 feet. At the beginning of each game, a total number of nine or fifteen billiard balls are arranged next to each other in triangular shape near the foot of the table. The first player opens the match with the so-called "break shot", i.e. the white cue ball is shot into the triangle of billiard balls. As the cue ball crashes into one of the outer balls of the formation with sufficient velocity, the billiard balls are knocked out from their original positions and become scattered all over the table. This phenomenon can be explained in terms of a sequence of collisions among the billiard balls that is induced by the cue ball impact.

In analogy to this macroscopic billiard game, a rather similar scenario can be found in modern surface analysis, however, on a nanometer length scale: The secondary-ion-mass-spectrometry (SIMS) [1], one of the most versatile surface analysis techniques, may be considered as a kind of atomic billiard. More specifically, the SIMS technique uses energetic atomic particles as projectiles for the bombardment of a solid surface placed within a vacuum chamber. This bombardment induces a complex series of collisions among the near-surface target atoms. This sequence of collisions will in the following be referred to as "atomic collision cascade". The spatial evolution of this atomic collision cascade within the target material takes place within some picoseconds and typically amounts to a few nanometer depending on the bombarding conditions as well as on material parameters.

In the course of the collision cascade, some of the atoms set into motion may strike nearby particles located on the outermost atomic monolayers of the target thereby ejecting them off the surface into the vacuum. This process is usually called "sputtering".

The basic idea of the aforementioned SIMS technology is to use the flux of sputtered particles as a source of information on the microscopical stoichiometric structure in the proximity of the bombarded surface spot. By laterally varying the bombarding spot on the surface, the entire surface can be scanned and chemically analyzed.

However, the particle detection, which bases upon deflection in electric fields, is limited to those species that leave the surface in an *ionized* state. Due to the fact that the ionized fraction of the total flux of sputtered atoms often only amounts to a few percent or even less, the detection is often hampered by rather low signals. Moreover, it is well known, that the ionization probability of emitted particles does not only depend on the elementary species, but also on the local environment from which a particle leaves the surface. Therefore, the measured signals for different sputtered species do not necessarily represent the stoichiometric composition of the sample. In the literature, this phenomenon is known as the “Matrix Effect” in SIMS.

In order to circumvent this principal shortcoming of SIMS, there exist two different concepts.

(i) From an *experimental* point of view, one well-established approach is to employ certain techniques to ionize the neutral atoms directly after they have been ejected from the surface. This is most commonly realized either by means of photoionization using laser irradiation [2], or by electron impact ionization in a noble gas discharge chamber [3]. Both post-ionization techniques avoid complicated matrix effects in SIMS by decoupling the emission process and the ionization process from each other. However, both of the aforementioned techniques constitute a direct intervention into the nascent flux of sputtered particles, which may also consist of agglomerates of atoms such as molecules or clusters. The latter, in turn, may be fragmented during the post-ionization process and, therefore, significantly distort the measured mass spectrum. In particular, the quantitative analysis of spectra from organic samples is hampered by the complexity of the post-ionization induced fragmentation processes.

(ii) An alternative ansatz to tackle the quantification problem in SIMS is the *theoretical* account of the ionization probability of sputtered particles, which constitutes a vivid field of research and has been recently considered as

“the most urgent unsolved problem in atomic collisions in solids.”

R. BARAGIOLA in *Invited review: Some challenging unsolved problems in atomic collisions in solids*, Nucl. Instr. and Meth. B **237** (2005) 520

It is well known [4], that the ionization probability of particles ejected from the surface is directly related to the generation and transport of kinetically induced electronic excitations in the collision cascade. These substrate excitations do not only play a crucial role in the determination of the charge state of sputtered atoms, but also manifest, for instance, in ion induced kinetic electron emission [5] or in the experimental detection of hot electrons as internal tunnel currents in metal-insulator-metal junctions [6].

From a theoretical point of view, the two excitation mechanisms usually taken into account during keV-bombardment of *metals* are (i) *direct*

collisions of the projectile with conduction electrons close to the FERMI-level and (ii) *electron promotion* in close atomic collisions. The collective electron excitation induced by process (i), i.e. the direct collisional transfer of kinetic energy from both the projectile and low-energy recoils to electrons, can to first order be described in terms of the LINDHARD-SCHARFF-SCHIOTT (LSS) model [7] giving rise to a velocity-dependent friction force, whereas electron promotion is mostly treated within the FANO-LICHTEN model [8] of quasi-molecular orbital crossing.

Due to the fact that an ab-initio calculation of large scale particle dynamics, which would directly include electronic excitations, is still too complex and therefore not feasible for a sputtering scenario, several attempts [9, 10, 11, 12, 13] have been made to incorporate electronic excitation processes into standard computer simulations of atomic collision cascades¹.

However, in all of these approaches electrons only play a passive role *either* as a static medium acting as a friction force, which is calculated within the framework of the LSS-model or similar approaches employing local electron densities [14], leading to a slowing down of moving atomic particles, *or* as a non-relevant by-product accompanying the deep level core hole generation in a hard binary collision event [13]. In addition, it should be emphasized here that published models neither feature a simultaneous quantitative treatment of both excitation sources nor do they take into account any excitation energy transport.

In order to close this gap, the present thesis develops an alternative computer simulation concept, which treats the electronic energy losses of all moving atoms as excitation sources feeding energy into the electronic sub-system of the solid. The particle kinetics determining the excitation sources are delivered by classical molecular dynamics. The excitation energy calculations are combined with a diffusive transport model to describe the spread of excitation energy from the initial point of generation. Calculation results yield a space- and time-resolved excitation energy density profile $E(\vec{r}, t)$ within the volume affected by the atomic collision cascade. The distribution $E(\vec{r}, t)$ is then converted into an electron temperature T_e , which in a further step can be utilized to calculate the ionization probabilities of sputtered atoms using published theory.

The present thesis is organized as follows:

Chapter 2 gives an overview of the standard models for particle emission from ion-bombarded surfaces. The standard sputtering scenarios are introduced and discussed in terms of their validity taking into account recent experimental data as well as molecular dynamics simulations. In addition, we present a rather promising rate equation model for secondary

¹It should be mentioned here that there are many analytical approaches describing excitation and ionization. The shortcoming is that all these theories must describe the particle dynamics as a prerequisite to then describe the electronic excitation. All analytical descriptions of the collision dynamics, however, constitute rather crude approximations. Therefore, computer simulations appear to be the most promising approach for modeling substrate excitations and ionization processes in sputtering

ion formation originally proposed by Z. SROUBEK. The local electron temperature T_e at the position a particle is emitted from, enters this model as an unknown parameter. A numerical model calculation of the ionization probability of atoms ejected from a silver surface is carried out in order to exemplify the crucial role of substrate excitations parametrized by T_e .

Chapter 3 familiarizes the reader with basic concepts of molecular dynamics (MD) computer simulations. Starting from some notes on the historical development as well as the today's scientific role of MD-simulations, it will particularly be focused on the simulation of atomic collision cascades induced by keV particle impact.

Chapter 4 concentrates on the MD-software package SPUT93, which is utilized in our group to model the atomic particle kinetics in the collision cascade. For the model system 5 keV Ag \rightarrow Ag(111), as employed throughout the entire thesis, the choice of the interaction potential, the initial and boundary conditions as well as details on the numerical integration are outlined.

In **Chapter 5**, we develop a basic model that allows for the incorporation of electronic excitation into standard MD-simulations of atomic collision in metals. The physical excitation mechanism being employed is *electronic friction*, which is treated within the framework of the LINDHARD model. The transport of excitation energy from the original point of generation is described in terms of a linear diffusion equation with an excitation energy diffusivity D . The model is applied to calculate an excitation energy density profile $E(\vec{r}, t)$ for two different atomic collision cascades induced by the impact of a 5-keV silver atom onto an Ag(111) surface. We show that surface electron temperatures T_e of the order of thousands of Kelvin may be reached, thus indicating that the collective low-energy electronic excitations by electronic friction may significantly influence the charge state of atoms emitted from the surface.

In **Chapter 6** the model presented in chapter 5 is extended to account for the fact that the evolution of an atomic collision cascade leads to a space- and time-dependent reduction of crystallographic order within a solid. This is the reason why the electron mean-free path λ and, hence, the diffusivity D will exhibit pronounced temporal and spatial variations, too. In this case, the transport dynamics are no longer linear and demand for a more sophisticated numerical treatment of the corresponding transport equation. This numerical treatment including proper boundary conditions will be elaborated in this chapter. The extended model is then applied to calculate the dynamics of substrate excitations again for one selected impact event.

Chapter 7 deals with the incorporation of electron promotion processes into the excitation model. Electron promotion is considered as an additional source of excitation energy and treated in terms of diabatic correlation curves derived from ab-initio molecular orbital level calculations in combination with the LANDAU-ZENER curve crossing model.

In **Chapter 8** the excitation model developed so far is applied in order to calculate how the kinetic energy originally imparted into the solid is

distributed among the nuclear and electronic degrees of freedom of the solid. It will be shown that on the transient stage corresponding to the picosecond time scale about 60 % of the kinetic energy introduced into the surface is converted into electronic excitation.

Chapter 9 gives some concluding remarks.

Chapter 2

Fundamentals of Ion-Bombardment of Solids

The impact of an energetic particle (atom, ion, molecule, cluster, . . .) onto a solid initiates a complex sequence of atomic collisions within a near-surface region. During the temporal and spatial evolution of this atomic collision cascade, particles may be released from the surface. This phenomenon is usually called *sputtering* and has been investigated experimentally as well as theoretically for more than fifty years.

Even today, the physics of sputtering is a vivid field of ongoing research triggered by the needs of secondary-ion-mass-spectrometry (SIMS). This surface analysis technique uses ion-bombardment to release atoms from a target surface. If these emitted particles leave the surface in an ionized state, they are accessible by electric fields and, therefore, also detectable by means of time-of-flight mass spectrometry. Thus, it is obvious that a quantitative analysis of SIMS spectra prerequisites a fundamental understanding of sputtering as well as of the formation of secondary ions. This chapter gives a brief overview of the standard sputtering and ion-formation models.

2.1 Sputtering Models

The standard theory of sputtering has been elaborated by P. SIGMUND [15] in 1969. He considered the development of an atomic collision cascade as the underlying physical mechanism leading to sputtering. The projectile, which in the following will also be referred to as primary particle, produces secondary recoil atoms by a series of mostly elastic collisions. Those recoils, in turn, may also generate further recoil atoms. By this iterative process the cascade evolves in space and time. If an atom receives an adequate amount of momentum in surface direction to overcome the surface binding forces, it will be ejected from the surface into the gas phase.

The physical observable probably most attention has been drawn to is the sputtering yield Y , which is defined as the average number of sputtered

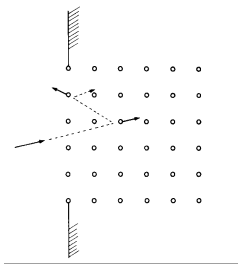


Figure 2.1: single knock-on regime [16]

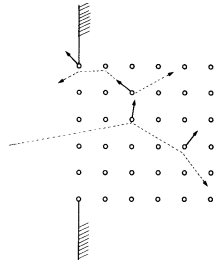


Figure 2.2: linear cascade regime [16]

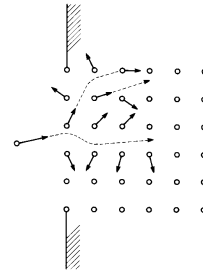


Figure 2.3: spike-regime [16]

particles per projectile impact.

In the following, the standard classification of atomic collision cascades will be briefly presented focusing on the particular prediction of the functional dependency of Y on system parameters like bombarding energy, incident angle, surface binding energy and, respectively, target characteristics. Figures 2.1, 2.2 and 2.3 give a schematic illustration of the three prototypes of collisional sputtering known as *single knock-on regime*, *linear cascade regime* and *spike regime*.

2.1.1 Single Knock-On Regime

In the *single knock-on regime* as sketched in Fig. 2.1, the collision cascade only consists of some insular binary encounters leading to distinct particle emission events, but not to the generation of a recoil cascade.

2.1.2 Linear Cascade Regime

In the *linear cascade regime* it is assumed that (i) the density of recoil atoms is such low that by far the majority of collisions involve one moving atom and one atom at rest and (ii) only one collision event takes place at the same time.

Under these presumptions, it is possible to treat the complex energy transfer processes by means of linearization¹ of the time-dependent BOLTZMANN transport equation [15] for a distribution function $H(E, \eta = \cos(\Theta), z)$ describing the distribution of recoils capable of overcoming a planar potential barrier of height U at depth z within the target. E and Θ denote the projectile energy and the angle of incidence, respectively. Additionally assuming the target to be amorphous and, thus, isotropic in the lower half plane, the solution of the BOLTZMANN equation can be expanded in terms of LEGENDRE polynomials leading to an analytical expression for the

¹At this point, it should be emphasized that the adjective *linear* in the term *linear collision cascade* does arise from this linearization procedure and *not* from the fact that the resulting yield formula (2.1) linearly scales with F_D as misleadingly pointed out by several authors.

average sputtering yield Y_{lin} given by [15]

$$Y_{lin} = H(E, \eta, z = 0) = \Lambda \cdot F_D(E, \Theta) \text{ with } \Lambda = \frac{0.042}{NU_0}, \quad (2.1)$$

where F_D denotes the kinetic energy deposited at the surface, U_0 is the average surface-binding energy and N represents the particle density of the target material. For perpendicular incidence and assuming inelastic effects to have only little influence on the sputtering yield, Eq. (2.1) can be further simplified into [17]

$$Y_{lin} = \frac{0.042 \cdot \alpha(m_1/m_2)S_n(E, Z_1, Z_2)}{NU_0}, \quad (2.2)$$

where S_n denotes the nuclear stopping power and Z_1 and Z_2 the nuclear charge of the projectile and target atoms. The parameter α represents a dimensionless function depending on the ratio of the mass m_1 of the projectile and the mass m_2 of a target atom.

In order to eliminate the explicit Z_1 - and Z_2 -dependence of S_n , one may introduce THOMAS-FERMI variables. In that formalism, any material dependency of the nuclear stopping power function is eliminated by a renormalization of the energy E in units of the Coulomb energy of two particles with atomic numbers $Z_{1,2}$ separated by an interatomic distance a_F known as the THOMAS-FERMI screening radius². The new energy variable is usually labeled ϵ and called *reduced energy*. In reduced energies the stopping power $S_n(E, Z_1, Z_2)$ translates for a screened Coulomb interaction potential to

$$S_n(E) = 4\pi a Z_1 Z_2 e^2 \frac{m_1}{m_1 + m_2} s_n(\epsilon) \quad (2.3)$$

with a universal function $s_n(\epsilon)$ (see Fig. 2.4) depending on the detailed choice of screening function. Combining Eqns. (2.3) and (2.2) one obtains the standard evaluation formula - also known as the SIGMUND formula - for the theoretical calculation of sputtering yields.

However, there exist many experimental data [19, 20, 21, 22] demonstrating that the sputtering yield Y of metals under bombardment with heavy ions systematically deviates from the values predicted by linear cascade theory. As an example, Figure 2.5 on page 15 shows experimental sputter yields for Cu, Ag and Au targets under bombardment with Ar, Xe, Au and Hg ions as a function of bombarding energy. The theoretically expected values according to the SIGMUND formula are included, too. One clearly finds that (i) the SIGMUND formula mostly underestimates the observed yields up to a factor of five, (ii) the measured yield maxima are shifted towards lower bombarding energies compared to linear cascade theory and (iii) the discrepancy between experiment and theory increases with the nuclear charge Z_1 of the projectile.

²The THOMAS-FERMI radius naturally depends on Z_1 and Z_2 , too. It is given by $a_F := 0.885 \cdot a_0 (Z_1^{2/3} + Z_2^{2/3})^{-1/2}$ with $a_0 = 0.529 \text{ \AA}$.

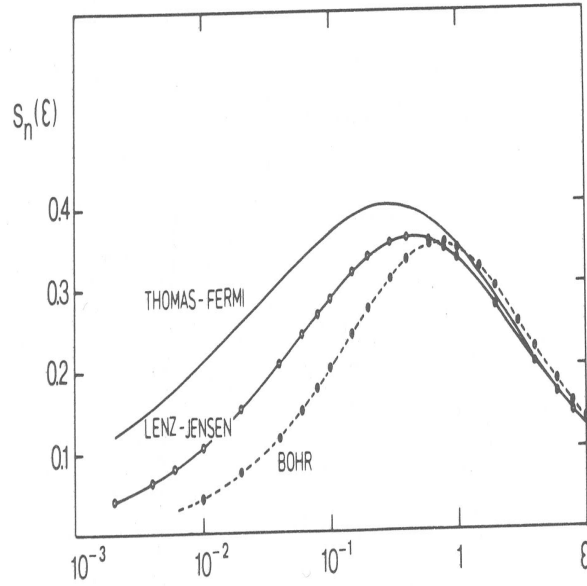


Figure 2.4: Nuclear stopping cross sections in THOMAS-FERMI variables. The three curves refer to three different screening functions for the Coulomb interaction. The one usually used for comparison of experimental and theoretical yield data is the THOMAS-FERMI curve (taken from Ref. [18]).

The reasons for those differences between experiment and linear cascade theory for heavy-ion bombarded metals have been worked out by H.H. ANDERSEN and H.L. BAY [23]. They attribute the deficiencies of SIGMUND's theory to the existence of *nonlinear effects* enhancing the sputter yield in the case of *high energy densities*, which, naturally, are in contradiction to the basic assumptions of the linear cascade model. In addition, they point out that for large ratios $m_2/m_1 \gg 1$, the α -function as proposed by P. SIGMUND leads to a systematic overestimation of Y due to a missing *surface correction term* and the neglect of *inelastic electronic energy losses*.

2.1.3 Spike Regime

Now, let us consider a target volume, in which the kinetic energy density is such high that by far the majority of particles are simultaneously in motion as depicted in Fig. 2.3. In this scenario, which is usually called a *spike regime*, the basic assumptions of the linear cascade are strongly violated. The sputtering from a spike volume has been described by P. SIGMUND and C. CLAUSSEN [24].

Their basic assumption is that the atoms in the spike volume resemble an ideal gas of high temperature and that the mechanism of particle emission is an evaporation process and, thus, not of collisional nature but of thermal nature. Using standard concepts from equilibrium thermodynamics, the transport of kinetic energy within the spike is modeled via

5.4 Sputtering

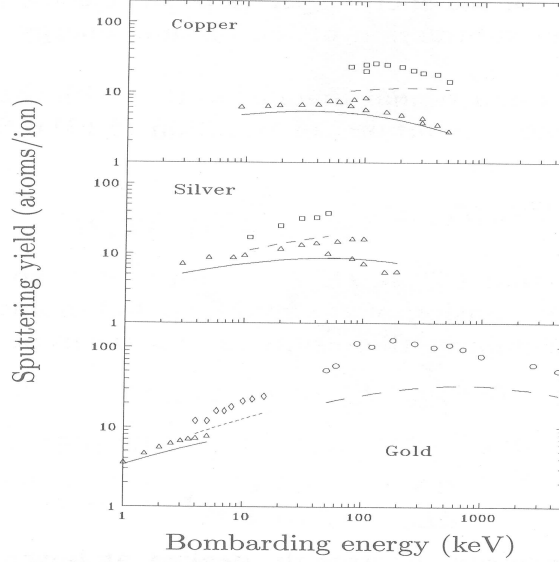


Figure 2.5: Experimental sputtering yield data for Ag targets (taken from Ref. [18]): open symbols correspond to experimental data, whereas the lines represent the predictions from linear cascade theory.

a diffusion equation for the lattice temperature T parameterizing the kinetic energy density. For the purpose of simplicity, P. SIGMUND and C. CLAUSSEN suppose the high-energy density region to be of cylindrical symmetry with respect to the primary particle track. This leads to the diffusion equation

$$\frac{\partial T(\rho, t)}{\partial t} = \nabla \cdot (\kappa(T(\rho, t)) \nabla T(\rho, t)) , \quad (2.4)$$

where ρ denotes the radial distance from the straight-lined trajectory of the projectile and $\kappa(T) \propto \sqrt{T}$ the lattice heat diffusivity. Employing the normalization

$$\frac{3}{2} N k_B \int d^2 \rho T(\rho, t) = F'_D \quad (2.5)$$

with N denoting the particle density and F'_D constituting the kinetic energy deposited per unit track length at the surface, the simultaneous solution of Eqns. (2.4) and (2.5) gives the temperature profile $T(\rho, t)$. This can then be used to calculate an evaporation rate $\Phi(T)$ (atoms per unit time and area). Once, $\Phi(T)$ is known, the total sputtering yield Y_{Spike} from a cylindrical spike volume is obtained by integrating the particle flux over the entire surface and time

$$Y_{Spike} = \int_0^\infty dt \int_0^\infty d\rho 2\pi\rho \Phi(T(\rho, t)) . \quad (2.6)$$

Under the assumption of a constant surface binding energy U and ap-

plying MAXWELL-BOLTZMANN ensemble statistics³ P. SIGMUND and C. CLAUSSEN arrive at the yield formula

$$Y_{Spike} = 0.036 \cdot (\lambda_0 a^2 F_D'^2 / U^2) \cdot g(U/k_B T_0) \text{ with } k_B T_0 = F_D' / 2\pi N \rho_0^2 \quad (2.7)$$

and a function g given by

$$g(\xi) = (1 + \xi - \xi^2) \cdot \exp(-\xi) + \xi^3 \int_{\xi}^{\infty} d\xi' \exp(-\xi') / \xi' . \quad (2.8)$$

The parameters T_0 and ρ_0 entering Eq. (2.7) represent the initial core temperature $T(t=0)$ and the average initial spike radius $\rho(t=0)$, respectively.

From Eq. (2.7), we conclude that for $U/k_B T_0 \ll 1$ the sputtering yield from a spike should be proportional to the *square* of the nuclear stopping power $F_D' = F_D(z=0) = N\alpha(dE/dx)_{z=0}$ and hence to the square of Y_{lin} . In addition, if we assume that the nuclear stopping power $dE/dx(n, E)$ of a cluster projectile consisting of n atoms corresponds to n times the nuclear stopping power of an atomic projectile of the identical element with the same impact velocity v , i.e.

$$\left(\frac{dE}{dx}(n, E) \right)_{nuc} = n \cdot \left(\frac{dE}{dx}(1, E/n) \right)_{nuc} , \quad (2.9)$$

then Eq. (2.7) implies that Y_{spike} increases at least with n^2 , while Y_{lin} is proportional to n at constant v .

Figure 2.6 monitors experimental sputtering yields [25] of gold and silver targets bombarded by Au_n ($n=1-13$) cluster projectiles with energies varying from 20 to 5000 keV/atom. The total yield Y is plotted as a function of $n \left(\frac{dE}{dx}(1, E/n) \right)_{nuc}$ for the different Au_n projectiles. The double-logarithmic representation of the data directly reveals that Y follows a line of slope 2 as long as the energy remains below the energy corresponding to the maximum of nuclear stopping power. Thus, in that energy regime the proportionality to the square of the nuclear stopping power, must be regarded as a signature of sputtering from a spike.

However, although there is at least good qualitative agreement of the predictions of the collisional spike model with experimentally observed sputtering yields under heavy-ion and cluster bombardment of metal surfaces, the validity of the presumption of thermodynamical equilibrium is highly questionable on a time scale of hundreds of fs. In addition, the temperature profile underlying Eq. (2.7) has been derived for an infinite medium. Hence, surface effects are not taken into account. Also the cylindrical track geometry and the neglect of (i) heat loss due to particle evaporation and (ii) electronic energy losses must be considered as an oversimplification.

In summary, we underline that in general the total sputtering yield Y is a sum of sputtering contributions from linear collision dynamics as well

³In this case, we have $\Phi(T) \propto \sqrt{T} \exp(-U/k_B T)$.

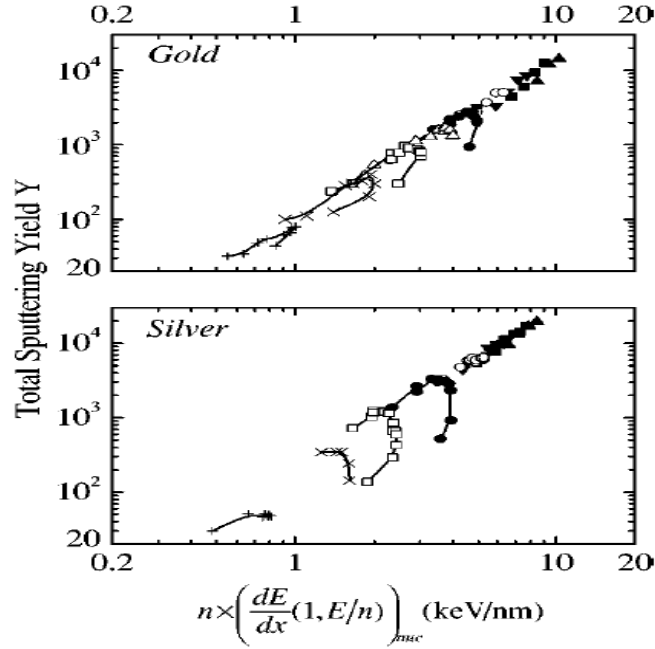


Figure 2.6: Gold and silver total sputtering yields Y , as a function of tabulated projectile nuclear stopping power $n \cdot (dE/dx)(1, E/n)_{nuc}$ and nuclearity n : + 1, × 2, □ 3, △ 4, ● 5, ○ 7, ▼ 9, ■ 11, ▲ 13 (taken from Ref. [25]).

as spike contributions, i.e.

$$Y_{tot} = Y_{lin} + Y_{spike} . \quad (2.10)$$

For silver self-bombarding conditions, the relative significance of both contributions has been theoretically assessed from molecular dynamics computer simulations, which are not restricted to equilibrium particle kinetics and allow for a rather accurate calculation of the central input parameter F'_D , ρ_0 and T_0 entering the spike model. For further discussion and results focusing on the validity of each of the two presented standard sputtering models, the reader is referred to Refs. [18, 23, 25, 26, 27, 28, 29, 30, 24, 31], for instance.

2.2 Formation of Ions in Sputtering

In the previous section, the two standard models for particle emission from ion-bombarded metal surfaces have been briefly introduced and discussed focusing on their predictions for the total sputtering yield Y . Both models only involve classical particle dynamics excluding any electronic degrees of freedom of the sputtered atoms.

However, it is well known that the total flux of sputtered particles is not exclusively composed of neutral atoms, but also consists of excited atoms or ions. Although the latter only constitute a rather small fraction of the total sputter yield Y , their experimental importance relates to their

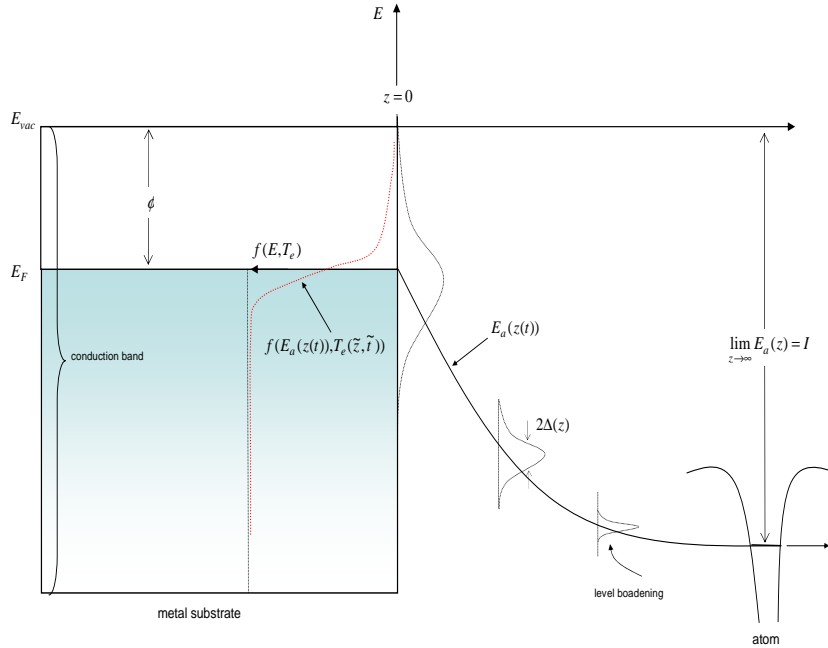


Figure 2.7: Schematic illustration of the electronic energy levels involved in secondary ion formation. On the left-hand side, the metal substrate is represented by its FERMI energy E_F and work function Φ . On the right-hand side, the energy E_a of the valence orbital of the atom - escaping from the surface with velocity v_{\perp} in normal direction - is drawn as a function of perpendicular distance $z = v_{\perp} t$ from the surface. The energy level E_a is broadened with decreasing distance from the surface. In the limiting case $z \rightarrow 0$, we assume the energy width $\Delta_a(z)$ to be equivalent to the width of the conduction band. The center of gravity of the energetic shape of the atomic valence level, we suppose to converge into the FERMI level.

either positive or negative charge state that makes them directly assessable to different kinds of mass spectrometry. The most popular of which is certainly the time-of-flight secondary-ion-mass-spectrometry (TOF-SIMS) [32] constituting the most sensitive of all the commonly-employed surface analytical techniques [33]. The drawback of this experimental method is that a quantitative stoichiometric evaluation of SIMS spectra requires the knowledge of the *ionization probability* for each sputtered species, which again significantly varies dependent on the bombarding conditions and the local chemical environment (“Matrix effect”) the sputtered particles originate from. In spite of this importance, the physical mechanisms leading to secondary ion formation are still poorly understood. The most general theoretical approach to secondary ion formation naturally bases upon a proper quantum mechanical treatment. For the applications we have in mind, the time-dependent ANDERSON model [34] seems to be the most appropriate one. In this approach, a non-degenerate atomic valence orbital $|a\rangle$ with energy ϵ_a is supposed to move with constant velocity v_{\perp} in direction parallel to the surface normal in z -direction (see Fig. 2.7). The electronic structure of the metal surface is represented by a continuum of conduction band

states $|k\rangle$ corresponding to energies ϵ_k .

Due to the (time-dependent) overlap of the wave functions $|a\rangle$ and $|k\rangle$ electronic transitions to and from the electronic band states are possible. These transitions induce an time-dependent, lifetime broadening

$$\Delta(t) = \frac{\pi}{\hbar} V_{ak}^2(t) \rho \quad \rho : \text{density of } |k\rangle \text{ states} \quad (2.11)$$

of the atomic energy level $\epsilon_a(t)$ according to FERMI'S Golden Rule. In Eq. (2.11) V_{ka} denotes the transition matrix element. The time-dependent Hamiltonian $H(t)$ for this system reads [35]

$$H(t) = \sum_k n_k(t) \epsilon_k + n_a(t) \epsilon_a(t) + \sum_k V_{ka}(t) (c_k^\dagger c_a + \text{H.c.}), \quad (2.12)$$

where n_k and n_a denote the occupation operators of $|k\rangle$ and $|a\rangle$, which can be expressed in terms of creation and annihilation operators c^\dagger and c as $\langle n_{a,k}(t) \rangle = \langle c_{a,k}^\dagger(t) c_{a,k}(t) \rangle$. Eq. (2.12) is usually treated in the so called "trajectory approximation", i.e. the atom is considered to follow a classical trajectory and the nuclear Hamiltonian is replaced by the corresponding Newtonian equation of motion. At each time step, the position of the atom enters the electronic Hamiltonian (2.12) as a fixed parameter.

Using HEISENBERG'S matrix mechanics instead of the SCHRÖDINGER'S wave function approach, the solution of Eq. (2.12) can be traced back to the solution of a set of first order differential equations of motion for the creation and annihilation operators. Analytical solutions of these equations require a variety of simplifying assumptions about, for instance, the time-dependence of the lifetime broadening $\Delta(t)$ and the hopping matrix elements $V_{ak}(t)$. Therefore, a more realistic and more flexible treatment of this quantum mechanical approach for the calculation of the expecting value of the ionization probability $\langle p \rangle = 1 - \langle n_a \rangle$ will call for a numerical treatment of the solution of the ANDERSON-Hamiltonian. Beside the fact that the numerical treatment of Eq. (2.12) may become rather tricky, it does not appear to be feasible to incorporate the dynamics of both the substrate and the sputtered particles into the description due to the complexity of the problem as pointed out by ZAVADIL [36]. In addition to this complexity argument, a more fundamental question arising in this context is, in how far substrate excitations - which are assumed to play a major role in the charge state formation of sputtered particles [4, 37, 38] and may be parametrized by a local effective electron temperature T_e - can principally be included at all, since T_e does not constitute a dynamical variable in the quantum mechanical approach.

In order to circumvent that shortcoming, we refer to the work of GEERLINGS ET AL. [39], which demonstrates - by means of an asymptotic expansion of the HEISENBERG'S equations of motion - that the quantum mechanical ANDERSON model presented above reduces to a simple semi-classical

rate equation for the occupation number $n_a(t)$ if $kT_e \gg \hbar\gamma v_\perp$ ⁴. The corresponding rate equation reads [4]

$$\frac{dn_a(t)}{dt} = -\Gamma \cdot n_a(t)(1 - f(E_a, T_e)) + \Gamma \cdot f(E_a, T_e)(1 - n_a(t)) \quad (2.13)$$

with $f(E_a, T_e)$ denoting the FERMI-DIRAC distribution at the energy E_a and at the electron temperature T_e . The parameter Γ is the transition rate. The first term on the right hand side of Eq. (2.13) represents resonant electron transitions from the atomic orbital into continuum states.

The change in the occupation number $n_a(t)$ per time unit due to this process is naturally proportional to the transition rate Γ and to the degree of occupation of the atomic valence level $|a\rangle$ itself times the probability to find an unoccupied state $|k\rangle$ at an energy E_a . The second term in Eq. (2.13) is the analogous one for the opposite direction, i.e. for a transition from the conduction band states into the atomic level. The transition rate Γ is usually taken as⁵ $\Gamma(t) = 2\Delta(t)/\hbar$. The crucial physical input parameters entering Eq. (2.13) are (i) the functional dependence of the energy of the atomic level on the perpendicular distance z from the surface, i.e. $E_a(z)$, and (ii) the variation $\Delta_a(z)$ of the width of the atomic valence level as a function of z . Once realistic parameterizations of $E_a(z)$ and $\Delta_a(z)$ are given, they can be directly converted into a time dependence via $z = z(t)$.

However, both parameterizations are associated with a high degree of uncertainty. Concerning $E_a(z)$ it is helpful to consider two limiting cases: Far outside the surface, i.e. at a distance where overlap effects of the valence electron with substrate atoms disappear, $E_a(z)$ will classically follow the image potential $E_a(z) = -e^2/4z$. For the limiting case $z \rightarrow 0$, the situation becomes by far more complicated, since the overlap of wave functions of the states $|a\rangle$ and $|k\rangle$ leads to a significant broadening $\Delta_a(z)$ of the atomic valence level E_a . NORSKOV and LUNDQUIST [41] as well as SROUBEK [4] propose among others that for $z \rightarrow 0$ the level $E_a(z)$ - which according to the aforementioned broadening has to be identified with the center of gravity of the density of states of $E_a(z=0)$ - must be “pegged at” [41] the FERMI level of the substrate.

In this case, we consequently have to assume that the corresponding width $\Delta_a(z=0)$ has to be identified with the energetic width of the conduction band of the metal substrate. A (linear) interpolation between the inner value $E_F = E_a(z=0)$ and the outer limit may then be considered as a first order approximation of $E_a(z)$. A probably more realistic approximation for $E_a(z)$ has been elaborated by STAUDT ET AL.. They assume the z -dependence far away from the surface to be determined by the image

⁴If we insert typical parameters ($T_e \approx 1000$ K, $\gamma = 1 \text{ \AA}^{-1}$, $v_\perp \approx 10^5$ m/s) for the bombarding conditions applied throughout the thesis, we get $kT_e/(\hbar\gamma v_\perp) \approx 14$. The parameter γ denotes the inverse fall-off length of the particle-substrate interaction

⁵This relation for Γ simply stems from the relation of uncertainty $\Delta E \cdot \Delta\tau \approx \hbar$ with $\Delta E := 2\Delta(t)$ and $\Delta\tau$ denoting a characteristic life time. Defining the transition rate Γ as $\Gamma = 1/\tau$, one arrives at $\Gamma(t) = 2\Delta(t)/\hbar$

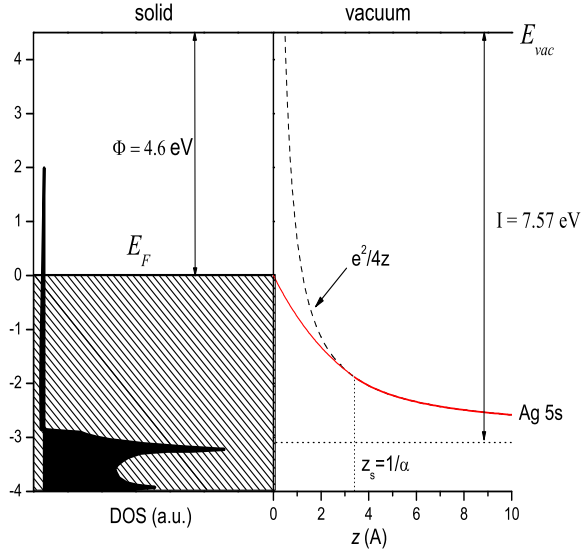


Figure 2.8: Energy levels relevant for electronic transitions between the conduction band of solid silver (left-hand side) and an outgoing silver atom (right) vs distance z from the surface. I : ionization potential for a ground silver atom; Φ : work function of solid silver; the solid line (red) represents the atomic valence level E_a for a silver ground state ion as calculated by Eqns. (2.14) and (2.15). The solid line shown on the left-hand side represents the calculated density of states (data partially taken from Ref. [40])

potential, too, and close to the surface to be given by [4, 40]

$$E_a(z) = E_a(\infty) + \{E_a(0) - E_a(\infty)\} \exp(-\alpha z), \quad (2.14)$$

where $E_a(\infty)$ corresponds to the energy of the state $|a\rangle$ at infinite distance from the surface. A simple calculation shows that one can arrive at a smooth transition between the aforementioned limits, i.e. the level position as well as its derivative can be matched at a distance $z_s = \alpha^{-1}$ [40]. For this particular case, α has to be chosen as [40]

$$\alpha = \frac{4[E_a(0) - E_a(\infty)] \exp(-1)}{e^2}. \quad (2.15)$$

Using values of 7.57 eV and 4.6 eV for the ionization potential $I = E_a(\infty)$ and the work function $\Phi = E_a(0)$ of silver, respectively, Eq. (2.15) yields $\alpha \approx 0.3 \text{ \AA}^{-1}$. Figure 2.8 illustrates the resulting level variation $E_a(z)$ (red line) in the context of the energy levels of solid silver. It becomes directly obvious that this parameterization of $E_a(z)$ will be a more realistic one than a simple linear interpolation, but, however, for large z the resulting level position falls below the image potential shift and therefore a proper matching of $E_a(z)$ and the long-distance limit cannot be realized.

Nevertheless, the parameterization of $E_a(z)$ resulting from Eqns. (2.14) and (2.15) may be applied to calculate the ionization probability for a

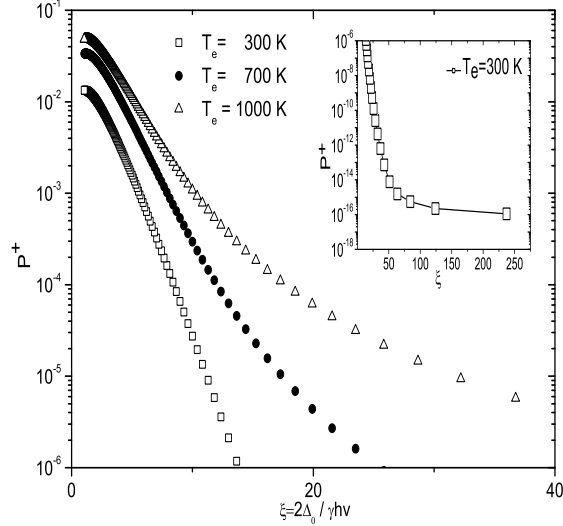


Figure 2.9: Model calculation of the ionization probability of Ag atoms sputtered from solid silver as a function of inverse emission velocity v and electron temperature T_e in the substrate.

silver atom - which is assumed to be emitted from the surface at $z = 0$ and therefrom to move with constant velocity v along the z -axis - as a function of v and electron temperature T_e from Eq. (2.13). In addition to this particular choice of $E_a(z)$, the level broadening we suppose to be given by $\Delta_a(z) = \Delta_0 \exp(-\gamma z)$, where Δ_0 denotes the initial width of the atomic valence level at $z = 0$, which we consider to be equivalent to the width of the conduction band of silver being approximately 10.8 eV [40]. The parameter γ is the inverse fall-off length of the interaction between the atomic orbital $|a\rangle$ and the substrate and γ chosen as 2 \AA^{-1} [4, 42].

Using these values the numerical solution of the rate equation (2.13) for an exemplary initial condition $n_a(t = 0) = 0$ yields the ionization probabilities P^+ illustrated in Fig. 2.9 as a function of $\xi = 2\Delta_0/\hbar\gamma v$. The particular representation of P^+ versus ξ has been chosen since the latter term is dimensionless and therefore simplifies the numerical treatment. In addition, the logarithm of ξ times $1/\gamma$ is the so called “freezing distance”, which in analytical approximations of the solution of Eq. (2.13) constitutes the distance at which electron transitions are most likely to occur. The parameter ξ varies from approximately 1 to 250, which is equivalent to an inverse velocity range from $0.4 \cdot 10^{-7} \text{ s/cm}$ to several 10^{-5} s/cm which is rather typical for sputtered particles. The different curves in Fig. 2.9 correspond to different electron temperatures $T_e=300 \text{ K}$, 700 K and 1000 K , respectively. First, considering only thermally excited substrates ($T_e=300 \text{ K}$), we observe a unrealistically steep exponential decrease of P^+ over several

orders of magnitude with decreasing particle velocity. In the limiting case $v \rightarrow 0$ the ionization probability converges towards $P^+ \approx 10^{-16}$. For higher electron temperatures $T_e=700$ K or $T_e=1000$ K, however, the ionization probabilities particularly for slow particles exceed those obtained at $T_e=300$ K by orders of magnitude.

Thus, without going into details, this exemplary numerical calculation clearly demonstrates the central role of the electron temperature for the ionization process of sputtered particles.

Chapter 3

Molecular Dynamics Simulation

A computer simulation method that follows the time evolution of a system of interacting particles by numerical integration of the classical Newtonian equations of motion is called *molecular dynamics* (MD).

Let us consider a set of N particles with time-dependent positions $\vec{r}_i(t)$ interacting among each other via a potential $V(\vec{r}_1(t), \vec{r}_2(t), \dots, \vec{r}_N(t))$. In the absence of additional external forces (frictional forces, external force fields, ...) the corresponding system of differential equations to be solved is given by

$$M_i \frac{d^2 \vec{r}_i(t)}{dt^2} = -\nabla_{\vec{r}_i} V(\vec{r}_1(t), \vec{r}_2(t), \dots, \vec{r}_N(t)) \quad \text{with } i = 1, \dots, N. \quad (3.1)$$

Provided that the initial conditions, i.e. the initial position $\vec{r}_i(t_0)$ and velocity $\vec{v}_i(t_0)$ of each particle, are known, Eqns. (3.1) can be numerically integrated to obtain $\vec{r}_i(t)$ for $t > t_0$, which is equivalent to the knowledge of the time evolution of the particle system. In the course of this thesis, the time evolution of a particle system will also be referred to as *trajectory*.

After this preliminary definition of molecular dynamics, the current chapter will start with a brief outline of the *history* of the MD-simulation technique followed by some examples of its *today's role* in natural sciences. Subsequent to that general overview, we will focus on the molecular dynamics simulation of *atomic collision cascades* with emphasis on *interaction potentials*, *boundary conditions* and *numerical integration* routines.

3.1 History of MD-Simulations

The origin of molecular dynamics simulations is naturally correlated with the development of microcomputers in the late 1950's. The first article reporting on molecular dynamic simulations has been published in 1957 by B. ALDER and T. WAINWRIGHT [43], who found that - even for a rather elementary model system of a few hundreds of hard-sphere particles with

exclusively repulsive interaction - a phase transition from liquid to solid may occur¹.

Shortly following this pioneering study, J. GIBSON ET AL. applied the MD-simulation method to investigate the dynamics of radiation damage using a particle system consisting of 500 copper atoms [44].

In 1964, A. RAHMAN studied a number of properties of liquid Ar using the LENNARD-JONES potential on a system containing 864 atoms. Three years later, L. VERLET, who also established the term “computer experiments” into the today’s scientific language use, published his famous work [45] on thermodynamical properties of LENNARD-JONES molecules and therein introduced the algorithmic bookkeeping concept of neighbor-lists as well as a new numerical integration scheme that both permit a speed-up in calculation time by orders of magnitude. Thus, beside the enhanced development of faster microprocessors in the 1970’s, L. VERLET provided the basis for the extension of molecular dynamics simulations to larger particle systems and more and more complex problems in all fields of physics. Concerning the MD-simulation of atomic collision cascades it is D.E. HARRISON whose works in the late 70’s [46, 47, 48] must be considered as the pioneering studies in that field.

3.2 Today’s Role of Molecular Dynamics

Due to the large popularity of MD-simulations it is not possible to review even a tiny subset of its applications covering nearly all disciplines of modern natural sciences. Therefore the purpose of this section is to mention only a few areas of current interest where MD has brought important contributions.

The research areas, the following examples are taken from, are *solid state physics*, *fluid dynamics*, *astrophysics* and, respectively, *biochemistry*. They have been selected not only to demonstrate the significant role of molecular dynamics in those particular fields, but also to show the enormous variety in the spatial dimensions as well as the simulated time scales of the investigated systems.

- **solid state physics:** Molecular dynamics are used to predict or test the mechanical and chemical stability of nanostructures [49] or, for instance, to study crack dynamics in notched solids on a microscopic scale using systems containing millions of particles [50].
- **astrophysics:** In this field of physics, MD-simulations are predominantly utilized to check the reliability of theoretical models. A rather prominent example for the applicability of molecular dynamics in astrophysical systems is the simulation of interacting spiral galaxies illustrated in Fig. 3.1(a).

¹At that time, this was a sensational result since it was believed that attractive forces should be necessary for this kind of phase transition.

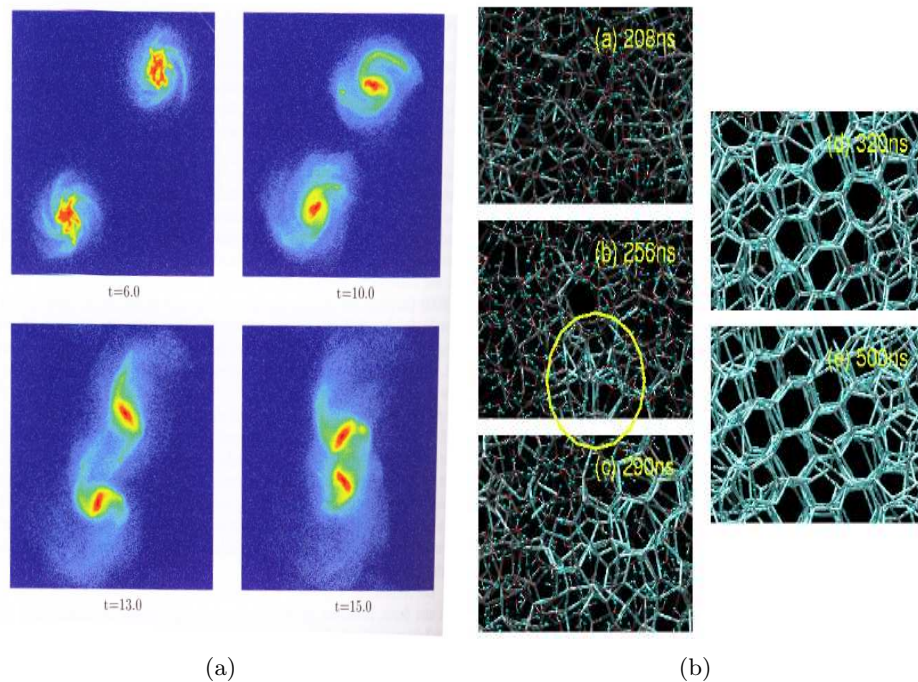


Figure 3.1: (a) MD-simulation of the dynamics of two colliding spiral galaxies [52]. The snapshots are taken at different times in direction parallel to the common rotational axis. The color code indicates the density of stars. (b) The hydrogen bond network structure of water at different times as calculated by molecular dynamics [51]. The temperature is artificially kept constant at 230 K.

- fluid dynamics:** MD-simulations give, for instance, an microscopic insight into hydrodynamic instabilities, complex fluids or, respectively, fluid alloys. Moreover, molecular dynamics constitute a tool for studying a large variety of phase transitions. Very recently, molecular dynamics simulations [51] have provided an atomistic level illustration (see Fig. 3.1(b)) of the water freezing and crystallization process which has never been successfully simulated on a computer, before.
- biochemistry:** MD-methods are routinely used to investigate the structure, dynamics and thermodynamics of biological molecules and their complexes. One finds molecular dynamics simulations of solvated proteins, protein-DNA complexes as well as lipid systems addressing a variety of problems including the thermodynamics of ligand binding and the folding of small proteins.

After this brief general introduction, the following section concentrates on molecular dynamics simulations of *atomic collision cascades* in solids.

3.3 MD-Simulation of Atomic Collision Cascades in Solids

The impact of a fast atomic particle upon a solid surface induces rapid movements of bulk particles in a near-surface region and thereby initiates a collision cascade as already discussed in the preceding chapter on sputtering basics. Although a major part of the progress in understanding sputtering phenomena came through analytical theory, computer simulations were already performed very early in the field of atom-solid-interactions since they provided a more detailed atomistic picture of the collision cascades.

Most of these computer schemes were based on the *binary-collision approximation* (BCA), which assumes that every moving atom only collides with one target atom at a time. In addition, it is presupposed that all collisions involve one moving atom and one atom at rest. Thus, BCA codes² implement the idea of a *linear collision cascade* on the atomic level. Although those BCA codes are rather fast - in particular for amorphous targets - and often give a very good representation of experimental results, there exist several drawbacks [57]. First, these codes need a large number of simulation parameters - such as the surface binding energy - the values of which are sometimes unclear and have to be fitted to experimental data. Second, and most important, the physical concept of the linear collision cascade breaks down whenever sputtering occurs from zones of high kinetic energy density (“spikes”) as achieved by polyatomic ion or massive cluster bombardment, for instance. In addition, BCA codes do not provide the opportunity to get a microscopic insight into the formation of sputtered clusters.

In contrast, the technique of molecular dynamics simulation allows for the treatment of all kinds of sputter phenomena, as long as the interatomic forces are realistically modeled [57]. In particular, it is no longer necessary to distinguish between different sputter regimes like *linear-cascade* regime, *single-knock-on* regime, *spike* regime, or respectively, *shock wave* scenarios [58].

In addition, MD simulations are not restricted to thermal equilibrium situations and therefore provide a unique tool to check the validity of those analytical sputtering theories which are based on equilibrium thermodynamics.

In recent MD-studies [28] of self sputtering phenomena at a silver surface under polyatomic ion-bombardment, for instance, the calculated nonlinear yield enhancements have been discussed in terms of the collisional spike model of P. SIGMUND and C. CLAUSSEN [24] and found to be in good agreement with theory. Moreover, it has been demonstrated that the MD-simulation provides a means to determine the spike core temperature T_0 and

²Prominent software packages for BCA simulations are TRIM [53], MARLOWE [54] and EVOLVE [55]. For a comprehensive treatment of BCA computer methods the reader is referred to Ref. [56].

the mean square of the spike area $\langle \rho_0^2 \rangle$, which both enter the analytical model as input parameters.

3.3.1 Potentials

The realism of a MD-simulation of sputtering, i.e. its ability to reproduce and to forecast physical sputtering phenomena in accordance with experimental data, mainly depends on the accuracy of the interatomic potential, which constitutes the by far most important input parameter for the calculation. In the context of sputtering, one usually distinguishes between *high-energy* potentials and *low-energy* potentials.

High-energy potentials describe the short-range *repulsive* interaction between atoms in close binary encounters, where in most cases the influence of surrounding atoms can be neglected. Thus, one may assume the interaction to be appropriately described by a *pair-potential*, which can generally be derived by quantum-mechanical dimer calculations in vacuum.

The *low-energy* potentials are predominantly used to describe the dynamics of particles around small deviations from their equilibrium positions. In the ideal case, the low-energy potential is flexible enough to describe the bondings in the solid as well as at the surface or even in gas-phase clusters. Due to the strongly non-local character of bondings, low-energy potentials usually consist of a repulsive pair interaction term as well as of a many-body potential term. The final potential function can then be parametrized via the coefficients of a polynomial spline function continuously connecting both contributions and fit to certain material properties. For metals the most common potentials are derived from *EAM-methods*³ [59, 60], *tight-binding calculations* [61] or *CEM-approaches*⁴ [62].

Pair Potentials

The simplest particle interactions result from direct isotropic forces between two particles. For that particular case, the total potential energy of a system with N particles at positions \vec{r}_i can be simply obtained by looping over all two-body interaction energies U_{ij} between particles i and j . Let $r_{ij} := |\vec{r}_i - \vec{r}_j|$ denote the interatomic separation between the i -th and the j -th atom, then the potential $V(\vec{r}_1, \dots, \vec{r}_N)$ is given by

$$V(\vec{r}_1, \dots, \vec{r}_N) = \sum_{i=1}^N \sum_{j=1, j>i}^N U_{ij}(r_{ij}) . \quad (3.2)$$

The inner sum is restricted to values $j > i$ in order to assure that each pair is counted only once. Prominent pair potentials often implemented into standard molecular dynamics codes for atomistic particle simulations are the

³Embedded Atom Method

⁴Corrected Effective Medium

- **Lennard-Jones-Potential**

$$U(r_{ij}) = 4\epsilon \left[\left(\frac{\sigma}{r_{ij}} \right)^{12} - \left(\frac{\sigma}{r_{ij}} \right)^6 \right], \quad m < n \quad (3.3)$$

This potential consists of an attractive tail ($\propto -1/r^6$), which originates from fluctuating dipole-dipole interactions (VAN DER WAALS forces), dominating at large distances, and a short-range repulsive interaction term⁵ ($\propto 1/r^{12}$) which is relevant at short interatomic distances when the wave functions of the two constituent atoms overlap and the energy increases due to PAULI'S principle. In view of the weak attractive part of the potential, the LENNARD-JONES potential applies best to atomic particles with closed valence-shells such as rare gases like Ar, Xe or Kr.

The parameters ϵ defining the depth of the potential and σ defining the equilibrium position are used to fit the physical properties of the material. However, regardless of how well this potential is able to model actual materials, the LENNARD-JONES potential nowadays constitutes a *standard potential* to use for all investigations where the focus is on fundamental issues, rather than studying the properties of a specific material [63].

- **Morse-Potential**

$$U(r_{ij}) = D \left(1 - e^{-a(r_{ij}-r_0)} \right)^2 \quad (3.4)$$

This potential has been developed by P.M. MORSE [64] in 1930. In contrast to the LENNARD-JONES potential, it is predominantly used for the modeling of intra-molecular forces. The parameter D denotes the dissociation energy of the bond; r_0 is the equilibrium distance and a constitutes a parameter depending on the frequency of molecular vibrations.

The significant role of that potential form as given by Eq. (3.4) arises from the fact that it allows an analytical solution of SCHRÖDINGER'S equation. A slightly modified version of the MORSE potential that differs from the one represented by Eq. (3.4) can also be used for the description of inter-molecular forces and allows a better fitting to *ab-initio* calculations than the LENNARD-JONES potential. Fits for a large variety of fcc- and bcc-metals have been elaborated by L.A. GIRIFALCO and V.G. WEIZER [65].

- **Born-Mayer-Potential**

$$U(r_{ij}) = Ae^{-r/a_0} \quad (3.5)$$

⁵The exponent "12" does not have any physical justification. It is usually chosen for the purpose of mathematical simplicity

The BORN-MAYER potential [66] belongs to the group of high-energy potentials and only provides repulsive interaction forces. The parameter A is a scaling parameter for the absolute energy values and a_0 defines the screening length of the potential.

Many-Body-Potentials

Although pair potentials provide a useful basis for a lot of principle studies, they are not an adequate means to account for specific bulk metal calculations. For those scenarios, it is necessary to introduce many-body-potentials which are usually of the form [52]

$$V(\vec{r}_1, \dots, \vec{r}_N) = \sum_{i=1}^N \left(\sum_{j>i}^N U_{ij}(r_{ij}) - S_i(r_{i1}, \dots, r_{iN}) \right) \quad (3.6)$$

with a repulsive pair-potential U_{ij} and an attractive contribution S_i . From the aforementioned group of many-body-potentials the embedded-atom-method as well as the corrected-effective-medium approach, which both match the above functional form, are to be presented in this context.

- **Embedded-Atom-Method**

M.S. DAW and M.I. BASKES [59, 60] have proposed a concept based on density-functional ideas, which is known as the *embedded-atom method* (EAM). The EAM has been successfully applied to study a large variety of physical phenomena (phase transition, crack formation, phonon spectra etc.) of bulk metals and their alloys. In particular, the EAM inherently incorporates the interfaces of a particle system and therefore realistically models surface reconstructions, sputtering processes as well as adsorption processes for a large variety of metallic system.

The main idea of the EAM is as follows: Every energy potential induces an electron density distribution. On the other hand, P. HOHENBERG and W. KOHN⁶ proved that the electron density uniquely determines the potential [67, 68]. The EAM adopts this principle in order to construct the potential from the electron density. Starting point is the observation that the total electron density in a metal is reasonably approximated by the linear superposition of the electron densities of the individual atoms, which are assumed to be radial symmetric. The energy V_i^{emb} of the i -th atom, which arises from the fact that the atom is embedded into the electron density of the metal (“host”), can then be written as

$$V_i^{emb} = F_i(\rho_i^{host}) = F_i \left(\sum_{j=1, j \neq i}^N \rho_j^{atom}(r_{ij}) \right) \quad (3.7)$$

⁶W. KOHN (together with J.A. POPLE) was awarded the Nobel Prize in 1998 for his pioneering works on density functional theory.

with ρ_i^{host} denoting the electron density at position \vec{r}_i without atom i itself⁷. In Eq. (3.7), F_i is called the “embedding function”. The total embedding energy of the system can then be obtained by looping over all atoms i , thus

$$V_{tot}^{emb} = \sum_{i=1}^N F_i \left(\rho_i^{host} \right) . \quad (3.8)$$

Note, that the embedding function F_i only depends on the specific type of atom i . In addition, the embedding potential (3.8) is combined with a purely repulsive pair interaction term

$$V_i^{pair} = \sum_{j=1, j \neq i}^N U_{ij}(r_{ij}) \text{ with } U_{ij} = \frac{Z_i(r_{ij})Z_j(r_{ij})}{r_{ij}} . \quad (3.9)$$

The functions Z can be considered as an effective charge which is constrained to be positive and to decrease monotonously with increasing interatomic separation. The assumed functional forms for F_i and Z_i are semi-empirical fit to bulk properties. For this purpose F_i and Z_i are usually taken as cubic spline functions whose coefficients are determined such that experimental observables like lattice constant, elastic properties or, respectively, sublimation energy are reproduced as well as possible.

The atomic electron density functions ρ_j^{atom} entering Eq. (3.7) can be obtained from HARTREE-FOCK calculations delivering the electronic wave function $\Psi_{i,n}$, where n denotes a set of quantum numbers defining the particular atomic orbital. For the electrostatic interaction among the atoms, the electrons in the outermost orbitals are of most importance. In the case of Ag ($[\text{Kr}]4d^{10}5s^1$) it is sufficient to take into account the $5s$ -electrons, which form the conduction band, as well as the d -electrons. For the resulting atomic electron density one gets

$$\rho_j^{atom}(r) = N_{5s} |\Psi_{j,5s}(r)|^2 + (N - N_{5s}) |\Psi_{j,4d}(r)|^2 , \quad (3.10)$$

where N denotes the total number of outer electrons and N_{5s} the empirically estimated contribution of the electrons in the s -orbital, which not necessarily coincides with the actual number of s -electrons. Fig. (3.2) shows the embedding functions F_i as a function of electron density as well as the effective charge $Z(R)$ (right-hand side) for Ag and Au as used in a series of MD sputtering simulations by A. WUCHER and B.J. GARRISON [69, 70, 71] in the early 1990's. In these works, the EAM potential

$$V^{EAM}(\vec{r}_1, \dots, \vec{r}_N) = \sum_{i=1}^N F_i \left(\sum_{j=1, j \neq i}^N \rho_j^{atom}(r_{ij}) \right) + \frac{1}{2} \sum_{i=1}^N \sum_{j=1, j \neq i}^N \frac{Z_i(r)Z_j(r)}{r} \quad (3.11)$$

was used to calculate, for instance, the equilibrium geometry and binding

⁷Note that this ansatz slightly differs from that proposed by P. HOHENBERG und W. KOHN who derive the potential from the electron density of *all* atoms.

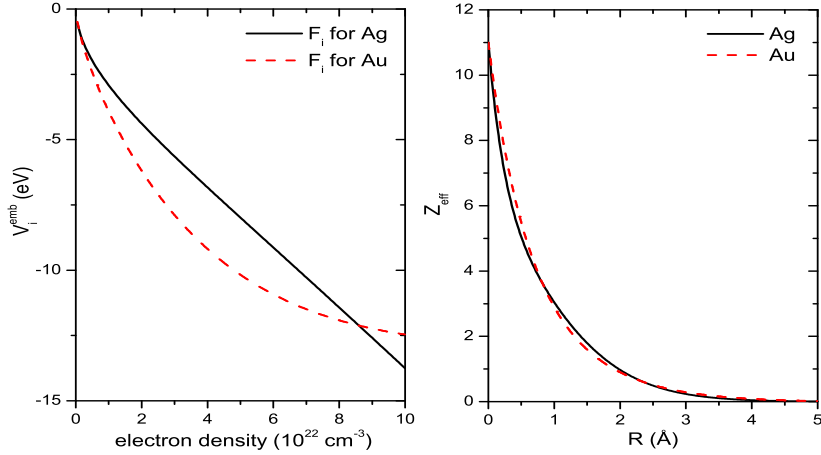


Figure 3.2: Left: Embedding functions $F_i(\rho_i^{\text{host}})$ for Ag (solid line) and Au (dashed line). Right: The effective charge $Z(R)$ used to define the pair interaction term (see Eq. (3.9)) for Ag and Au. Note that Z is in units of electron charge.

energies of small silver clusters. However, it turned out that the EAM potential fit to the bulk properties of solid silver significantly overestimates the binding energy of small Ag_n ($n=2-10$) in comparison to experimental or ab-initio data as illustrated in Fig. 3.3. In a subsequent study [72], A. WUCHER and B.J. GARRISON show that the so-called MD/MC-CEM potential developed by DEPRISTO and co-workers yields more reasonable values for the cluster binding energies than the EAM potential (\rightarrow Fig. 3.3) and, therefore, may provide a more accurate description of particle emission and cluster formation in the self-sputtering of silver.

- **MD/MC-CEM Potential**

The MD/MC-CEM potential⁸ has been designed by DEPRISTO ET AL. [62]. The functional form of this potential takes into account the interaction energy E_i of an atom i within an ensemble of N atoms as [75]

$$E_i = F_i \left(\rho_i = \sum_{j=1, j \neq i}^N \rho_j^{\text{atom}}(r_{ij}) \right) + \sum_{j \neq i}^N V_{ij}. \quad (3.12)$$

In Eq. (3.12), ρ_i denotes the total electron (“jellium”) density at the position of the i -th atom, which is obtained from the superposition of atomic electron densities. The term V_{ij} , which can be calculated from first principles, represents the pairwise Coulomb-interaction of nuclei and electrons of the atoms i and j . F_i denotes an embedding function, which for low densities is obtained by inverting the binding energy curve of an isolated

⁸Molecular Dynamics and Monte-Carlo-corrected effective medium

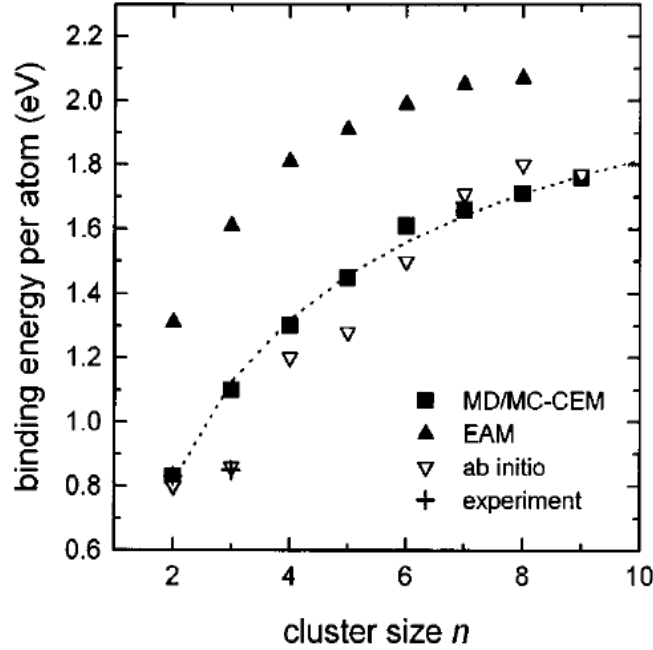


Figure 3.3: Binding energy per atom for small Ag_n clusters as a function of cluster size n as calculated from different potential types (Figure taken from Ref. [72], data partially taken from Refs. [73, 74]).

dimer obtained from ab-initio calculations. In the case of high jellium densities, F_i is fit to bulk properties in analogy to the EAM method. The final embedding function is then constructed by smoothly connecting the two curves in the intermediate region.

MD/MC-CEM potentials created this way have been successfully employed in a variety of MD simulations of keV ion bombardment of Ni(001), Rh(001) [78], Ag(111) [27, 28, 75, 29] or, very recently, Au(111) [77].

Figure 3.4, taken from Ref. [77], shows a compilation of experimental and calculated sputtering yields for an Au(111) surface under bombardment with Xe projectiles in the energy range from 0.1 eV to 200 keV. It is directly obvious that in the energy regime from 1-10 keV, which is the energy interval the present thesis focuses on, the MD/MC-CEM potential provides a more realistic description of the interaction among the cascade atoms than the EAM potential does. Moreover, the calculations carried out with the MD/MC-CEM potential are in excellent agreement with experimental results.

3.3.2 Numerical Integration

For the numerical time integration of the Newtonian equations of motion (3.1) there exist a large number of algorithms known as *Euler-*, *Verlet-* [45], *Leap-Frog-* [79], *Runge-Kutta-* and *Gear-*algorithm [80], for instance.

The schemes, which appear to be the most popular ones in the field of

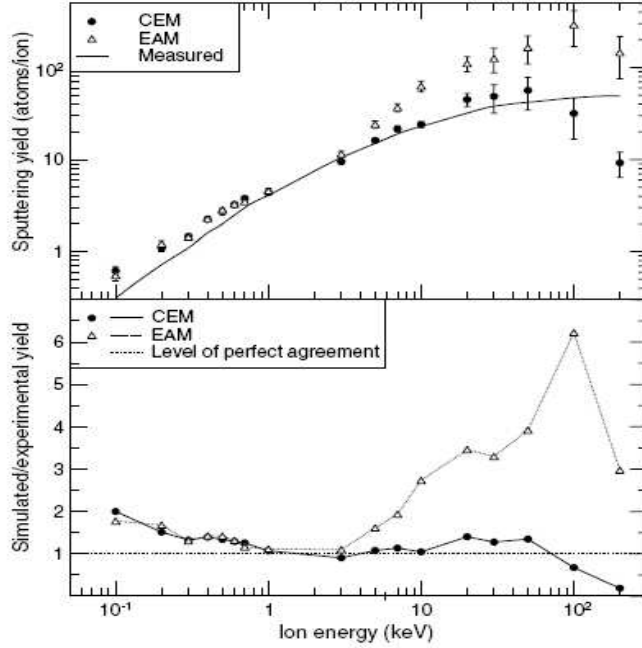


Figure 3.4: Comparison of experimental and MD-calculated sputtering yields of gold atoms from an Au(111) surface bombarded by Xe ions. The MD calculations have been carried out for the EAM potential as well as for the MD/MC-CEM potential for Au. The experimental values are extracted from Ref. [76]. The lower graph shows the ratio between simulated and measured yield data (Figure taken from Ref. [77]).

molecular dynamics, are the VERLET-algorithm and the GEAR-algorithm, which are to be briefly discussed in the following paragraphs.

- **Verlet-Algorithm**

The VERLET-algorithm is based on a third order Taylor expansion of the atomic positions $\vec{r}_i(t)$, which is done *twice* - once, in *forward* time direction and, additionally, once in *backward* time direction. Let Δt be the time step, then the corresponding expansions read [27]

$$\begin{aligned}\vec{r}_i(t + \Delta t) &= \vec{r}_i(t) + \frac{d\vec{r}_i(t)}{dt} \Delta t + \frac{1}{2} \frac{d^2\vec{r}_i(t)}{dt^2} (\Delta t)^2 + \frac{1}{6} \frac{d^3\vec{r}_i(t)}{dt^3} (\Delta t)^3 + o(t^4) \\ \vec{r}_i(t - \Delta t) &= \vec{r}_i(t) - \frac{d\vec{r}_i(t)}{dt} \Delta t + \frac{1}{2} \frac{d^2\vec{r}_i(t)}{dt^2} (\Delta t)^2 - \frac{1}{6} \frac{d^3\vec{r}_i(t)}{dt^3} (\Delta t)^3 + o(t^4).\end{aligned}$$

A simple addition of those two equations leads to the expression

$$\vec{r}_i(t + \Delta t) = 2\vec{r}_i(t) - \vec{r}_i(t - \Delta t) + \frac{d^2\vec{r}_i(t)}{dt^2} (\Delta t)^2 + o(t^4) \quad (3.13)$$

with a truncation error $\propto (\Delta t)^4$. Thus, according to Eq. (3.13), the position of the i -th atom at the next time step is calculated from the current position $\vec{r}_i(t)$, the position $\vec{r}_i(t - \Delta t)$ one time step before, as well as from the current acceleration $\vec{a}_i(t)$. The advantage of the VERLET-algorithm lies in its stability as well as in its simplicity to implement [63].

However, a look at Eq. (3.13) reveals that this numerical integration scheme does not inherently deliver the velocities $\vec{v}_i(t)$ of the particles. Therefore, it is not possible to directly calculate the total kinetic energy, for instance, which often constitutes an important means to check energy conservation during the time loop to ensure the proper working of the code. However, it is naturally possible to additionally calculate the velocities during each time step from the positions via

$$\vec{v}_i(t) = \frac{\vec{r}_i(t + \Delta t) - \vec{r}_i(t - \Delta t)}{2\Delta t}, \quad (3.14)$$

but the error for this expression scales with $(\Delta t)^2$ and no longer with $(\Delta t)^4$. This is the reason why more sophisticated variations of the VERLET-scheme have been developed (*Leap-Frog*-algorithm etc.).

• Gear's Predictor-Corrector-Algorithm

GEAR-Predictor-Corrector methods [80] constitute a class of numerical integration schemes, where the update of coordinates, velocities and higher derivatives is performed in two steps. In a first step, usually referred to as *predictor step*, the position $\vec{r}_i^p(t + \Delta t)$ and its derivatives are calculated from the values of the preceding time step by means of a m -th-order Taylor expansion as follows [81]:

$$\begin{aligned} \vec{r}_i^p(t + dt) &= \vec{r}_i(t) + \vec{v}_i(t)dt + \frac{1}{2!}\vec{a}_i(t)dt^2 + \dots + \frac{1}{m!}\frac{\partial^{(m-2)}}{\partial t^{(m-2)}}\vec{a}_i(t)dt^m \\ \vec{v}_i^p(t + dt) &= \vec{v}_i(t) + \vec{a}_i(t)dt + \frac{1}{2!}\frac{\partial}{\partial t}\vec{a}_i(t)dt^2 + \dots \\ \vec{a}_i^p(t + dt) &= \vec{a}_i(t) + \frac{\partial}{\partial t}\vec{a}_i(t)dt + \dots \\ &\vdots = \vdots \end{aligned} \quad (3.15)$$

On the other hand, it is possible to determine the accelerations at the next time step by employing the equations of motion to calculate the forces $\vec{F}_i(t + dt)$ at the predicted positions $\vec{r}_i^p(t + dt)$. This yields accelerations $\vec{\alpha}_i(t + dt) = \vec{F}_i(t + dt)/m_i$, which in general will deviate from the predicted accelerations $\vec{a}_i^p(t + dt)$.

The main idea of the predictor-corrector methods is to use this difference $\Delta\vec{\alpha}_i(t + dt) = \vec{\alpha}_i(t + dt) - \vec{a}_i^p(t + dt)$ as a measure for the error in the predictor step. This error is then used to correct the trajectory as follows [81]:

$$\begin{aligned} \vec{r}_i^c(t + dt) &= \vec{r}_i^p(t + dt) + c_0\Delta\vec{\alpha}_i(t + dt) \\ \vec{v}_i^c(t + dt) &= \vec{v}_i^p(t + dt) + c_1\Delta\vec{\alpha}_i(t + dt) \\ \vec{a}_i^c(t + dt) &= \vec{a}_i^p(t + dt) + c_2\Delta\vec{\alpha}_i(t + dt) \\ \frac{\partial}{\partial t}\vec{a}_i^c(t + dt) &= \frac{\partial}{\partial t}\vec{a}_i^p(t + dt) + c_3\Delta\vec{\alpha}_i(t + dt) \\ &\vdots = \vdots \end{aligned} \quad (3.16)$$

The coefficients c_i in Eqns. (3.16) depend on the order of the differential equation as well as of the order m of the predictor-corrector scheme. It can be shown [80], that the truncation error of the predictor-corrector algorithm is of the order $O(\Delta t^{m+1})$.

Moreover, detailed studies on numerical errors of numerical integration algorithms indicate that for the simulation of atomic collision processes, the predictor-corrector methods may constitute a more accurate choice than the VERLET-algorithm [82].

Chapter 4

The SPUT93 Sputtering Simulation Package

On the basis of the more general chapter on MD-simulations (\rightarrow chapter 3), this chapter concentrates on the particular software package SPUT93, which is used in our group to simulate sputtering processes induced by keV particle bombardment.

The origin of SPUT93 traces back to the works of D.E. HARRISON [47, 46] in the late 1970's, which have been continuously carried on in the research group of B.J. GARRISON¹ at Penn State University, who provided us with their software package.

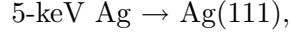
The structure of SPUT93 does not significantly differ from other popular MD codes like MDRANGE [83] or KALYPSO [84] used for the simulation of atomic collision cascades: At the beginning of a calculation a *model crystal* is either generated by an internal subroutine or read in from an external file containing the coordinates of all crystal atoms. Then, the projectile atom is positioned above the surface outside the surface interaction range and all particles of the system (crystal atoms + projectile) are assigned their initial velocities. Furthermore and most important, a *potential* for the interaction among the particles of the system has to be set up². Subsequently, the coupled differential equations of motion (3.1) are numerically integrated as long as a certain criterion for the termination of the trajectory integration is fulfilled. Once, the *numerical integration* has been finished, further subroutines or programs are usually applied to *analyze* the characteristics of the flux of sputtered particles or to create an *atomistic visualization* of the particle kinetics, for instance. In addition, each evaluation of simulation data should be accompanied by an *error estimation*.

The different types of potentials have already been focused on in the

¹<http://galilei.chem.psu.edu/>

²In the case of the presence of more than one atomic species interaction, potentials for all possible combinations of interactions among different types of particles have to be defined.

preceding chapter. Therefore, at this point, we only note that for our model system



we use a MD/MC-CEM potential [62] with a cut-off radius of 6.76 Å, which has been fit to the bulk properties of silver. Thus, the central issues remaining for discussion in this chapter are:

- selection and generation of a model crystal
- definition of initial and boundary conditions
- details on the numerical integration
- description of the analysis of the flux of sputtered particles
- error estimation
- notes on visualization

4.1 Model Crystal

SPUT93 contains an internal crystal generator capable to create a lattice structure with a monoatomic basis positioned at the center of each lattice site. Available crystallographic orientations are the (100)-, (110)- and (111)-direction. Concerning our model system, we employ a silver crystal-lite oriented in (111)-direction with a lattice constant of $a_0 = 4.09$ Å.

For the simulation of ion bombardment-induced collision cascades it is of utmost importance to choose a model crystal that is large enough to embed the entire cascade volume. Naturally, the spatial extent of the complex sequence of collisions strongly depends on the bombarding energy and, in addition, on the particular impact point on the surface, which the projectile is aimed at.

Table 4.1 shows a compilation of the standard crystal sizes which have been employed in previous works of our group [29, 28, 27]. For the purpose of the present study the crystal containing $N = 4500$ atoms has turned out to be the best trade-off between accuracy and cpu time, particularly in regard to the very time expensive space- and time-resolved calculation of the four dimensional excitation energy density profile $E(\vec{r}, t)$, which has been incorporated into SPUT93 in the course of the present thesis.

4.2 Initial and Boundary Conditions

Apart from the initial positions of all constituents of the model system, the numerical integration of the corresponding equations of motion requires the specification of the initial velocities of all particles. Due to the fact that the

Model crystal	x(Å)	z(Å)	y(Å)	layers
2295	43.4	42.6	21.3	9
4590	43.4	42.6	42.6	15
10500	72.3	73.4	35.4	15
24086	94.0	97.7	44.9	19

Table 4.1: Compilation of the crystal sizes used in this work and in previous studies of our group [29, 28, 27].

primary particle is assumed to impinge onto the surface under normal incidence, the initial velocity of the projectile is implicitly predefined via the selection of the bombarding energy. For all bulk atoms, the initial velocity is set to zero, i.e. the calculations are performed for an initial bulk temperature of $T_l = 0$ K. It should be emphasized here that this particular initial condition provides a perfect sixfold symmetry in the surface plane, which allows a more efficient selection of impact points, which the projectiles are aimed at (\rightarrow Section 4.3).

A further question arising in the preparation of the model system relates to the choice of boundary conditions for the model target. In many MD simulations, boundaries are artificially circumvented by employing periodic boundary conditions in one or more directions. This might be useful for annealing or relaxing surfaces as well as for simulations of low energy processes such as scattering or diffusion. However, periodic boundary conditions directly appear inappropriate for the simulation of sputtering by keV particle bombardment due to the large amount of crystal damage. Consequently, and in analogy to previous studies [29, 28, 27], we apply *open boundary conditions* at the boundary planes of the model crystal, i.e. particles are allowed to pass the planes without any restrictions. Possible systematic errors due to particle and energy loss have shown to be negligible [75] for the crystals and bombarding conditions applied here.

4.3 Impact Zone

Once, the complete model system has been initialized, for a constant bombarding energy the dynamics of the generated atomic collision cascade and the resulting sputtering yield Y only depends on the selected impact point on the surface. Previous MD simulations [75, 85] of keV bombardment of surfaces have revealed, however, that Y is not a smooth function of impact point, but a more or less random one characterized by “frequent abrupt changes” [85].

Under the presumption that the lattice temperature is zero, the aforementioned lateral symmetry (\rightarrow section 4.2) allows one to define the mean sputtering yield \bar{Y} as an average over the individual yields of different impact points distributed within an irreducible part of the lateral WIGNER-

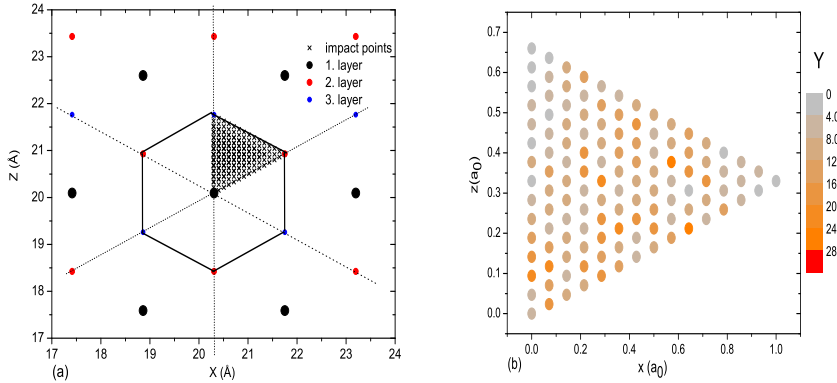


Figure 4.1: (a): Top view onto the three uppermost monolayers of the Ag(111) model crystallite. In addition, the two-dimensional WIGNER-SEITZ unit cell (solid line) as well as the 120 impact points are depicted. (b): Sputtering yield as a function of impact point for 5-keV Ag \rightarrow Ag(111) bombardment including electronic energy losses due to electronic friction and electron promotion. The average yield is $\bar{Y} \approx 9.7$.

SEITZ cell. The two-dimensional, WIGNER-SEITZ cell for the Ag(111) model crystallite is depicted in Fig. 4.1(a). For the particular choice of the set of impact points within that primitive surface area, several strategies³ have been investigated by COLLA and BRIEHL [86]. Adopting their proposal for the calculation of average sputtering yields, we arrange all impact points on a *regular grid* within our primitive cell to get the best estimate for the average yield, which is then calculated by

$$\bar{Y} = \frac{1}{N} \sum_{i=1}^N Y(\vec{r}_i) \quad (4.1)$$

with $Y(\vec{r}_i)$ denoting the individual yield of the i -th impact point located at \vec{r}_i in the irreducible surface cell. An upper estimate for the statistical error in the mean sputtering yield is given by $\pm\sigma/\sqrt{N}$, where σ denotes the square root of the variance [86].

As an example, Fig. 4.1(b) shows the individual yield Y for 120 different impact points for 5-keV Ag \rightarrow Ag(111) bombardment including electronic energy losses due to electronic friction and electron promotion. The average yield turned out to be $\bar{Y} \approx 9.7$ - a value that is significantly reduced in comparison to the calculations of LINDENBLATT ($\bar{Y} \approx 16$) using the identical impact points, but neglecting any electronic degrees of freedom. This calculated average yield reduction due to the incorporation of inelastic energy losses into molecular dynamics has already been observed by KÜRPICK [87] and is currently under investigation in our lab.

³These different strategies are known as “Monte-Carlo”, “fully stratified Monte-Carlo”, “regular grid” and “low discrepancy sequence strategy” according to COLLA and BRIEHL [86].

However, in the present thesis the analysis of electronic excitation in atomic collision cascades will be restricted to two individual trajectories which in the calculations without electronic excitations turned out to exhibit an extra-ordinairily high yield ($Y \approx 54$, Traj. 207) in one case and an average yield ($Y \approx 16$, Traj. 952) in the other case, respectively. Animation snapshots of trajectory 207 can be found in the appendix of the present work.

4.4 Numerical Integration

The integration routine implemented in SPUT93 to solve the system of differential equations (3.1) is a speed-optimized version of GEAR's Predictor-Corrector algorithm already introduced in section 3.3.2.

The speed optimization is realized by a dynamic adjustment of the time step Δt . This works as follows: For every integrator step the time step is maximized by specifying a maximum range d_{step} , which the fastest particle is allowed to move within Δt . Let v_{max}^m be the velocity of the fastest particle at the m -th time step. Then, an upper limit for the next time step is given by

$$\Delta t_{max}^{m+1} = \frac{d_{step}}{v_{max}^m}. \quad (4.2)$$

The time integration of the equations of motion will instantaneously be terminated, if a predefined total number N_{max} of time steps is exceeded. The integrator will also abandon the calculation, if a predefined maximum time of simulation t_{max} is passed. Hence, it should be taken care that t_{max} is chosen sufficiently large to ensure that the calculation does not finish when the sputtering process is still in progress. Although a detailed study [27] has shown that by far the majority of particles are emitted from the surface within the first ps, it is recommended to set $t_{max} \geq 3$ ps in order to be able to detect also clusters which are usually emitted in the very late stages of a cascade. The third condition for the termination of trajectory integration is an energy criterion that abandons the calculation when the total energy of every crystal atom has fallen below a certain threshold E_{thr} .

4.5 Trajectory Analysis

At the end of a trajectory integration, it has to be analyzed how many particles have been sputtered from the surface. Thereby, it is important that only those particles are identified as "sputtered", which have really been emitted from the surface into the gas phase in the course of the cascade. Particles, which left the crystal across one of the lateral crystal planes⁴ must not be taken into account for the total yield Y .

⁴This is possible due to the implementation of open boundary conditions (\rightarrow section 4.2).

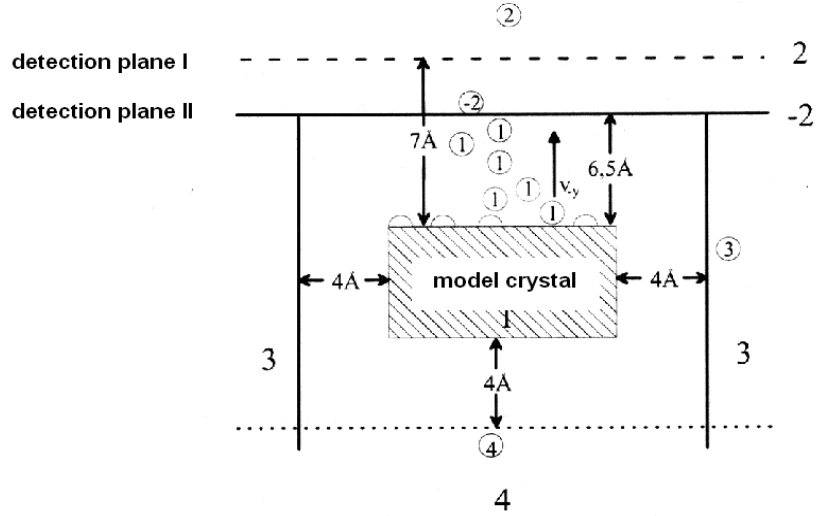


Figure 4.2: Detection scheme used to identify regularly as well as irregularly sputtered particles within SPUT93 [75].

For this purpose, each atom of the simulated system is assigned a flag variable `lcut` as illustrated in Fig. (4.2). Particles intersecting the virtual, sidewise boundary planes, which are attached to the crystal sides with an offset of 4 Å, are labeled with `lcut=3`, whereas for particles pervading the virtual detection plane at the bottom of the model crystallite the variable `lcut` is set to 4. Some Å above the gas-vacuum interface, two additional detection planes are aligned parallel to the surface in 6.5 Å and 7.0 Å distance, respectively. Atoms which are above the surface, but beneath the first detection plane are indexed with `lcut=1`; particles located in-between these two detection planes are classified via `lcut=-2` and, finally, particles being above the second plane are assigned `lcut=2`.

It should be annotated here, that the detection planes are arranged such that the first detection plane is still within the range of the MD/MC-CEM potential cut-off radius of 6.76 Å. The second detection plane, in contrast, is located slightly outside the interaction distance with the surface.

Atoms with `lcut=2` will be considered as “sputtered”, if they do not indirectly interact with the surface via other atoms or agglomerates of atoms between the second detection plane and the solid surface. Atoms with `lcut=-2` still interact with the surface and, therefore, have to undergo an additional energy check to determine if their kinetic energy is sufficient to overcome the surface barrier. If this is the case, the atom is also assumed to be sputtered.

In addition to this algorithm for identifying sputtered particles, SPUT93 includes a subroutine, which allows to scan the list of ejected atoms for “nascent” clusters, i.e. agglomerates of two or more atoms with negative total energy, which can then be subjected to a stability check against dissociation. Due to the fact that the present thesis does not deal with the

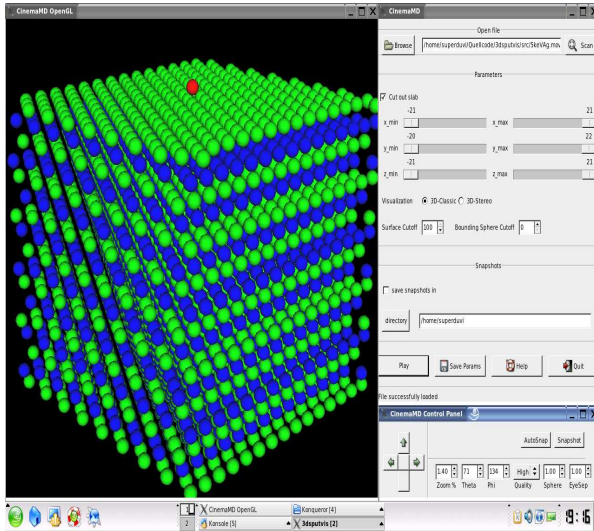


Figure 4.3: Screenshot of CINEMAMD and its graphical user interface. The visualized model crystallite consists of $N=4500$ atoms.

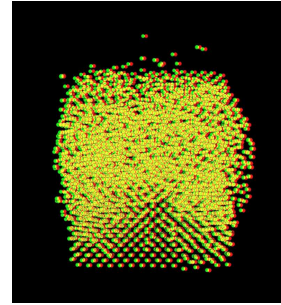


Figure 4.4: 3D-stereoscopic visualization mode of CINEMAMD.

analysis of cluster abundance in sputtering, the details of the aforementioned cluster identification scheme are not worked out here explicitly. For more details on this subject the reader is referred to Refs. [27, 75, 72].

4.6 Visualization

In this section, the visualization of SPUT93 data output using CINEMAMD will be presented. CINEMAMD constitutes a smart, open-source 3D-stereoscopic visualization program, which has been coded in the course of this thesis.

It has been developed in our group to study atomic collision cascades at surfaces. The program does not only allow to convert MD-simulation raw data into high-quality graphics for publication purposes - it moreover constitutes a nice supplementary presentation tool for interactively showing animated sequences directly calculated from the raw ascii data.

CINEMAMD has been implemented in ANSI-C employing the free MESA 3-D graphics library and should therefore work under every standard Unix/X11 platform. Concerning hardware requirements, the visualization software should run well on a standard notebook with a 2 GHz cpu and a 32 MB graphics card with 3D hardware acceleration. The complete program package including the source code, sample data and a detailed user's guide can be freely downloaded at the homepage of our workgroup⁵.

Figure 4.3 shows a screen snapshot of CinemaMD and its graphical user interface, which is divided into three sub-windows containing the *main*

⁵<http://www.ilp.physik.uni-essen.de/wucher/>

menu (upper right in Fig. 4.3), the *interactive control pad* (right bottom in Fig. 4.3) and, respectively, the *display window* (left-hand side in Fig. 4.3).

The main menu directly opens at program start and provides a comfortable selection menu to specify the particular data file to be visualized. The standard input file is in ASCII format and must contain an integer number in the first line defining the total number N of particles in the system. Each of the subsequent N rows specifies the x , y , and z -coordinates for one particular atom as well as its colorization, which is parametrized via three integers n_r, n_g, n_b constituting the RGB-color components. For the creation of animated sequences, just an arbitrary number of sets of N rows with atomic coordinates and color values has to be appended. Each set of N rows will then automatically be regarded as a new visualization time step. After an input file has been scanned, CINEMAMD offers two different display modes labeled as *3D-Classic* and *3D-Stereo*.

In the classic mode, all atoms are represented by spheres, which are first colorized according to their specific RGB-color values and, secondly, rendered in a three-dimensional perspective manner with diffuse illumination and specular reflectivity.

In order to achieve an even more realistic depth perception, CinemaMD provides a stereographic visualization mode (*3D-Stereo*). The realization of stereographics necessarily requires that two images (one for each eye) are presented independently to the eyes. If each of the two images constitutes the correct perspective projection from the point of view of the left and, respectively, the right eye, the human brain will merge them and give us a much stronger virtual illusion of three-dimensional depth as normally obtained with one single image. Although there exists quite a large amount of rather sophisticated high-end stereographic visualization tools as, for instance, LCD shutter glasses or even complete 3D-virtual reality environments, we use anaglyphs, in which the left and right eye images are made up of two different colors usually chosen as red and green/cyan. In doing so, simple paper 3D glasses with two color filters are sufficient to independently deliver each eye with its associated image. The low price of such glasses makes it possible to equip every person in the audience of a scientific talk with one exemplar and, thus, to let the complete audience participate in a “virtual reality” sputtering event.

Once the visualization is started from the main menu, the *control pad* allows to rotate the image, to change viewing angle and viewing distance, to adjust the sphere size as well as to change the display quality. The latter option may in particular be useful to accelerate image rotating in the case of large data sets with more than 100.000 particles per time step. The selectable display quality options are “low”, “medium” and “high”, respectively, and differ from each other in the number of faces each sphere is constructed of. In the high quality mode, for instance, each sphere consists of 10 subdivisions around the z -axis (similar to lines of longitude) as well as of 10 subdivisions around the x -axis (similar to lines of latitude), thus yielding a total of 100 faces to be rendered.

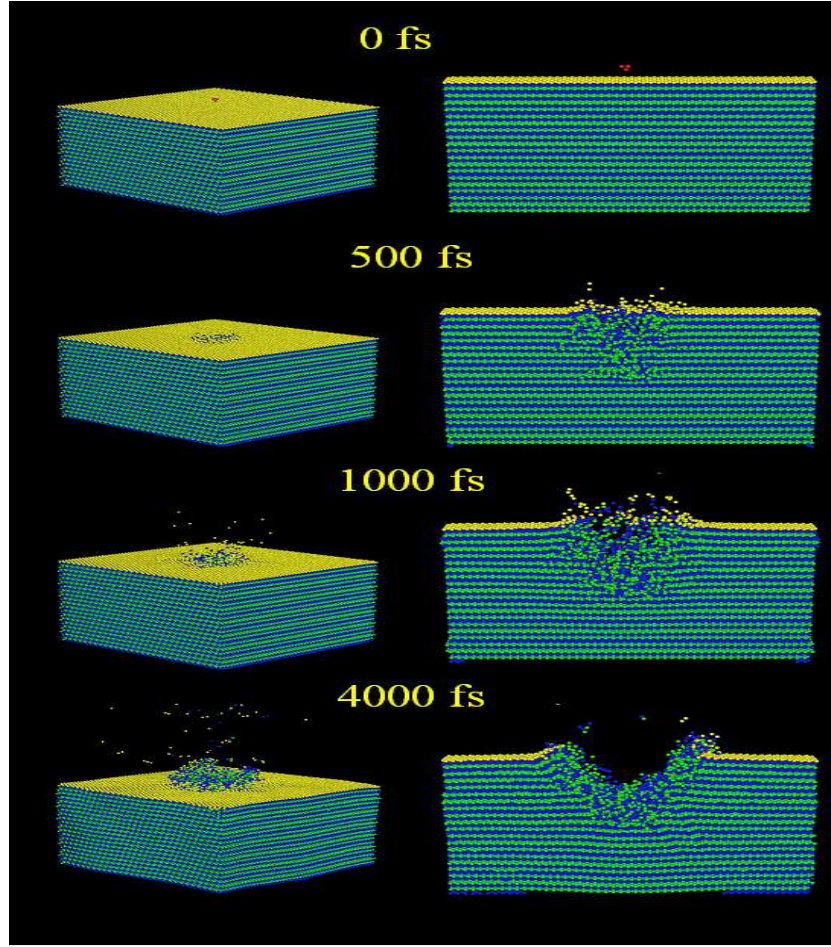


Figure 4.5: *left:* Snapshots of the particle dynamics after the impact of an 8-keV Ag_4 cluster onto an $\text{Ag}(111)$ model crystallite consisting of 120.000 atoms arranged in 40 layers; *right:* Central slab of the crystal with a thickness of 20 Å showing the crater formation.

As an example, Fig. 4.5 illustrates two different visualizations of the MD-calculated particle dynamics at distinct time steps (0 fs, 500 fs, 1 ps, 4 ps) after the impact of a 8-keV Ag_4 projectile onto an $\text{Ag}(111)$ model crystallite containing 120.000 atoms distributed over 40 layers. In Fig. 4.5 (left) the perspective view onto the complete crystal gives a nice atomistic picture of the sputtering process concerning the number of emitted particles, the origin of depth of sputtered particles or, for instance, the lateral extent of surface damage.

For a more detailed study of *interior* particle kinetics CINEMAMD provides a set of sliders to cut out certain subvolumes. This is exemplified in Fig. 4.5 (right) showing only the central slab of the crystal with a thickness of 20 Å. These snapshots give an insight into the dynamics of crater formation (see Ref. [26]) and, in addition, indicate a spike emission mechanism that closely resembles a free expansion process of a supercritically heated

subsurface volume [30, 88].

Chapter 5

Low-energy Electronic Excitation in Atomic Collision Cascades: A linear Transport Model based on Electronic Friction

In this chapter, we will present a computer simulation model of electronic excitation in atomic collision cascades induced by keV particle impact onto a metal surface. This model has already been published in the article *Computer simulation of low-energy electronic excitations in atomic collision cascades* by A. DUVENBECK, F. SROUBEK, Z. SROUBEK and A. WUCHER appeared in Nucl. Instr. and Meth. B **225**, 464 (2004). The following elaboration is largely taken from that reference. Direct citations are marked by quote signs.

5.1 Introduction of the Model

“In practically all MD implementations that have appeared so far, the electrons in collision cascades are assumed to play only a passive role as a medium which causes a slowing down of the atomic particles [89]. This electronic energy loss is normally included in an MD calculation as a friction force proportional to the velocity of the moving atom. In the calculation of the atomic motion, any possible electronic excitation caused by this friction is generally ignored because it does not influence the atom kinetics. Moreover, at least in a metallic substrate one can expect that any excitation in the electronic system dissipates rapidly in the bulk of the solid, thus making its effective magnitude relatively small.

In some instances, however, even a weak excitation may have strong effects. When atoms are emitted [...] from the surface as a consequence of

the collision cascade, their charge and excitation state is determined either by the escaping particles' rapid non-adiabatic passage through the surface barrier or by the electronic excitation in the solid which is transferred adiabatically to the particle. In this context, the term "surface barrier" denotes the region at and above the surface where the particle is still in an electronic interaction with the solid. In some cases, like in scattering of relatively fast projectiles that only shortly interact with the surface, the non-adiabatic processes are known to be dominant. In sputtering or multiple scattering events, however, the electronic excitation processes undergone by the substrate may play the decisive role in determining the charge and excitation states particularly of slow emitted particles.

In fact, one of the prevailing theoretical models describing the ionization probability of a sputtered atom uses the surface electron temperature T_e as a key parameter [90] as discussed in section 2.2. "It is important to note that this temperature is assumed to describe the local state of an electron gas that – due to the short, subpicosecond time scale on which collision cascades generally proceed – is not in thermal equilibrium with the atomic motion. The magnitude of T_e , which is an extremely critical parameter of the model since it enters the ionization probability exponentially, has only been crudely estimated [38].

Moreover, the localized nature of the impact process introducing kinetic energy into the system will cause T_e to vary as a function of time and position within the surface region disturbed by a collision cascade. So far, this time and space dependence has not been accounted for". It is the purpose of this chapter "to quantitatively estimate the amount of electronic excitation which is produced in such a cascade and how it distributes within the affected volume in the solid.

Unfortunately, a rigorous calculation of the electronic excitation – i.e. the ab initio solution of the SCHRÖDINGER equation of the complete system including the electronic degrees of freedom – is prohibitively complex and therefore still not practically possible. We therefore employ a number of severe semiclassical approximations in modeling the excitation processes.

One of these approximations is to treat the electronic sub-system of the solid as a quasi-free electron gas, whose excitation state may be described by an electronic temperature T_e [38].

The second approximation is concerned with the process by which the kinetic energy originally imparted into the solid is coupled to and converted into electronic excitation energy.

In principle, three different schemes can be used to include the excitation processes into the MD simulation of collision cascades. First, GARRISON and coworkers [9, 91, 10] as well as SHAPIRO ET AL. [92, 12] have invoked collisional excitation processes that are based on electron promotion in close binary encounters. This treatment has recently been utilized to describe the excitation of d-holes, thus leading to the emission of highly excited metastable atoms in sputtering [93, 13]. However, the underlying physics require fairly energetic collisions which are rare in a collision

cascade and lead to only few relatively large singular excitations.

Second, concepts of electron–phonon interaction have been employed to describe the energy transfer between atoms and electrons in the low-energy limit. In fact, these processes have been shown to largely dominate the energy loss experienced by the moving nuclei in the late stages of a collision cascade, where the average kinetic energy is below 1 eV/atom and the atomic motion can be assumed to follow thermal equilibrium dynamics [94, 95, 96, 97]. Moreover, it has been demonstrated that the description of effects like ion beam mixing or defect production ultimately requires the inclusion of electron–phonon coupling as an important cooling mechanism of the thermal spike [95]. The energy transfer can in this regime be described by a two-temperature model [96] as is also used to describe lattice heating occurring after rapid electronic excitation, for instance during electronic sputtering processes prevailing at very high projectile impact energies [98] or during laser ablation [99].

Due to the strong atomic disorder that is generally produced in an energetic collision cascade, however, the concept of phonons becomes questionable in the liquified region affected by such a cascade.” Moreover, the scope of the present thesis “is focused on relatively short time scales where collisional sputtering occurs. The relevant times are of the order of sub-ps and therefore too short to establish local thermal equilibrium. As a consequence, a two-temperature model as it is also used to describe the thermalization of a cascade [97] cannot be applied in this time range. Moreover, average energies well above 1 eV/atom are required in the cascade to permit the sputter ejection of atoms. In this energy regime, the energy transfer between moving atoms and electrons is dominated by the electronic stopping power of individual atoms in uncorrelated motion [94].”

Since the original motivation of the present study “concerns the description of mechanisms leading to the excitation or ionization of sputtered particles, we employ this concept to describe the kinetic excitation of the electronic system. For the sake of simplicity, the electronic stopping power will be treated in the frame of the dielectric function theory originally formulated by LINDHARD and SCHARFF [7].

In that way, the MD simulation naturally delivers the source term heating the electron gas as a function of location and time within the cascade volume. The temporal and spatial spread of the low-energy electronic excitations generated this way will be treated by means of a simple diffusive approach similar to that used in other work describing electronic relaxation in collision cascades [96] or during laser ablation [100].

5.2 Description of the Simulation

The classical MD simulation of particle dynamics has been described in detail” in chapter 3. In short, the solid is modeled by an fcc microcrystal of dimension $42 \times 42 \times 21 \text{ \AA}^3$ containing 2295 atoms arranged in 9 layers. “The

kinetics of the system are followed by solving the classical equations of motion for all atoms, the driving forces being derived from” the parametrized MD/MD-CEM many-body potential (\rightarrow section (3.3.1)) fit to the properties of silver.

“In order to eliminate the influence of chemical effects as much as possible, self-bombardment conditions were employed where the projectile hitting the surface is also composed of the same atoms as the solid. Since the CEM potential provides a realistic behavior at low interatomic distances, it can be directly applied to describe the interaction between the projectile and the substrate atoms as well.

As mentioned above and discussed in more detail below, the energy loss experienced by a moving atom due to its interaction with the electron system of the solid is introduced into the simulation by a friction term proportional to the velocity of the atom.”

The simulations are carried out for the model system

$$5\text{-keV Ag} \rightarrow \text{Ag}(111),$$

i.e. “for an Ag atom with a kinetic energy of 5 keV normally impinging onto an Ag(111) surface.

In order to gain information about averaged quantities that can be compared to experimental data, a total of 1225 trajectories were run with different impact points [...]” Without the inclusion of electronic excitation the average sputtering yield amounts to about 16 atoms/projectile, “a value which is in reasonably good agreement with experimental data collected for the self-sputtering of polycrystalline silver (≈ 13 atoms/projectile [101]).

Moreover, the simulated mass distribution of sputtered particles (atoms and clusters) closely resembles that measured experimentally [29]. We therefore conclude that the dynamics of the collision cascade initiated by the projectile impact are described reasonably well by the simulation.

5.2.1 Excitation: Principle

The electronic system in our model is represented by valence conduction electrons and inner shell electrons are neglected. The reason is that the inner shell electrons are not likely to be excited in low-energy cascades, particularly not at the later temporal stage, and their contribution to the charge state formation of emitted atoms is not important in the studied cases.

We thus assume that the Ag crystallite is embedded into an electron gas which is characterized by the FERMI energy ϵ_F and by the electron mean-free path λ . According to the prevailing theory of the electronic stopping power developed by LINDHARD and SCHARFF [7], the energy loss per unit traveled distance of the particle moving with the kinetic energy E_k is given by

$$\frac{dE_k}{dx} = -Kv, \quad (5.1)$$

where v is the velocity of the particle and the coefficient K is a parameter depending upon the solid in which the particle is moving. The corresponding time derivative of E_k is given by

$$\frac{dE_k}{dt} = -Kv^2 = -AE_k, \quad (5.2)$$

where A is a constant equal to $(2/M)K$ and M denotes the mass of the moving particle. From Eq. (5.2) we obtain the expression for the time derivative of the particle velocity, which yields friction in the molecular dynamics simulation, as

$$\frac{dv}{dt} = -\frac{A}{2}v. \quad (5.3)$$

Probably the most appropriate theoretical description of the friction in the free electron gas of our model is due to TRUBNIKOV and YAVLINSKII [102] but the LINDHARD-SCHARFF-SCHIOTT (LSS) inelastic loss model gives quantitatively similar results and is easier to handle numerically." Therefore, throughout the present thesis we use the LSS formula [7]

$$K = n_e \xi_\epsilon \times 8\pi e^2 a_0 \frac{Z_1 Z_2}{(Z_1^{2/3} + Z_2^{2/3})^{3/2}} \cdot \frac{1}{v_0} \quad (5.4)$$

for the evaluation of the friction parameters K and A , respectively. In Eq. (5.4) a_0 and v_0 denote the BOHR radius and BOHR velocity, respectively. The parameters Z_1 and Z_2 are the nuclear charge numbers of the ion and the bulk atoms; the parameter ξ_ϵ varies with Z_1 as approximately $\xi_\epsilon \approx Z_1^{1/6}$. The electron density of the target material is denoted as n_e . "The resulting value is $A = 2.88 \times 10^{12}$ 1/s [...] for an Ag atom moving in Ag metal.

The question remains whether the LINDHARD theory, which has originally been formulated for the stopping of keV atoms in matter, is in principle applicable to the case of low-energy recoil atoms with kinetic energies in the 10 eV range as are frequently found particularly in the later stage of a collision cascade. In order to examine this point in some detail, we compare the LSS stopping cross section obtained for H in Al according to Eq.(5.4) with recent ab-initio MD calculations [103]."

These ab-initio calculations have been carried out for an hydrogen atom approaching the threefold Al(111) fcc-hollow site with an initial kinetic energy of 2 eV, 5 eV or 10 eV, respectively. The time-dependent density functional theory and EHRENFEST equations were numerically integrated until the H-atom was reflected and returned to the same position above the surface where it started from. During the simulation, KOHN-SHAM wavefunctions and the coordinates of the particles are stored to be then relaxed electronically down onto the BORN-OPPENHEIMER surface at the corresponding frozen-in ionic positions $R(t)$. The difference in electronic total energy between the time-dependent calculation and the calculation employing fixed nuclei, equals the energy E_{diss} that is dissipated into electron-hole pairs [103].

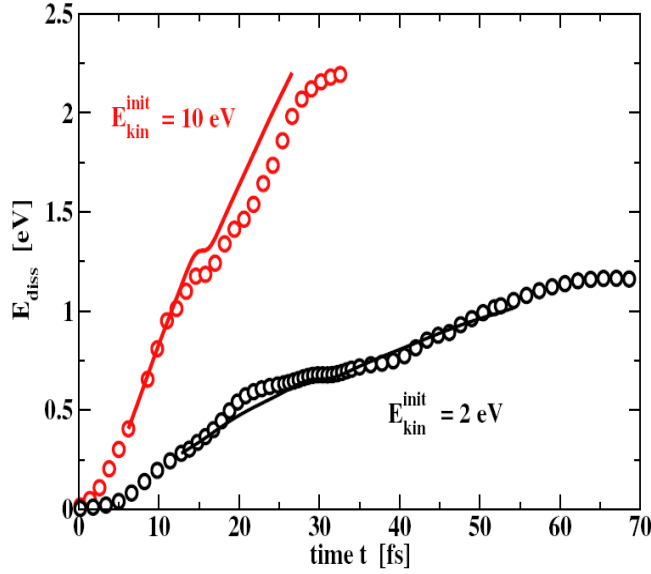


Figure 5.1: Energy E_{diss} dissipated into electron-hole pair excitations as a function of time for initial kinetic energies of the H-atom of 2 eV and 10 eV. The dissipated energy E_{diss} refers to a single hydrogen atom. The results from the TDDFT simulation (circles) are compared to the empirical bulk-friction ansatz (full lines) according to Eq. (5.2) (Figure taken from Ref. [103]).

This energy E_{diss} dissipated into electron-hole pair excitations is shown in Fig. 5.1 as a function of time for initial kinetic energies of the H-atom of 2 eV and 10 eV. The results from the TDDFT simulation (open symbols) are compared to the results obtained from the LSS-model according to Eq. (5.2) (solid lines).

First of all, we note that for both kinetic energies of the H-atom, a rather considerable total amount of excitation energy of about 1.2 eV ($E_{kin}=2$ eV) and 2.5 eV ($E_{kin}=10$ eV) has been transferred into the electronic subsystem. This observation is in good agreement with recent experimental studies on internal exoelectron emission [104], or chemicurrents [105], induced by hydrogen absorption on silver surfaces.

More important in our context is the finding that the predictions of the LINDHARD model are in excellent agreement with the TDDFT data. We may therefore conclude that the concept of electronic friction provides an accurate description of the conversion of kinetic energy into electronic excitation even for low-energy recoils.

“It should also be mentioned at this point that the (LINDHARD-) stopping power has been shown to significantly underestimate the energy transfer in the so-called electron phonon interaction (EPI) regime of a thermal spike at very low average kinetic energies [106, 7]. As shown in [7], the friction formulas (5.1) and (5.2) are also applicable in the EPI regime with, however, modified coefficients K and A .” In that sense, the electronic excitation calculated within the approach presented here, must be regarded

as a lower limit.

“[...] However, the present study concentrates on a relatively short time scale (<1 ps), where the average energy is still large enough to permit collisional sputter ejection of surface particles. In this regime, we expect the electronic stopping power (ESP) to still dominate over EPI processes (which come into play at larger times) and assume the error introduced by the neglect of EPI to be small.

The amount $dE(\vec{r}, t)$ of the electronic excitation energy $E(\vec{r}, t)$ that is transferred into the electronic system within dt by the i -th particle moving with the kinetic energy $E_k^i(t)$ at the point \vec{r}_i and at the time t is from Eq. (5.2) given by $AE_k^i(t)$, and hence

$$\frac{dE(\vec{r}, t)}{dt} = A \sum_i E_k^i(t) \cdot \delta(\vec{r}_i(t) - \vec{r}) . \quad (5.5)$$

The energy $E(\vec{r}, t)$, which is essentially the energy of electron-hole pairs in the metal excited by the moving particle, is rapidly carried away from the excitation spot by the motion of electron-hole pairs. This motion may be described approximately by a diffusion process characterized by a diffusion coefficient

$$D = \frac{1}{3} \lambda v_F , \quad (5.6)$$

where λ is the elastic mean-free path of the electrons and v_F denotes the FERMI velocity.

As discussed in Ref. [107] and also in detail below, we disregard in collision cascades the energy transfer from electrons to the lattice as a second order effect. In this case, the spatial and temporal development of $E(\vec{r}, t)$ is described by

$$\frac{\partial E(\vec{r}, t)}{\partial t} - D \nabla^2 E(\vec{r}, t) = \left(\frac{dE(\vec{r}, t)}{dt} \right)_s , \quad (5.7)$$

where the term on the right hand side is the source term, equal to Eq. (5.5) in our case.

Equation (5.7) describes the development of $E(\vec{r}, t)$ in time and space but does not give any information how the energy is distributed between the energy levels of the solid. As the electronic energy equipartition is not known, we assume in analogy with others [108, 96, 97, 109] , that $E(\vec{r}, t)$ rapidly thermalizes in the s-p conduction band at the electron temperature T_e . This assumption can be *qualitatively* justified by the fact that the excitation mechanism considered here produces a large amount of low-energy excitations, the distribution of which will be relatively close to a FERMI distribution to begin with.”

In order to give a more profound *quantitative* justification for the introduction of an electron temperature T_e , we again refer to our collaborative ab-initio study [103] on the H/Al(111) system. In this study, excitation spectra have been calculated as follows: First, the n KOHN-SHAM wave

functions $|\Psi_i(R(t), \vec{k})\rangle$ obtained from the TDDFT calculation are expanded in terms of the relaxed KOHN-SHAM eigenstates $|\phi_j(R(t), \vec{k})\rangle$ with eigenvalues $\epsilon_j(R(t), \vec{k})$, i.e.

$$|\Psi_i(\vec{k}, t)\rangle = \sum_j \langle \Psi_i(R(t), \vec{k}) | \phi_j(R(t), \vec{k}) \rangle |\phi_j(R(t), \vec{k})\rangle \text{ for } j = 1 \dots n. \quad (5.8)$$

Thus, for a given electron state $|k\rangle$ with wave vector \vec{k} and energy $\epsilon_{\vec{k}}$ the occupation number contribution $f_{\vec{k}}^{(i)}$ of the i -th KOHN-SHAM state to the total occupation number $n(\vec{k}, t)$ is then given by

$$f_{\vec{k}}^{(i)} = \sum_{\{j|\epsilon_j(R(t), \vec{k})=\epsilon_{\vec{k}}\}} \left| \langle \Psi_i(R(t), \vec{k}) | \phi_j(R(t), \vec{k}) \rangle \right|^2, \quad (5.9)$$

where the sum loops over all those KOHN-SHAM eigenstates, whose eigenenergies match $\epsilon_{\vec{k}}$. Consequently, the total occupation number of the state $|k\rangle$ is obtained by summing up the contribution from each $|\Psi_i(R(t), \vec{k})\rangle$

$$n(\vec{k}, t) = 2 \sum_i^n \sum_{\{j|\epsilon_j(R(t), \vec{k})=\epsilon_{\vec{k}}\}} \left| \langle \Psi_i(R(t), \vec{k}) | \phi_j(R(t), \vec{k}) \rangle \right|^2, \quad (5.10)$$

where the factor 2 originates from the consideration of spin degeneracy. Equation (5.10) represents a form of multidimensional \vec{k} -spectrum, which has to be converted into an energy spectrum $n(\epsilon, t)$. Thus, for a fixed energy ϵ the right hand side of Eq. (5.10) has to be summed up over all \vec{k} with $\epsilon_{\vec{k}} = \epsilon$. In order to get a continuous representation of $n(\epsilon, t)$, we instead integrate over the complete BRILLOUIN zone Ω_{BZ} of the reciprocal lattice and, in addition, replace the sets of summation indices by a δ -function $\delta(\epsilon - \epsilon_j(R(t), \vec{k}))$ yielding the equation

$$n(\epsilon, t) = 2 \sum_i^n \sum_j \int_{\Omega_{BZ}} \frac{d^3 \vec{k}}{\Omega_{BZ}} \left| \langle \Psi_i(R(t), \vec{k}) | \phi_j(R(t), \vec{k}) \rangle \right|^2 \times \delta(\epsilon - \epsilon_j(R(t), \vec{k})), \quad (5.11)$$

which can be integrated numerically.

Snapshots of the resulting electronic excitation spectra $n(\epsilon, t) - n^{BO}(\epsilon, R(t))$ are shown in Fig. 5.2 using a single logarithmic scale. The snapshots taken at $t_1 = 13$ fs, $t_2 = 23$ fs, $t_3 = 29$ fs and $t_4 = 75$ fs, respectively, roughly coincide with the points in time where the H-atom penetrates the first ($\rightarrow t_1$) and second ($\rightarrow t_2$) atomic Al-layer, where the H-atom is reflected at the third layer ($\rightarrow t_3$) and where the H-atom reaches an outer (on the vacuum side) reflection point ($\rightarrow t_4$). It should be annotated here, that the obtained spectra have been (i) convoluted with a Gaussian of 50 meV width in order to smoothen the energy gaps between the discrete eigenstates contained in the simulation volume and (ii) multiplied with -1.

Inspecting Fig. 5.2 the successive build-up of the electron-hole pair excitation in the Al metal becomes obvious. Looking particularly at the energy

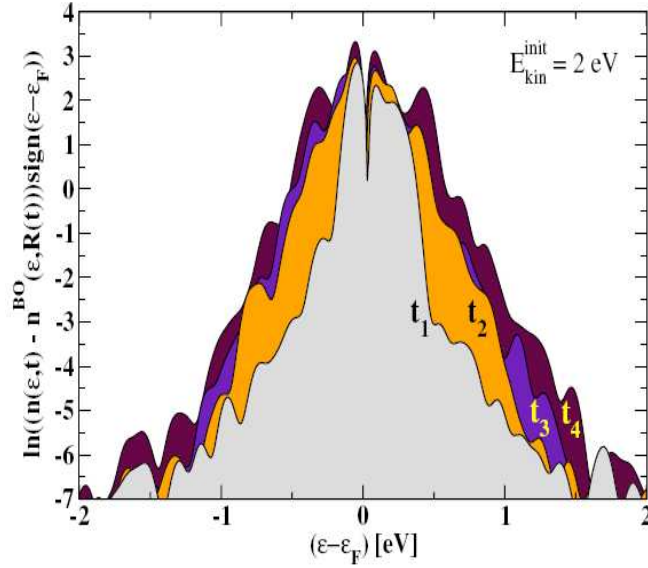


Figure 5.2: Snapshots ($t_1 = 13$ fs, $t_2 = 23$ fs, $t_3 = 29$ fs and $t_4 = 75$ fs) of the time evolution of the excitation spectra for holes and electrons obtained for a 2 eV H-atom impinging onto the Al(111) surface via the fcc-hollow site. Note that the densities of states $n(\epsilon, t)$ and $n^{BO}(\epsilon, R(t))$ have been convoluted with a Gaussian of 50 meV width (Figure taken from Ref. [103]).

range in the proximity of the FERMI energy, it is seen that the excitation spectrum is naturally dominated by low-energy excitations closely above and below the FERMI level. However, in the context of the incorporation of an effective electron temperature T_e into our model description, the important observation from Fig. 5.2 is that the calculated excitation energy distribution of hot electrons and holes generated by atomic motion in solids closely resembles a FERMI-DIRAC distribution and therefore may be parametrized by a fictitious electron temperature T_e [103], which turns out to be almost identical for holes and electrons.

At this point, we put emphasis on the fact that the FERMI-like excitation spectrum is obtained generically. This means that the concept of an effective electron temperature T_e does not prerequisite electron-electron scattering as a sort of equilibration mechanism as recently postulated by VEKSLER [110].

In conclusion, “we describe the excitation state of the electron system by a position and time-dependent electron temperature $T_e(\vec{r}, t)$ which is estimated from the electronic specific heat [111]

$$c_e = \frac{\pi^2}{2} \cdot n_e \cdot k_B \cdot \frac{T_e}{T_F} =: C \cdot T_e \quad (5.12)$$

(k_B : BOLTZMANN constant, n_e : electron density, T_F : FERMI temperature) of the conduction electrons of the solid as

$$T_e(\vec{r}, t) = \sqrt{\frac{2}{C} E(\vec{r}, t)} . \quad (5.13)$$

Therefore, once $E_k(\vec{r}, t)$ is known from the molecular dynamics simulation, we can obtain from Eqns. (5.7) and (5.13) the values of T_e at any point \vec{r} and time t . The numerical implementation of this concept is described in the following section.”

5.2.2 Excitation: Numerical Implementation

As already outlined in section 5.2.1, “we assume for the cascade simulation that the crystallites are embedded in a homogeneous infinite electron gas. This approximation simplifies the calculation, but because the excitations can spread in all directions it also slightly underestimates the density of excitations. The actual numerical calculation of the excitation energy density in our case is done as follows:

The space of the crystallite is divided into small cubic elementary cells with a dimension of $2 \cdot 2 \cdot 2 \text{ \AA}^3$. The coordinates of the centers of the cells are denoted by the vectors \vec{r}_m where the index m specifies the cell. For the given system there are 4000 of such cells. For each time from $t=0$ fs (the impact time of the primary particle onto the surface) to $t=750$ fs, the summed kinetic energy $E_k(\vec{r}_m, t)$ of atoms within each cell is calculated. For each time t_n , where t_n runs from $t=0$ to 750 fs in intervals $\Delta t=2.5$ fs, the values of $E_k(\vec{r}_m, t_n)$ are stored in the memory of the computer as a matrix. There are $750/2.5=300$ different times t_n and 4000 \vec{r}_m elements in space. We take first the matrix elements $E_k(\vec{r}_m, t_0)$ and according to Eq. (5.5) multiply them by A and Δt to obtain the excitation energy densities at (\vec{r}_m, t_1) .

The density $AE_k(\vec{r}_m, t_0)$ can be treated, in this discrete representation, as a point source term in the diffusion equation (5.7). Already during the time interval Δt the excitation diffuses rapidly around \vec{r}_m and thermalizes. The solution of Eq. (5.7) for the point source is the GREEN’S function that has the well known gaussian form [112]. For the first time step, the excitation energy density $E_k(\vec{r}_k, t_1)$ at a general point \vec{r}_k is then given by

$$E(\vec{r}_k, t_1) = A\Delta t \sum_m E_k(\vec{r}_m, t_0) \cdot \frac{1}{(4\pi D(t_1 - t_0))^{3/2}} \cdot \exp\left(\frac{-|\vec{r}_m - \vec{r}_k|^2}{4D(t_1 - t_0)}\right), \quad (5.14)$$

where the sum loops over all \vec{r}_m . Thus, according to Eq. (5.14), the matrix $E(\vec{r}_k, t_1)$ is actually the convolution of $E(\vec{r}_m, t_0)$ with the diffusion gaussian term as the convolution function.

If the diffusion coefficient D is time-independent, the values of $E(\vec{r}_k, t_2)$ that are due to $E_k(\vec{r}_m, t_0)$ can be obtained from Eq. (5.14) simply by substituting t_1 by t_2 , ultimately leading to the general description at arbitrary position and time

$$E(\vec{r}_k, t_i) = A\Delta t \sum_{n=0}^{i-1} \sum_m E_k(\vec{r}_m, t_n) \cdot \frac{1}{(4\pi D(t_i - t_n))^{3/2}} \cdot \exp\left(\frac{-|\vec{r}_m - \vec{r}_k|^2}{4D(t_i - t_n)}\right). \quad (5.15)$$

If D is allowed to vary as a function of time, a more complicated formalism must be used. For instance, if D changes from D_1 in the interval between t_1 and t_0 to D_2 in the time interval between t_2 and t_1 , we must substitute in the calculation of $E(\vec{r}_k, t_2)$ the diffusion coefficient D_2 by an effective coefficient D'_2

$$D'_2 = D_2 + \frac{t_1}{t_2}(D_1 - D_2) . \quad (5.16)$$

More generally, the constant value of D in Eq. (5.16) must be replaced by its average value in the time interval $t_i - t_n$. The simplicity of Eq. (5.16) is due to the gaussian form of the convolution function.

The final values of $E(\vec{r}_k, t_i)$, for any time t_i , are obtained by summing over all contributions to $E(\vec{r}_k, t_i)$ from $E_k(\vec{r}_m, t_p)$ from $t_p < t_i$. The calculation of the contributions to $E(\vec{r}_k, t_i)$ due to different $E_k(\vec{r}_m, t_p)$ follows the prescription given by Eqns. (5.14) and (5.16).

5.3 Application of the Model

“In this section, we will describe first calculations to test the application of the concepts developed above. In order to assess the magnitude of the electron temperature developing in particle impact induced collision cascades, the simulations are performed for the impact of 5-keV Ag atoms onto an unreconstructed Ag(111) surface.

First, normal MD simulations are performed without the inclusion of the electronic excitation for a set of 1225 trajectories in order to obtain information about statistical quantities like the average sputtering yield as well as the influence of different impact points on the intensity of the collision cascades. Then, two particular trajectories are chosen to be treated with the much more time consuming excitation code.

The first, which will in the following be referred to as no. 952, exhibits a total sputtering yield of 16 atoms/projectile that is very close to the average yield. From visualization of a number of simulations, we infer that this trajectory constitutes a normal case which is typical for the system and kinetic impact energy studied. The second, which will be called no. 207, leads to one of the highest sputtering yields (48 atoms/projectile), ejects the largest clusters and therefore represents an exceptional case where extremely large action is generated within the solid.

By investigating these two cases separately, it should be possible to gain insight into the “normal” behavior of collision cascades as well as the relatively rare events where many atoms are set in motion, thus leading to a high kinetic energy density in the cascade volume.

5.3.1 Diffusion Coefficient

As outlined above, the central parameter of the model describing the transport of electronic excitation is the diffusion coefficient D . In the Ag con-

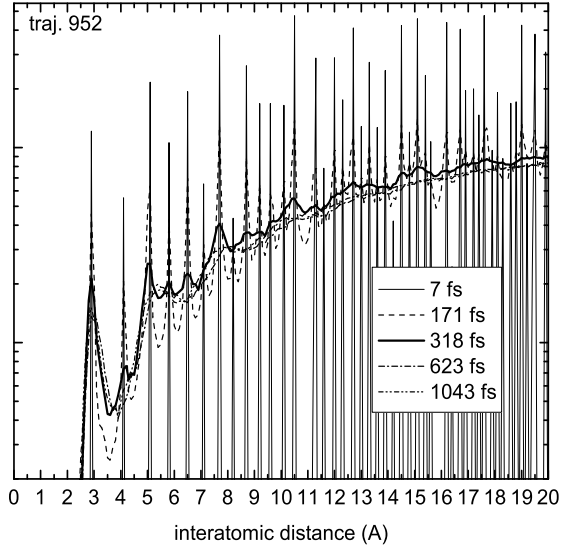


Figure 5.3: Pair correlation function of interatomic distances within the investigated Ag crystallite as a function of time after the impact of a 5-keV Ag atom.

duction band the FERMI energy is calculated as 5.48 eV, corresponding to a FERMI velocity of $v_F = 1.39 \times 10^8$ cm/s. For a crystalline solid, the value of D can be estimated from Eq. (5.6) using the electron mean-free path λ , which under non-equilibrium conditions characterized by an electron temperature T_e and a lattice temperature T_l is given by [113, 100, 114]

$$\lambda = \frac{v_F}{aT_e^2 + bT_l} . \quad (5.17)$$

For silver, the constants in Eq. (5.17) are estimated as $a = 1.2 \times 10^7$ K⁻²s⁻¹ and $b = 1.2 \times 10^{11}$ K⁻¹s⁻¹ [114]¹.

It should be noted that some controversy exists in the literature concerning the appropriate temperature dependence of λ . For instance, in their description of electron–phonon interaction in energetic displacement cascades, FLYNN and AVERBACK [95] have disregarded the role of electron–electron collisions altogether by omitting the first term in the denominator of Eq. (5.17). On the contrary, KOPONEN ET AL. [96, 97] have argued that the influence of electron–phonon scattering should be neglected in a two-temperature model, since it is explicitly included in the electron–phonon coupling term. This would result in the omission of the second term in the denominator of Eq. (5.17). In the scope of the model

¹The constants a and b can be calculated by applying the relationship [115] between electron–electron scattering and optical relaxation found by WISER ET AL [116], who demonstrated that the optically measured relaxation time constant corresponds to dc electron scattering measurements.

presented here, we feel that both electron–electron and electron–phonon scattering processes should be included in the determination of the electron mean-free path, thus leading to Eq. (5.17). The same formula has been extensively employed in two-temperature model descriptions of laser induced excitation processes [113, 100].

At room temperature ($T_e = T_l = 300$ K), the mean-free path resulting from Eq. (5.17) is of the order of several tens of nanometers. Since we will later show that lattice "temperatures" of the order of several thousands of Kelvin are rapidly reached in the collision cascade, we assume a diffusion coefficient of $D \approx 20$ cm²/s for the hot but still crystalline lattice, which corresponds to value of $\lambda \approx 4.2$ nm.

In the course of the developing collision cascade, the solid is rapidly disordered and finally completely amorphized. It is clear that the electronic energy transport properties must be altered by such a transition. In order to illustrate the time scale on which amorphization proceeds, Fig. 5.3 shows the pair correlation function, i.e. the distribution of interatomic distances within the simulated Ag crystallite, at various times after the projectile impact. It is apparent that the long range order is essentially lost within 300 fs, leaving only the short range order which is typical for an amorphous or liquid material. This result is practically identical for both investigated trajectories and can therefore be regarded as typical for a collision cascade.

The loss of crystallographic order will ultimately lead to a reduced value of the electron mean-free path and, hence, of the diffusion coefficient D . This phenomenon has been first discussed in [95], where it was pointed out that λ can become smaller than the cascade diameter and exhibits values of only few Å for liquid metals.

In order to estimate the magnitude of the effect, we assume for the amorphized system an electron mean-free path of the order of one interatomic distance, which with Eq. (5.6) leads to an altered diffusion coefficient of the order of 0.5 cm²/s.

Therefore, the value of D will generally decrease with time as the dynamic disorder increases in the course of the time development of the collision cascade. [...] In order to acknowledge the temporal variation of D , we assume a *linear* dependence between both limiting values within the first few hundred fs after the projectile impact and a constant value of 0.5 cm²/s at later times. The resulting electron energy densities and temperatures will be compared to those calculated under the assumption of a fixed diffusion coefficient of 20 or 0.5 cm²/s, respectively.

5.3.2 Application on Ag

Using the formalism described above, the electronic excitation energy density has been calculated as a function of time and space for two example collision cascades referred to as trajectories 952 and 207 which lead to average and high sputter yields, respectively. In both cases, the cascade was initiated by the normal incidence of a 5-keV Ag onto an Ag(111) surface

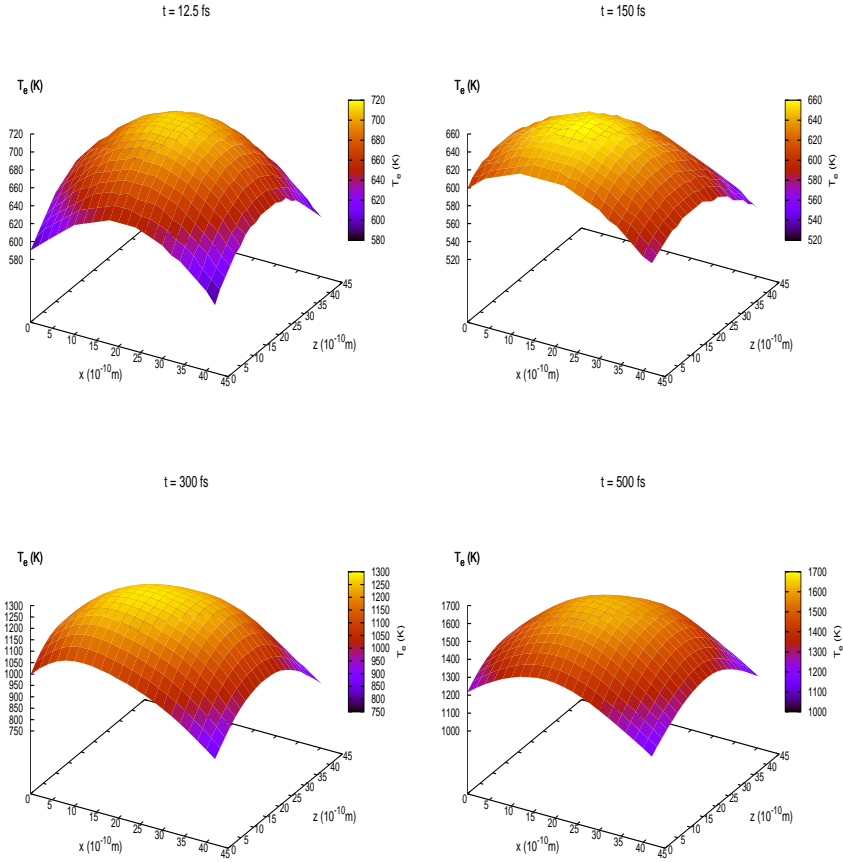


Figure 5.4: Snapshots of the two-dimensional spatial distribution of the electron temperature at the surface for four different times ($t = 12.5$ fs, $t = 150$ fs, $t = 300$ fs and $t = 500$ fs) after the projectile impact. The data correspond to the particular collision cascade labeled as trajectory 207 in the text. In order to illustrate the observed variation, the color scale code was for each individual image chosen such as to extend over the observed range between minimum and maximum values.

onto two different impact points.”

As outlined in the previous subsection, the diffusion coefficient D was chosen to decrease linearly from $20 \text{ cm}^2/\text{s}$ at $t = 0$ to $0.5 \text{ cm}^2/\text{s}$ at $t = 300$ fs and stay constant thereafter.”

The results are exemplified in Fig. 5.4 showing temporal snapshots of the two-dimensional spatial distribution of the electron temperature T_e at the surface, i.e. in the uppermost cell layer of the model. Although the complete three-dimensional distribution is obtained from the calculations, the surface distribution was selected for visualization since more than 90% of the sputtered particles originate from the topmost layer and therefore their excitation and ionization probabilities are determined by the electron temperature at this location.

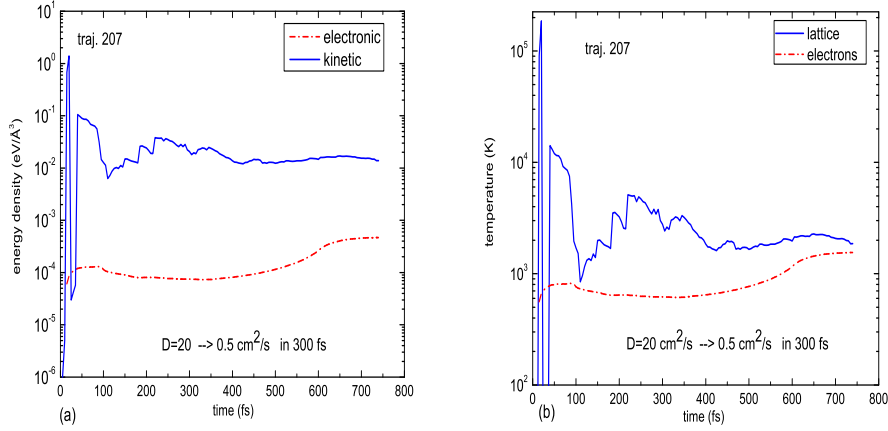


Figure 5.5: (a): Average total kinetic and electronic excitation energy density at the surface versus time after the projectile impact. The data were calculated for a particular collision cascade described as Traj. 207 in the text. (b): Average “lattice temperature” and electron temperature at the surface versus time after the projectile impact. The data were converted from the energy densities depicted in (a).

What becomes directly obvious from a rough inspection of Fig. 5.4 is (i) the smearing of the electronic excitation due to diffusive transport and (ii) an interesting time structure of the maximum electron temperature observed at the surface. However, at this point, the series of snapshots in Fig. 5.4 is not intended to be precisely discussed with respect to the two aforementioned issues, but rather to give the reader a first impression of results.

Of note are the different scales of the energy axis on the plots in Fig. 5.4. In order to allow a better comparison, we average both quantities over the entire surface of our model crystallite and plot the resulting time dependence of the kinetic and electronic surface energy density in Fig. 5.5(a). It is seen that the electronic excitation energy rises quickly within the first few 10 fs, exhibits an intermediate plateau and then slowly starts to rise again at 300 fs. This rise is clearly connected to the decrease of the energy diffusion coefficient used in the simulation. A second maximum appears at approximately 650 fs with excitation energy densities of about $4 \times 10^{-4} \text{ eV}/\text{\AA}^{-3}$ which translate to electron temperatures of 1500-1700 K. The kinetic energy density at the surface, on the other hand, shows large fluctuations in the beginning – which are due to the projectile crossing the surface cell layer – and then also levels at a fairly constant value.

Probably the most important information extracted from Fig. 5.5 is the fact that at all times the kinetic energy density is significantly larger than the electronic excitation energy density. This finding is important since it demonstrates that the neglect of energy flow from the electron gas to the

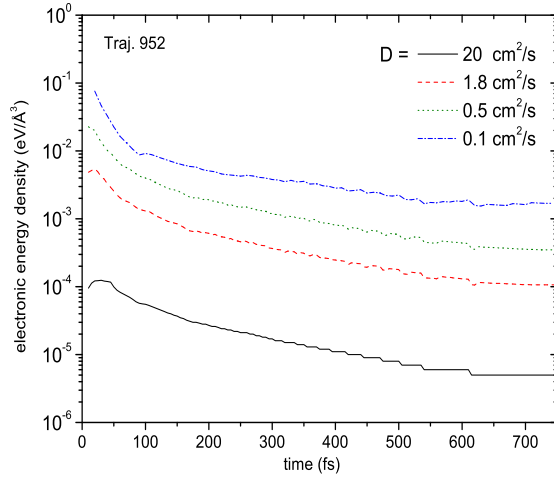


Figure 5.6: Surface electronic excitation density at the impact point versus time after projectile impact. The data have been calculated for trajectory 952 (see text) using a constant electron energy diffusion coefficient as displayed.

lattice in our model is probably justified. In order to further substantiate that statement, we convert both quantities into temperatures using a lattice specific heat of $(3/2)nk_B$ and Eq. (5.13) for T_e . The constant C in Eqns. (5.13) and (5.13) was evaluated as $C = 3.9 \times 10^{-10} \text{ eV}\text{\AA}^{-3}\text{K}^{-2}$ using the electron density $n_e = 5.85 \times 10^{22} \text{ cm}^{-3}$ and FERMI temperature $T_F = 6.4 \times 10^4 \text{ K}$ of silver [111]. The results are plotted in Fig. 5.5(b). Note that the lattice "temperature" determined this way has no real physical meaning since the particle kinetics within the collision cascade do not necessarily follow MAXWELL-BOLTZMANN statistics. Moreover, no correction for possible collective motion velocity components (which for a real temperature determination would have to be subtracted from the individual particle velocities in a cell [113]) has been performed. Nevertheless, it is evident that – although the specific heat of the electron gas is much lower than that of the lattice – the electron temperature never significantly exceeds the lattice "temperature". Therefore, also a two-temperature model as used frequently to describe lattice heating by electronic excitation [109] would predict negligible energy flow back from the electron system into the lattice dynamics.

It is of course essential to investigate how the particular choice of the diffusion coefficient D influences the simulated results. In order to visualize the surface distribution of the calculated electronic energy density and electron temperature, we plot radial distributions that are obtained in the following way.

First, the surface electron energy density is averaged over four cells that are located in the directions parallel to the crystallite edges at a certain

radial distance r from that cell containing the impact point.

The resulting surface energy density calculated for a constant diffusion coefficient as a function of time after the projectile impact is depicted in Fig. 5.6. The data have been calculated for trajectory 952; the corresponding curves for trajectory 207, however, look very similar. In order to illustrate the influence of energy transport, different values of the diffusion coefficient were used spanning the range from an unrealistically low value of $0.1 \text{ cm}^2/\text{s}$ to $D = 20 \text{ cm}^2/\text{s}$, which is assumed to be appropriate for the crystalline solid. It is seen that the magnitude of the electronic excitation roughly scales with the inverse of D . Moreover, the surface energy density rapidly goes through a maximum at very short times below 50 fs which is produced by the large energy loss of the projectile crossing the surface layer and then decays again. Note that although the figure seems to suggest that a “steady state” is reached after about 1 ps, it is clear that in the limit of large time the electronic interaction must dissipate in the bulk of the solid and, hence, the excitation energy density must go to 0.

Second, the average energy density is converted into surface electron temperature by means of Eq. (5.13). Again, the results are plotted as a function of time after the projectile impact for different values of r . Fig. 5.7 shows such a plot calculated for trajectories 207 and 952 for the case of a *constant* diffusion coefficient of $D = 20$ and $0.5 \text{ cm}^2/\text{s}$, respectively. As outlined in Section 5.3.1, these values are assumed to correspond to an ordered and to a completely amorphized crystal, respectively, and the results must therefore be regarded as limiting cases.

It is seen that the projectile induced maximum T_e is most pronounced directly at the impact point. If heat diffusion is fast, the curves at larger radial distance completely track with that for $r = 0 \text{ \AA}$, thus indicating that the electron excitation is distributed homogeneously across the cascade volume.

If diffusion is slow, on the other hand, it is clearly visible that the temperature rise at larger distance r is slower and the maximum is less pronounced than at $r = 0 \text{ \AA}$. At times exceeding approximately 500 fs, all curves are found to merge to a “steady state” surface temperature, the inverse of which is found to linearly increase with increasing D . Note, that the results calculated for both trajectories are almost identical, thus indicating that the details of the particular collision cascade are not important. This finding is understandable due to the large number of collisions involved in such a cascade. The time dependence of T_e can be compared to the temporal evolution of particle emission, which has been included in the figure for both trajectories. It is evident that the majority of sputtered particles leave the surface at times later than 100 fs, thus making the sharp peak of T_e at times below 100 fs practically unimportant for the determination of their charge or excitation states.

As already stated in Section 5.3.1, the temperature evolution depicted in Fig. 5.7 is not realistic since the diffusion coefficient will probably vary as a function of time due to collision induced atomic disorder.

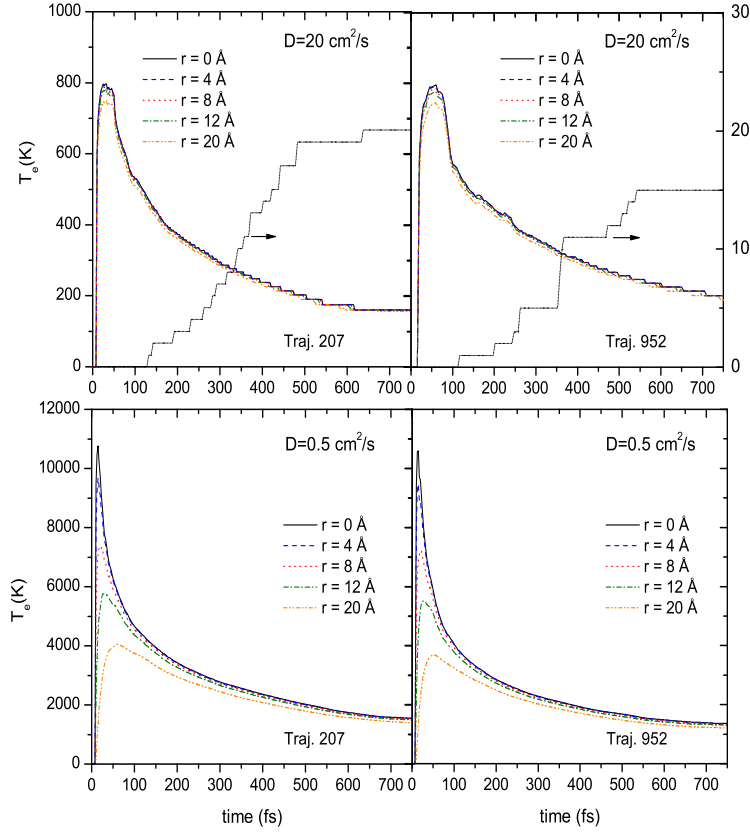


Figure 5.7: Average surface electron temperature at different radial distances r from the impact point versus time after the projectile impact. The data were calculated for two different trajectories using a constant electron energy diffusion coefficient as displayed. The thin solid black line depicts the temporal evolution of sputtered particle emission.

In order to arrive at a more realistic description of the transport of electronic energy within a collision cascade, we therefore invoke a time-dependent D that is assumed to vary linearly from the crystal limit at $t = 0$ to the amorphous limit at $t = t_{am}$ and remains constant thereafter.

The resulting time evolution of the surface electron temperature is depicted in Fig. 5.8 for two different values of the amorphization time t_{am} . It is seen that the decrease of D during the cascade evolution leads to an increase and a second maximum of the electron temperature, which roughly occurs at $1.5t_{am}$.

This finding is particularly interesting, since the electronic excitation at the surface is now largest during the time period where most of the sputtered particles are emitted [...]. Moreover, the absolute values of the electron temperature are predicted to be of the order of 2000 K, a value which is sufficient to significantly influence the ionization and excitation

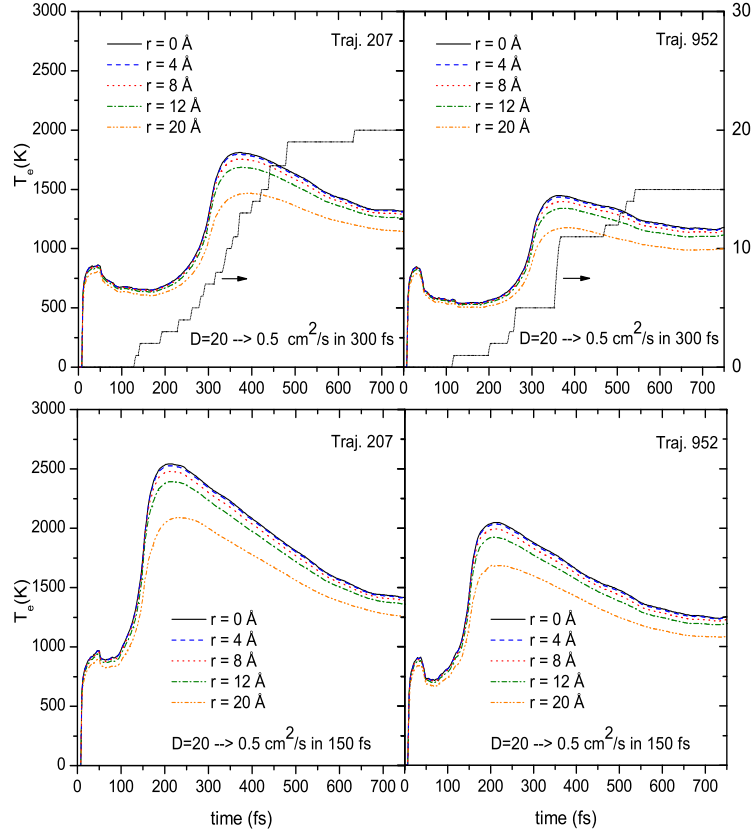


Figure 5.8: Average surface electron temperature at different radial distances r from the impact point versus time after the projectile. The data were calculated for two different trajectories using a time-dependent electron energy diffusion coefficient D as explained in the text.

probability of sputtered particles.

[...] It should be noted that figures similar to Fig. 5.5 have been published by KOPONEN and HAUTALA [97] who employed a two-temperature model to describe the thermalization of a high-energy collision cascade. There are, however, a few fundamental differences which should be discussed in more detail. First, the electronic system treated in [97] is assumed to start with a high electron temperature which then decreases with time. This assumption clearly neglects the details of the short-term processes heating the electron gas which we are aiming at in the present study. Second, the data in Ref. [97] indicate that T_e remains essentially constant in the time range studied here, whereas our simulations predict a strong variation depending on the particular choice of the diffusion coefficient D . These differences are in part due to the different impact energy ranges explored in both studies ($\approx 100 \text{ keV}$ in Ref. [97] versus keV here), but also

reflect the fact that the model described in Ref. [97] has been designed to describe the long-term temporal evolution of a collision cascade rather than the details of kinetic excitation during the first few hundred fs after the projectile impact.”

5.4 Conclusion

In this chapter, “a computer simulation model of the electron excitation in collision cascades in solids bombarded with keV atomic particles has been developed.

The model uses molecular dynamics for the simulation of atomic movements which excite the electrons and uses an approximate semiclassical approach for the description of spatial and temporal developments of the excitations. In this approach the excitations are characterized by the energy density of electron–hole pairs. The energy in the conduction band rapidly diffuses in space and thermalizes, creating a local electronic temperature T_e in the sp band.

It is shown that the calculated surface temperature T_e can reach values of several thousands of Kelvin, thus showing that the electronic excitation process discussed here can influence the formation of slow ions and excited atoms emitted from solids during sputtering.”

It is obvious that the model presented in this chapter “represents only a first step towards a microscopic understanding of the electronic excitation processes occurring in a collision cascade. On our way towards a more quantitative description”, in the following chapter, we will extend the model presented here in order to account for a more “appropriate description of the lattice order dependent diffusion coefficient D ”.

Chapter 6

Low-energy Electronic Excitation in Atomic Collision Cascades: A nonlinear Transport Model based on Electronic Friction

The electronic excitation calculations presented in the previous chapter have demonstrated that for the model system 5-keV Ag \rightarrow Ag(111), electron temperatures T_e of several thousands of Kelvin may be obtained. These temperatures appear to be large enough to influence the electronic states of emitted particles. However, the numerical approach employed in the *linear transport model* is restricted to *constant* or at most *time-dependent* diffusivity D .

It is well known that the evolution of an atomic collision cascade leads to a time- and position-dependent reduction of crystallographic order within the solid. As a consequence, the electron mean-free path λ and, hence, the diffusivity D will exhibit strong local and temporal variations.

In the present chapter - which in essence has been published in the article *Low-energy electronic excitation in atomic collision cascades: A nonlinear transport model* by A. DUVENBECK and A. WUCHER appeared in Phys. Rev. B **72**, 165408 (2005) - we therefore extend our model towards a full three dimensional treatment based on a finite differences approach which allows for a *spatial variation* of D . The latter, in turn, is correlated with both the *lattice* and the *electron temperature* at each point in space and time.

In addition, we incorporate a *local order parameter* which is calculated from the time-dependent atom positions delivered by the MD calculation. This parameter is then used to interpolate the local diffusivity D between values appropriate for an ideal crystal and a fully amorphized solid, respectively.

Results show that the atomic disorder plays a key role in trapping the electronic excitation in the cascade volume. The resulting time-dependence of the electron temperature T_e is again calculated as a function of position around the impact point in order to allow for a comparison with the *linear* transport model.

6.1 Description of the Model

The excitation model presented in the previous section may be separated into three distinct parts: (i) the calculation of particle dynamics using molecular dynamics, (ii) the description of the physical excitation mechanism and (iii) excitation energy transport, respectively. However, the new extensions to that model, which are to be figured out in this chapter, only involve the excitation energy transport. Thus, the MD calculation as well as the calculation of the source terms of excitation energy remain unchanged and will therefore not be outlined again.

Focusing on the transport of excitation energy, now, the crucial role of the diffusivity of excitation energy D has become obvious. In the specific case of a *constant* diffusion coefficient the diffusion equation is given by

$$\frac{\partial E(\vec{r}, t)}{\partial t} - D \nabla^2 E(\vec{r}, t) = \left(\frac{dE(\vec{r}, t)}{dt} \right)_s, \quad (6.1)$$

which can be solved in a straightforward way employing the GREEN's function method as discussed in the previous chapter.

“In the following, we will expand the versatility of the approach by allowing D to depend on the lattice temperature T_l , the calculated electron temperature T_e itself and an additional lattice order parameter $\Lambda(\vec{r}, t)$. The exact functional form of D will be discussed in the following subsection. The corresponding diffusion equation

$$\frac{\partial E(\vec{r}, t)}{\partial t} - \vec{\nabla} \cdot (D(T_l(\vec{r}, t), T_e(\vec{r}, t), \Lambda(\vec{r}, t)) \vec{\nabla} E(\vec{r}, t)) = \left(\frac{dE(\vec{r}, t)}{dt} \right)_s \quad (6.2)$$

is no longer linear in $E(\vec{r}, t)$, thereby complicating the numerical treatment. In particular, it is no longer possible to solve Eq. (6.2) by means of a simple GREEN's function approach. Instead, we revert to a finite differences treatment described in detail below.

6.1.1 Diffusion Coefficient

In principle the diffusivity D of electronic excitation energy can be evaluated as (\rightarrow page 55)

$$D = \frac{1}{3} \lambda v_F, \quad (6.3)$$

where λ denotes the mean-free path of the electrons and v_F is the FERMI velocity. Under non-equilibrium conditions characterized by an electron

temperature T_e and a lattice temperature T_l - both varying in space and time - the mean free path in a perfectly crystalline solid is given by [114]

$$\lambda = \frac{v_F}{aT_e^2 + bT_l}. \quad (6.4)$$

The first term in the denominator of Eq. (6.4) arises from electron-electron scattering, while the second term originates from electron-phonon scattering." For silver, the constants v_F , a and b have already been estimated on page 60.

The lattice temperature T_l entering Eq. (6.4) we calculate as

$$T_l(\vec{r}, t) = \frac{2E_k^{tot}(\vec{r}, t)}{3Nk_B}, \quad (6.5)$$

"where E_k^{tot} denotes the sum of the relative kinetic energy of all N particles localized within a sphere of radius r_c centered at \vec{r} at time t . The center-of-mass velocity is subtracted in order to exclude a possible influence of directed collective motion.

We are aware that the definition of a lattice temperature is critical because the particle dynamics within the cascade may exhibit a strongly non-equilibrium character. Furthermore, in the simulation we have to make a trade-off between sufficient particle statistics on the one hand, which demands for large sphere radii r_c , and on the other hand a reasonable spatial resolution of the temperature profile requiring small values of r_c . Thus, the calculated values for T_l should be interpreted carefully and only be regarded as a physical parameter describing the kinetic energy density in the cascade volume rather than a realistic temperature.

Now, substituting Eq. (6.4) into Eq. (6.3) yields the expression

$$D_0(\vec{r}, t) = \frac{1}{3} \frac{v_F^2}{aT_e^2(\vec{r}, t) + bT_l(\vec{r}, t)}, \quad (6.6)$$

where the index zero is meant to underline that disorder effects have not yet been taken into account. At room temperature ($T_e = T_l = 300$ K) the mean-free path resulting from Eq. (6.4) is of the order of 40 nm! This value is exclusively determined by electron-phonon scattering and yields $D^{cryst} \approx 180$ cm²/s.

We remark that, for that particular case, the mean-free path exceeds the dimension of our model crystal by about one order of magnitude, calling the diffusive approach into question. On the nanometer scale targeted here, the transport of excitation energy within a quiescent ideal crystal should therefore be described more realistically in terms of ballistic motion rather than by a diffusion mechanism. However, as shown below, the rapid lattice heating, combined with the effect of local disorder, leads to a drastic reduction of λ and D within the first few femtoseconds of a collision cascade, thereby justifying the diffusive treatment at later times."

So far, only the particular case of a *crystalline* solid under non-equilibrium conditions has been taken into consideration. However, the detailed

analysis of the time-dependent radial distribution function (\rightarrow page 61) revealed “a rapid destruction of the crystalline order on sub-picosecond time scales after the primary particle impact. More specifically, the evolution of the atomic collision cascade induces a rapid loss of long range order, leading to a complete amorphization of the model system within a time interval of approximately 300 fs. In this limit, the concept of electron-phonon scattering must be replaced by quasi-elastic scattering on individual atoms with a mean free path λ comparable to the mean interatomic distance. The excited electrons will therefore undergo a chaotic motion which can be described rather well by a diffusive approach with a diffusion coefficient of the order of $D^{am} \approx 0.5 \text{ cm}^2/\text{s}$ (Ref. [110]).”

In chapter 5, “the influence of crystalline order has been described only *qualitatively* without spatial resolution by assuming the diffusivity to decrease linearly between D^{cryst} and D^{am} within a time interval of several 100 fs after the projectile impact. While this temporal variation could be easily incorporated into the numerical GREEN’s function method employed to solve the diffusion equation, it allowed no spatial variation of D . The latter, on the other hand, appears to be important due to the strongly local character of the collision cascade dynamics.

In the following, we present an approach to incorporate both the temporal and spatial dynamics of lattice disorder as well as its coupling to the diffusivity D . For that purpose, a scalar, local lattice order parameter is defined at $\vec{r} = (x_1 = x, x_2 = y, x_3 = z)$ by [45]

$$\Lambda(\vec{r}, t) = \frac{1}{3N} \left| \sum_i \sum_{j=1}^3 \cos \left(\frac{2\pi}{a_j} x_j^i(t) \right) \right|, \quad (6.7)$$

where the outer sum loops over all N particles within a sphere of radius r_c around \vec{r} . The parameters a_j denote the nearest neighbor distances in the x_j -directions of the coordinate system. Thus, the case of a completely ordered fcc crystal yields $\Lambda=1$ because each particle is positioned on a lattice site and therefore each cosine in Eq. (6.7) is equal to one. In the case of a completely amorphized crystal, on the other hand, the values of Λ fluctuate statistically around zero with an amplitude of the order of $\delta = N^{-1/2}$, provided the cut-off-radius r_c is not too small. In our treatment, we chose a value of $r_c=8 \text{ \AA}$ (corresponding to $\delta \approx 0.05$), which is large enough to include the 7th-nearest neighbor shell in a silver crystal.

It should be pointed out at this point, that the order parameter considered here is based on rather simple periodicity arguments. More sophisticated definitions of scalar order parameters which, for example, take into account bond-orientation statistics [117, 118] can be found in the literature. However, they are significantly more time consuming to calculate. Moreover, MORRIS and SONG [119] have proposed a scalar measure of translational order that is very similar to Eq. (6.7), but additionally features a time- and neighbor-averaging procedure in order to cancel out artefacts

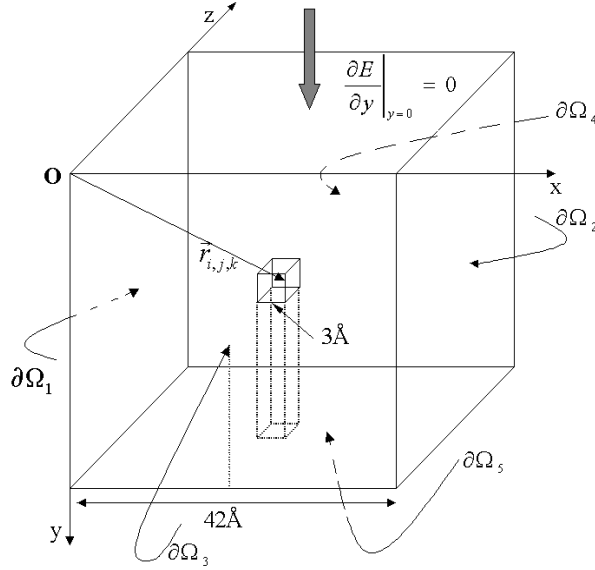


Figure 6.1: Schematic drawing showing the boundaries, dimensions as well as one representative discretization cell.

caused by fast atomic lattice vibrations. This averaging procedure, however, would conceal the fast, collision induced lattice dynamics which are explicitly considered here and therefore would be detrimental to the goal of the present work.

The next step in our model description regards the influence of local disorder on the effective diffusivity D . In principle, it is not trivial to rigorously derive a straightforward relation between Λ and D , which is based on simple arguments.

As a zero-order approach, we apply a linear interpolation between the two limiting cases of (i) a completely ordered crystal ($\Lambda = 1$) and (ii) an amorphous ensemble of particles ($\Lambda \approx 0.05$) with

$$D(\Lambda = 1) = D_0 \text{ and } D(\Lambda = 0.05) = D^{am} , \quad (6.8)$$

leading to

$$D(\vec{r}, t) = \frac{D_0(\vec{r}, t) - D^{am}}{0.95} \cdot \Lambda(\vec{r}, t) + \frac{D^{am} - 0.05D_0(\vec{r}, t)}{0.95} . \quad (6.9)$$

In combination with Eq. (6.6), this relation describes the influence of local heating, electronic excitation and lattice disorder on the excitation energy diffusivity D . Note that the dependence on \vec{r} is implicate via local variations of the electron temperature T_e , lattice temperature T_l and order parameter Λ .

6.1.2 Numerical Implementation

The model crystallite of dimension $42 \times 42 \times 42 \text{ \AA}^3$ is discretized into 2744 small cubic volume elements with grid spacing $\Delta = 3 \text{ \AA}$ in each direction. The function $E(\vec{r}, t)$ is then represented by its values at the discrete set of cell centers $\vec{r}_{i,j,k} = i\Delta \cdot \vec{e}_x + j\Delta \cdot \vec{e}_y + k\Delta \cdot \vec{e}_z$ with $(i, j, k) \in \{1, \dots, 14\}^3$ and \vec{e}_x , \vec{e}_y and \vec{e}_z denoting the unit vectors in x -, y - and z -direction (see Fig. 6.1).

Let $E_{i,j,k}^{n=0}$ denote the initial excitation energy distribution at time t_0 at $\vec{r}_{i,j,k}$. Then, the resulting distribution $E_{i,j,k}$ at time $t_{n+1} = t_0 + (n+1)\Delta t$ is numerically evaluated as [120]

$$\begin{aligned} E_{i,j,k}^{n+1} = \Delta t \cdot \left(\frac{dE}{dt} \right)_s \Big|_{i,j,k}^n + \frac{\Delta t}{\Delta r^2} \Big\{ & D_{i+\frac{1}{2},j,k}^n \cdot (E_{i+1,j,k}^n - E_{i,j,k}^n) \\ & - D_{i-\frac{1}{2},j,k}^n \cdot (E_{i,j,k}^n - E_{i-1,j,k}^n) + D_{i,j+\frac{1}{2},k}^n \cdot (E_{i,j+1,k}^n - E_{i,j,k}^n) \\ & - D_{i,j-\frac{1}{2},k}^n \cdot (E_{i,j,k}^n - E_{i,j-1,k}^n) + D_{i,j,k+\frac{1}{2}}^n \cdot (E_{i,j,k+1}^n - E_{i,j,k}^n) \\ & \left. - D_{i,j,k-\frac{1}{2}}^n \cdot (E_{i,j,k}^n - E_{i,j,k-1}^n) \right\} + E_{i,j,k}^n \end{aligned} \quad (6.10)$$

with

$$D_{i+\frac{1}{2},j,k}^n = \frac{1}{2} \cdot \{ D(T_{l;i+1,j,k}^n, T_{e;i+1,j,k}^n, \Lambda_{i+1,j,k}^n) + D(T_{l;i,j,k}^n, T_{e;i,j,k}^n, \Lambda_{i,j,k}^n) \}. \quad (6.11)$$

$$(6.12)$$

The boundary conditions for the solution of Eq. (6.2) are critical. At the surface ($j=1$), a *Neumann* condition $\vec{\nabla} E \cdot \vec{n} = 0$ is enforced in the outward direction to prohibit outward diffusion of excitation energy into the vacuum. This is implemented by defining a virtual cell layer at $j=0$ with $E_{i,0,k} := E_{i,1,k}$.

For the other boundaries of the crystal the underlying physics require *open* boundary conditions. In order to realize that, we introduce a set of virtual cell layers, which in the following will be referred to as $\partial\Omega_m$ with $m \in \{1, \dots, 5\}$ denoting the left, right, front, back and bottom virtual cell layer with corresponding surface normal vectors \vec{n}_m . Each of these virtual layers of cells is directly attached outside the corresponding crystal boundary plane. Then we calculate the excitation energy

$$\Delta E^{out,n} = \frac{1}{\Delta r} D_{out} \vec{\nabla} E \cdot \vec{n}_m \Delta t \quad (6.13)$$

flowing out of each boundary cell during the time interval Δt at time t under the assumption of a *constant* diffusion coefficient D_{out} outside the crystal. These values are stored in a large data matrix and taken as electronic energy point sources ΔE^s localized at the particular virtual cell in the corresponding virtual cell layer. Since the outward diffusivity is constant, the time evolution of E within these virtual cells is followed using the GREEN's function formalism.

To illustrate this procedure, let $I_m := \{(i, j, k) | \vec{r}_{i,j,k} \in \partial\Omega_m\}$ denote the set of indices representing the virtual cells of the m -th virtual layer. Formally, the values of E within these virtual cells at time t_n are calculated as (\rightarrow Eq. (5.15), page 58)

$$E(\vec{r}_{i,j,k} \in \partial\Omega_m, t_n) = \sum_{\alpha=0}^{n-1} \sum_{\kappa,\mu,\nu \in I_m} \Delta E_{\kappa,\mu,\nu}^{s,\alpha} \times \frac{1}{(4\pi D_{out}(t_n - t_\alpha))^{\frac{3}{2}}} \exp\left(\frac{-|\vec{r}_{\kappa,\mu,\nu} - \vec{r}_{i,j,k}|^2}{4D_{out}(t_n - t_\alpha)}\right) \quad (6.14)$$

and taken as the new boundary conditions for the next finite differences time step.

As an example to demonstrate the implementation of Eq. (6.13) and (6.14), consider the left crystal boundary plane characterized by a fixed cell index $i=1$. According to Eq. (6.13), the energy flowing out of cell $(1, j, k)$ towards the outside of our simulation volume is given by

$$\Delta E_{1,j,k}^{out,n} = \frac{\Delta t}{\Delta r^2} D_{out}(E_{1,j,k}^n - E_{0,j,k}^n) . \quad (6.15)$$

Here, $E_{0,j,k}^n$ denotes the energy content of a virtual cell belonging to the virtual boundary cell layer at $i=0$. This energy is fed into the virtual cell $(0, j, k)$ as a source term $\Delta E_{0,j,k}^s$, thereby increasing its energy content, and allowed to diffuse and heat up the other virtual cells $(0, j', k')$. By superposition of the contribution originating from all other virtual cells $(0, \mu, \nu)$ during all preceding time steps $\alpha < n$ the energy content of a virtual cell $(0, j, k)$ at time step n is calculated as

$$E_{0,j,k}^n = \sum_{\alpha=0}^{n-1} \sum_{\mu,\nu} \Delta E_{0,\mu,\nu}^{s,\alpha} \cdot \frac{1}{(4\pi D_{out}(n - \alpha)\Delta t)^{\frac{3}{2}}} \times \exp\left(-\frac{[(\mu - j)^2 + (\nu - k)^2]\Delta r^2}{(4\pi D_{out}(n - \alpha)\Delta t)}\right) . \quad (6.16)$$

These values are then used as the new boundary conditions in order to calculate $\Delta E_{1,j,k}^{out,n+1}$ at the next time step, etc.

The time step Δt used in the numerical integration of Eq. (6.2) is critical. If Δt is chosen too large, the solution calculated by Eq. (6.10) becomes unstable. An obvious condition for numerical stability is given by

$$\Delta r^2 / \Delta t > D_{max} , \quad (6.17)$$

where D_{max} denotes the maximum possible value of the diffusivity. With $\Delta r=3 \text{ \AA}$ and $D_{max}=180 \text{ cm}^2/\text{s}$, this yields $\Delta t \leq 10^{-18} \text{ s}$. Attempts using this value, however, were still hampered by serious stability problems, which were found to disappear only if Δt was reduced to about 10^{-20} s . On the other hand, this time step is unnecessarily small for the MD-simulation.

Therefore both computing parts are separated from each other as follows. First, the particle kinetics are followed up to a total simulated time of 750 fs using our standard molecular dynamics code with dynamical time step adjustment in the range of 10^{-17} - 10^{-15} s. In equidistant time steps of $\Delta t^{MD}=1$ fs, the positions of all particles in the system are stored in a data matrix. After the molecular dynamics trajectory integration has finished, this data matrix is used as input for the explicit finite-differences scheme. In order to accommodate for the much smaller time step, the positions are linearly interpolated within each time interval Δt^{MD} . The two simulation parts are synchronized by performing in each time interval Δt^{MD} the necessary number of finite-differences time steps. After time intervals of 1 fs the complete set of E as a function of space and time in the solid is output and converted into electronic temperature according to Eq. (5.13).

In order to limit the memory and CPU time requirements of the code, the boundary conditions are updated in time intervals of 1 fs by means of Eq. (6.14). Test calculations have shown that a higher boundary refresh rate does not significantly alter the calculated electronic energy density distribution.”

6.2 Application on Silver

Applying the procedure described above, the excitation energy density is calculated as a function of time and space for the same exemplary atomic collision cascade - induced by a 5-keV silver atom impinging onto an Ag(111) surface under normal incidence - as chosen in chapter 5.

“In order to compare the model presented here with the GREEN’s function approach applied earlier [...], Fig. 6.2 shows the calculated time-dependence of the *surface* electron temperature T_e at a radial distance of $r=15$ Å from the impact point for an arbitrarily assumed constant diffusivity $D = 20$ cm²/s¹.

It is seen that the finite differences (FD) calculation predicts a rather sharp initial rise of T_e , which is induced by the highly energetic projectile penetrating the surface layer, thereby locally feeding excitation energy into the electronic system at the impact point. Due to the onset of diffusion, this energy rapidly spreads around the original point of excitation, leading to a pronounced maximum of T_e at times of the order of 10 fs after the impact. Later, the evolution of the collision cascade leads to a spatial spread of kinetic energy and, hence, a stronger delocalization of electronic excitation

¹At this point, it should be noted that the data shown in Fig. 6.2 still originate from the very early developing stage of the software codes, where in both treatments (GREEN’s function and finite differences) the electronic friction was already used as a source of excitation energy, which, however, was not yet incorporated into the Newtonian equations of motion as an additional frictional force acting on the atomic particles. Therefore, the results presented in this particular figure may overestimate the resulting electron temperatures. Nevertheless, for the purpose of comparing the results obtained from the two different approaches, we consider this shortcoming to be only of negligible significance.

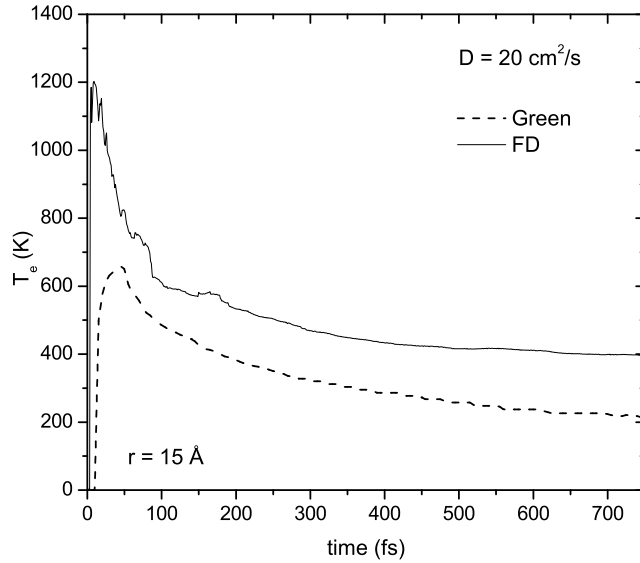


Figure 6.2: Time evolution of the surface electron temperature for a radial distance $r = 15 \text{ \AA}$ from the impact point.

sources within the crystal volume. In combination with the rapid dissipation of excitation energy, this results in a fast decay of T_e as a function of elapsed time. At $t=750 \text{ fs}$ the electron temperature has decreased to values only slightly above room temperature. At this point, we remark that the fine-structure observed in Fig. 6.2 is not caused by statistical noise, but reflects the kinetics of fast secondary recoil atoms in the uppermost crystal layer.

Comparing the FD-calculation with the GREEN's function method, we observe characteristic differences. At small times after the projectile impact, the FD-calculation apparently predicts significantly higher electron temperatures. Although not as pronounced, slightly larger temperatures are also predicted at later times. We attribute these observations to the different boundary conditions employed in both types of calculations. More specifically, the GREEN's function approach generates a full-space solution, whereas the FD-calculation correctly incorporates the surface by prohibiting outward energy flow towards the vacuum. As a zero-order approximation, one would therefore expect a factor 2 between the energy densities calculated with both methods. In combination with Eq. (5.13) this would translate to $\sqrt{2}$, which is in reasonable agreement with the data presented in Fig. 6.2.

The FD-code now provides a powerful basis to calculate more realistic electron temperatures using a time- and space-resolved diffusivity D .

As a prerequisite, Fig. 6.3 shows the time-dependence of the order parameter Λ averaged over two different volumes of the model crystallite. The

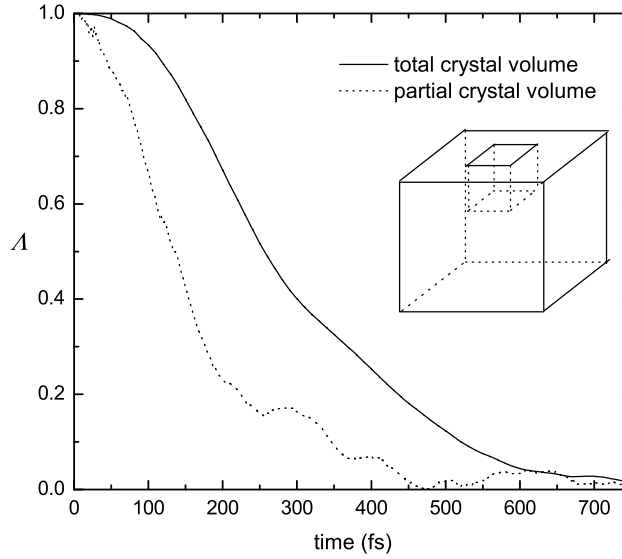


Figure 6.3: Local order parameter Λ for two different crystal volumes as a function of time after the projectile impact. The relative size and position of the ‘partial’ crystal volume (dotted line) within the total model crystallite (solid line) is schematically drawn, too.

data depicted by the solid line have been averaged over the total crystallite, whereas the dotted line corresponds to the average taken over a small cubic sub-volume of dimension $10 \times 10 \times 10 \text{ \AA}^3$ located in the center of the collision cascade (see small sketch depicted in Fig. 6.3). Here, the crystallographic order is completely destroyed within approximately 350 fs after the particle impact. Apparently, the time scale for this transition is significantly longer in the larger volume, illustrating the highly localized character of the lattice disorder generated in the cascade. This finding illustrates the necessity of a space- and time-resolved determination of Λ in evaluating the local diffusivity via Eq. (6.9).

Using the same MD data as in Fig. 6.2, the dynamics of the electron temperature distribution are calculated using the FD-code with a space and time resolved diffusivity according to Eq. (6.6).” As initial temperatures we choose $T_e = T_l = 300 \text{ K}$.

“Figure 6.4 depicts temporal snapshots of the resulting lateral distribution of (a) the electron temperature and (b) the diffusion coefficient D evaluated at the surface, i.e., in the uppermost cell layer of the model crystallite. This particular visualization was chosen, because we are in the long run interested in determining the influence of T_e on excitation or ionization of sputtered particles, which predominantly originate directly from the surface.

In order to emphasize the role of lattice dynamics, Fig. 6.4(c) shows a

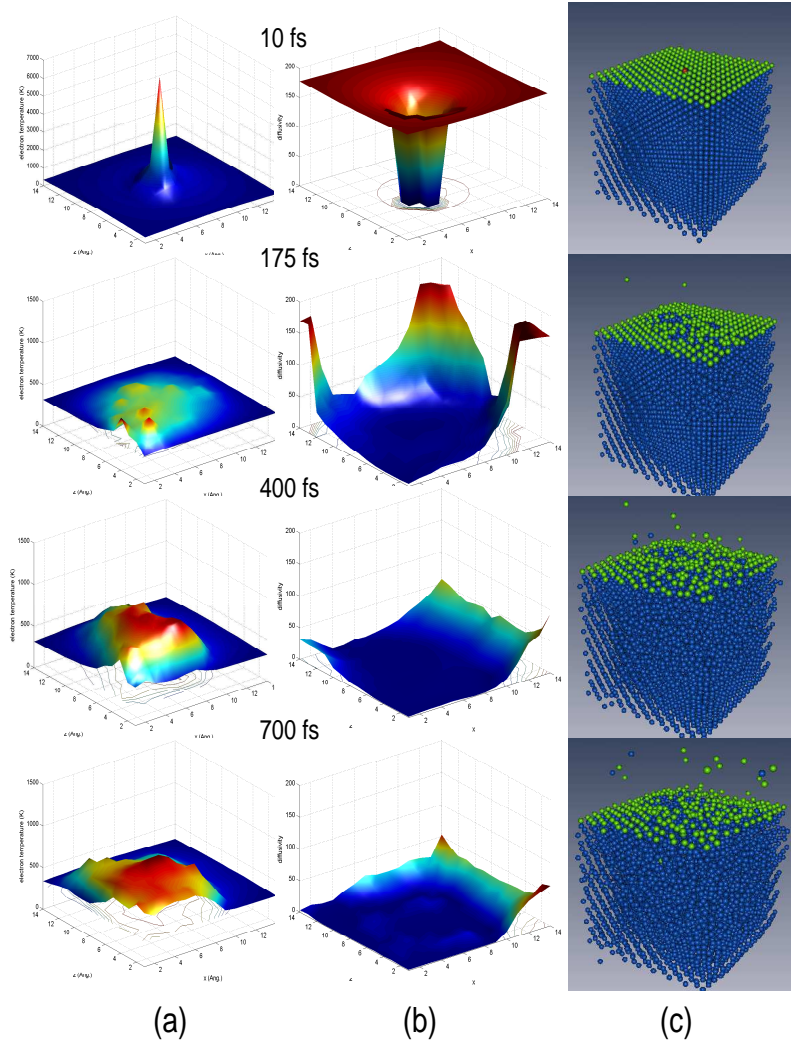


Figure 6.4: Snapshots of (a) the electron temperature T_e (K) and (b) the diffusivity D (cm^2/s) at the surface; (c) shows the corresponding trajectory pictures in a perspective view.

three-dimensional animation of the corresponding MD trajectory.”

“The first set of snapshots is taken some fs after the projectile impact, when the projectile still traverses the surface layer, thereby depositing a large amount of excitation energy at the surface. Simultaneously, the diffusivity is significantly reduced due to local lattice heating immediately around the impact point. The combination of both effects leads to a relatively high local electron temperature of about 6500 K directly at the impact point.”

At 175 fs after the impact of the primary particle, “the temporal and spatial evolution of the collision cascade has already led to sputter emission of two surface atoms as well as to a significant damage of the crystallographic order within a circular near-surface volume of approximately

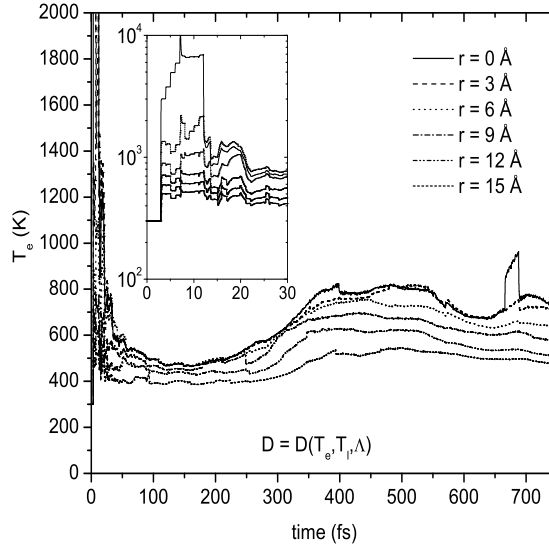


Figure 6.5: Time evolution of the surface electron temperature for different radial distances and a diffusion coefficient $D = D(T_e, T_l, \Lambda)$.

10 Å diameter around the original impact point. By inspecting the diffusivity distribution at that time, the correlation between lattice disorder and the magnitude of D becomes clearly visible. More specifically, surface areas of reduced crystallographic order - which in most cases will also be those of an above average lattice temperature - exhibit strongly reduced values of D whereas the undisturbed regions at the crystal boundaries still reveal diffusion coefficients of 150-180 cm²/s. The electron temperature at the surface exhibits a much broader distribution in connection with much smaller absolute values, mainly caused by the rapid diffusion of the original excitation. This distribution is superimposed by local excitation sources originating from fast recoil atoms moving within the surface layer.”

The following images correspond to $t=400$ fs and “reveal (i) the onset of massive sputtering and (ii) the spatial spread of the collision cascade predominantly propagating in direction towards the front-right crystal edge. Looking at the diffusivity plot, one finds a nearly homogeneous distribution with rather low values of $D \approx 0.5-5$ cm²/s. Only at the upper-right and the back boundary surface edge there are still insular peaks of high diffusivity in correspondence with the nearly undisturbed crystalline structure in these surface regions. The corresponding electron temperature distribution peaks at values around 1000 K and still shows prominent local structure reflecting the ongoing kinetic heating of the electronic sub-system by fast recoils.” Finally, at $t=700$ fs, we observe an electron temperature distribution with a maximum value slightly below 1000 K. “The location of the maximum excitation correlates with the core of enhanced collision dynamics

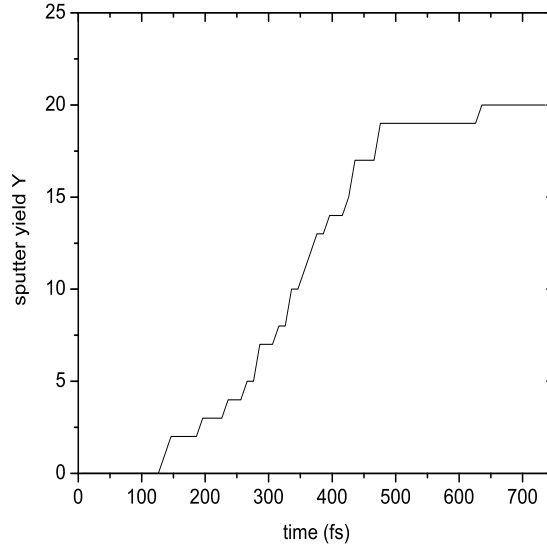


Figure 6.6: Sputter yield as a function of time. In order to define the ejection time an atom is considered sputtered as soon as it crosses a plane located at a distance of 7 \AA above the surface.

and crystallographic disorder.

To allow a better visualization of the time-dependence of surface excitation, we calculate the temporal evolution of T_e for different radial distances r from the impact point” applying the averaging procedure already outlined in the previous chapter. “The resulting distributions $T_e(t)$ are depicted in Fig. 6.5 for $r = 0, 3, 6, \dots, 15 \text{ \AA}$.

There are several interesting observations. Shortly after the impact, the predicted excitation exhibits a sharp peak of about 10 fs duration” with a maximum electron temperature of about 10000 K decreasing with “increasing distance from the impact point. After the projectile has passed the surface layer, the electron temperature is found to rapidly decay due to the onset of diffusion without any notable electronic energy source term, until at times of about 50 fs values close to room temperature are reached. Probably the most striking observation in Fig. 6.5 is the fact that, after this initial decay, the surface excitation is found to rise again, leading to a second maximum of T_e at times around 500 fs ².

This finding is of utmost importance, since it reflects the trapping of electronic excitation in a collision cascade by means of local heating and, more importantly, atomic disorder. The electron temperature reached in the later stage of the cascade is [...] sufficient to influence the ionization and

²The particular rise of T_e , which for $r = 0 \text{ \AA}$ is found approx. 680 fs after the impact, originates from one extra-ordinarily fast particle traversing the single discretization cell at $r = 0 \text{ \AA}$.

excitation processes of sputtered particles leaving the surface [4]. Moreover, the time scale at which these temperatures are reached almost perfectly coincides with that of maximum particle emission. This fact is demonstrated in Fig. 6.6, which shows the emission statistics of sputtered particles as a function of time after the projectile impact.

The temporal structure of the electronic excitation determined here can be compared to that calculated by USMAN ET AL. [121], who find a time-dependence of T_e which is qualitatively similar to that depicted in Fig. 6.2. There are, however, distinct differences that will significantly influence the ionization and excitation behavior of sputtered particles. First, the electron temperature calculated in Ref. [121] exhibits its maximum at about 100 fs after the projectile impact, i.e., much later than that depicted in Fig. 6.2. We attribute this to the rather crude assumptions regarding the particle dynamics of the collision cascade which form the basis of the kinetic excitation treatment in Ref. [121]. Moreover, the effect of local lattice disorder has not been included in Ref. [121], leading to an unrealistically fast decay of T_e at times larger than 200 fs.

6.3 Conclusion

First results obtained for a selected ion impact event reveal an interesting time structure of the kinetic electronic excitation associated with the particle dynamics in a collision cascade. Immediately following the projectile impact, we find a sharp maximum of about 10 fs width, localized directly at the impact point, where excitation energy densities are reached which translate to electron temperatures of several thousand Kelvin. While this maximum appears at much too short times to significantly influence the excitation or ionization states of sputtered particles, it may play a dominating role for projectile induced kinetic electron emission from the surface. The initial excitation is rapidly dissipated by the onset of fast heat diffusion.

If the diffusivity would remain the same as for the undisturbed crystal, this cooling would simply lead to a monotonic decay of the electron temperature on time scales of the order of 100 fs.

If, on the other hand, the local and temporal variations of the diffusivity D are taken into account, the excitation energy density is found to rise again, leading to a [...] second maximum of T_e at times of several hundred fs after the projectile impact.

We attribute this finding to the influence of local heating and, most importantly, impact-generated atomic disorder, which are shown to lead to a trapping of the electronic excitation within the crystal volume affected by the collision cascade. From an analysis of the emission statistics of the sputtering process, we conclude that it is this feature which determines the ionization and excitation probabilities of sputtered particles.”

At this point it should be underlined again, that by “utilizing the combination between MD and the electronic excitation calculation applied here, it

is in principle feasible to locate the emission of every single particle leaving the surface both in space and time and correlate its ionization probability with the electron temperature calculated at this point. This way, characteristics of secondary ion emission can be predicted which are otherwise inaccessible by MD simulations.”

Naturally, [...] there is an additional excitation mechanism by *electron promotion* in hard collisions between cascade atoms, which has been neglected in the” model presented in this chapter. “Since hard collisions can easily be identified in the MD scheme, such effects can in principle be included into our model, for instance, as an additional source term entering Eq. (6.2)” as it will be shown in the following chapter.

Chapter 7

Electronic Excitation in Atomic Collision Cascades: A nonlinear Transport Model including Electronic Friction and Electron Promotion

A shortcoming of the excitation model presented in the two previous chapters is that collisional excitations are not taken into account.

In this chapter, we develop another extension, which allows the incorporation of those processes in a straightforward manner.

The extended model is then applied to calculate the temporal and spatial excitation energy density for the identical trajectory as investigated in chapters 5 and 6. The obtained results are compared to the corresponding calculation without collisional excitations in order to estimate the relative significance of excitation by electron promotion and frictional excitation.

It should be noted here, that this chapter constitutes a compilation of the paper *Electron promotion and electronic friction in atomic collision cascades*, A. DUVENBECK, O. WEINGART, V. BUSS and A. WUCHER, New. J. Phys. 9 (2007) 38.

7.1 Description of the Model

The additional source of excitation energy to be considered, now, “is the promotion of d -electrons to energies above E_F in violent binary collisions. In a simple physical model, these excitations can be described on the basis of the curve-crossing theory of FANO and LICHTEN [8, 122, 123] originally developed for inelastic collisions in gases. In this picture, quasi-molecular

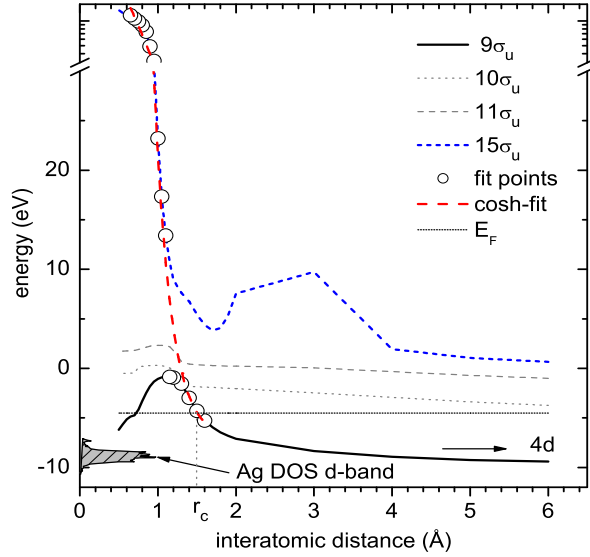


Figure 7.1: Ab-initio calculation of molecular orbital (MO) energies vs interatomic distance corresponding to a quasi-molecule consisting of two silver atoms. RHF single-point energy calculations were performed using GAUSSIAN03 [125] in 1 Å steps. In the region of strong interaction (between 2 and 0.4 Å) the step size was refined to 0.1 Å. In order to include all electrons in the mathematical description of the Ag-Ag wavefunction we have used the 3-21G standard basis rather than pseudopotentials. We note that preliminary calculations for the binary Ga-Ga System were found to be in agreement with earlier calculations carried out by LORINCIK [126]. The dotted lines constitute the diabatic MO-level constructed from the adiabatic ones by connecting the gap between the energy curves at avoided crossings with an inverse hyperbolic cosine function. The DOS-data have been taken from Ref. [127].

orbitals (MO) are transiently formed by two hard colliding atoms. As the distance of the two nuclei decreases, some orbitals may be promoted to higher energies due to the competing effect of the increased nuclear charge in the quasi-molecule with decreasing internuclear distance and the increase in kinetic electron energy caused by increased localization [124]. When two levels of the same symmetry cross in a non-adiabatic picture, exchanges between them are possible, and higher levels, unoccupied before the collision, can be partially filled.

Figure 7.1 shows ab-initio calculated adiabatic σ_u molecular orbital (MO) energies for a binary Ag-Ag collision as a function of internuclear distance. It is quite obvious that the $9\sigma_u$ MO, which in the separated atom limit corresponds to the $4d-4d$ orbital, is quickly promoted with decreasing internuclear separation thereby exhibiting avoided crossings with the energetically higher $10\sigma_u$, $11\sigma_u$ and $15\sigma_u$ MO's.

From the adiabatic molecular orbitals we derive the diabatic MO's by connecting the gap between the energy curves at avoided crossings with smooth, continuous curves which are then taken to substitute the former

ones in the crossing region. Thus, this geometrical construction, which is in analogy to the one proposed in Ref. [126], leads to a “diabatic” $9\sigma_u$ energy curve $E_{9\sigma_u}(r)$ which for the ease of computations is approximated by an inverse cosine hyperbolicus dependence $E_{9\sigma_u}(r) = a + b/\cosh(\gamma r)$ (dashed line, $a = -7.1$, $b = 1657$, $\gamma = 4.75$) as already used by SROUBEK [124].

Now, considering a violent collision within a solid metal, we are confronted with the problem, how to match the binary collision description of a promoted localized energy level with the band structure of the solid.

For that scenario, we correlate the $4d-4d$ energy level, to which the $9\sigma_u$ MO converges in the limit of large interatomic distance to the energy corresponding to the center of gravity of the density of states in the d -band of silver.

Under the assumption, that the molecular orbital energy levels originating from the localized d states for a Ag-Ag collision in the gas phase do not significantly differ from those evolving in a solid silver environment, the $9\sigma_u$ level energetically crosses the FERMI energy level at an interatomic distance r_c of 1.5 Å (see Fig. 7.1).

Thus, whenever the internuclear separation in a binary collision falls below this critical value, promoted electrons may undergo a transition from the promoted state to unoccupied levels in the continuum leaving either a localized $4d$ hole on one of the colliding atoms (binary picture) or a hole in the d band after the collision is completed.

So far, the description is identical to that employed by others in order to explain the generation of inner shell vacancies. Here, we are interested in the fate of the liberated *electron*, which may in principle end up in all possible excitation states between the FERMI level and the maximum energy corresponding to the distance of closest approach.

Assuming a resonant transition at an internuclear distance $r^* = r(t^*)$ we arrive at an additional source term

$$(E_{9\sigma_u}(r^*) - E_F) \cdot \delta(\vec{r}^* - \vec{r}) =: S_2(\vec{r}) \quad (7.1)$$

to incorporate into the nonlinear diffusion model. At this point, it is obvious, that for each hard collision occurring within the cascade, the total amount of excitation energy S_2 fed into the electronic sub-system strongly depends on the interatomic distance $r^* < r_c$ at which the transition occurs.

In order to calculate the transition probability as a function of interatomic distance, we employ the LANDAU-ZENER curve crossing formula to describe the transition from a diabatic potential energy curve to the (horizontal) free electron states in the conduction band.

Let us consider two diabatic potential energy curves crossing at r . According to the classical LANDAU-ZENER approximation the transition probability is given by

$$p(r) = \left(1 - \exp\left(\frac{-2\pi H^2}{\hbar v(r)a(r)}\right) \right), \quad (7.2)$$

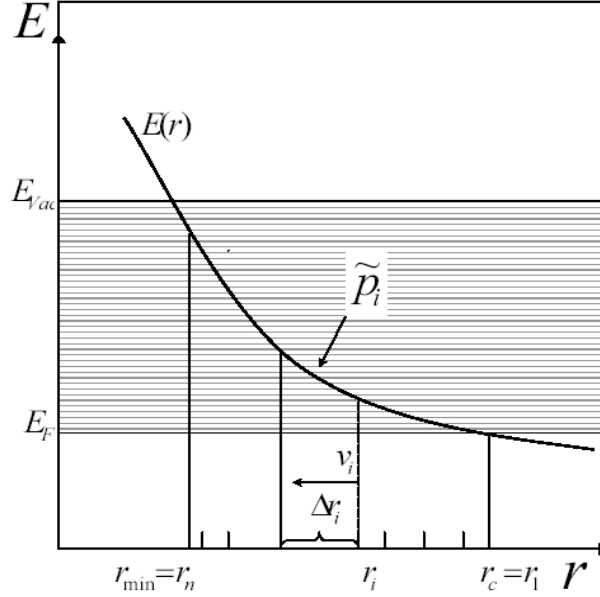


Figure 7.2: Schematic drawing of the quasi-molecular orbital intervening the conduction band

where a denotes the modulus of the difference in the derivatives of the curves, v constitutes the relative velocity of the two nuclei and the parameter H represents the transition matrix element. All quantities are evaluated at the crossing distance.

Now, let us consider the case that during a violent binary collision within a solid, one energy curve $E(r)$ - which has to be identified with the diabatic MO energy curve - overlaps with the conduction band. For the purpose of the present study, we assume the conduction band states to be a continuum of unoccupied free electron states with the FERMIE energy E_F intersected by $E(r)$ at an interatomic distance r_c .

The detailed binary collision dynamics, i.e the trajectory path $r(t)$ and the corresponding relative velocity $v(r(t))$ between r_c and the distance of closest approach r_{min} are provided by the MD simulation at discrete times t_i . Note that the time intervals $\Delta t_i = |t_{i+1} - t_i|$ and, thus, the intervals $\Delta r_i = |r(t_{i+1}) - r(t_i)| = |r_{i+1} - r_i|$, are not necessarily of equal length due to a dynamical time-step adjustment.

Then, we assume - provided that the transition has *not* taken place in any of the previous intervals Δr_j with $1 \leq j < i$ - the probability \tilde{p}_i for a transition within the i -th interval to linearly scale with the LANDAU-ZENER term (7.2) as well as with the number of states $N_i = \lfloor \Delta r_i \cdot \frac{\partial E}{\partial r} |_{r_i} \rfloor$ crossed within Δr_i . Thus, we have

$$\tilde{p}_i = \frac{1}{\xi} \cdot \left(1 - \exp \left(\frac{-2\pi H^2}{\hbar v(r_i) a(r_i)} \right) \right) \cdot \Delta r_i \frac{\partial E}{\partial r} |_{r_i} \quad (7.3)$$

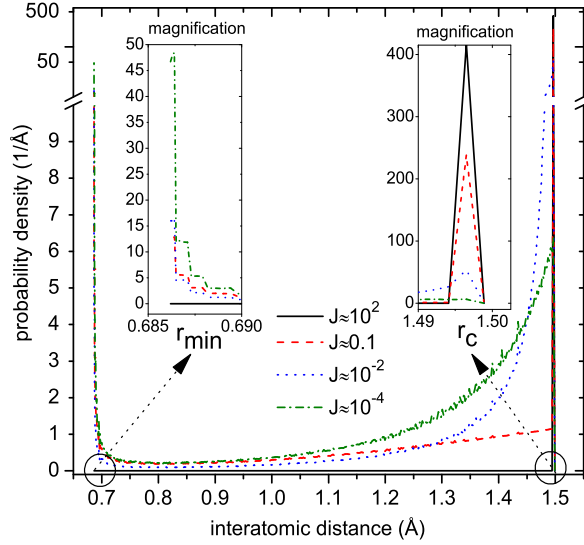


Figure 7.3: Transition probability density as a function of interatomic distance for different coupling parameters J

with

$$\xi = \max_i \left\{ \Delta r_i \frac{\partial E}{\partial r} \Big|_{r_i} \right\}. \quad (7.4)$$

In Eq. (7.3) the normalization factor ξ has to be introduced in order to be able to define the counter probability q_i as $q_i = 1 - p_i$. In order to account for the prerequisite that the transition must not have taken place in any of the preceding intervals $\Delta r_{j < i}$, the probability \tilde{p}_i has to be multiplied with a factor $\prod_{j=1}^{i-1} (1 - p_j)$, thus, leading to the recursion

$$p_i = \frac{1}{N} \cdot \frac{1}{\xi} \cdot \left(1 - \exp \left(\frac{-2\pi H^2}{\hbar v(r_i) a(r_i)} \right) \right) \times \Delta r_i \frac{\partial E}{\partial r} \Big|_{r_i} \times \prod_{j=1}^{i-1} (1 - p_j), \quad (7.5)$$

with $p_1 := \tilde{p}_1$. The normalization constant N can be determined in a straightforward way, since at r_{min} the radial velocity vanishes leading to a singularity in the denominator of the argument of the exponential function which is equivalent to a transition probability equal to one. Thus, it is clear that the transition must take place somewhere on the trajectory path from r_c to r_{min} , which is equivalent to

$$N = \sum_{i=1}^n p_i = \sum_{i=1}^n \left\{ \frac{1}{\xi} \cdot \left(1 - \exp \left(\frac{-2\pi H^2}{\hbar v(r_i) a(r_i)} \right) \right) \times \Delta r_i \frac{\partial E}{\partial r} \Big|_{r=r_i} \times \prod_{j=1}^{i-1} (1 - p_j) \right\}.$$

Figure 7.3 displays the calculated transition probability density $p_{dens}(r)$, i.e. $p_i/\Delta r_i$, as a function of radial interatomic distance for different coupling parameters $J := H^2/\overline{\hbar a(r)v(r)}$.

In the case of *strong* coupling of the quasi-molecular orbital with the continuum states (i.e. $J = 10^2 \gg 1$) the resulting probability density distribution is a delta-function centered at the critical distance r_c , i.e. the electron will be fed into the conduction band directly at the FERMI edge provided that there are unoccupied states, of course. Thus in this case the electron promotion process does not lead to the formation of an “hot electron” in the conduction band.

With decreasing coupling strength ($J \approx 0.5$) the delta peak loses approximately one half of its height in favor of the evolution of a small peak at the turning point r_{min} as well as in favor of a non-zero probability density in the intermediate region between r_c and r_{min} . Comparing $p_{dens}(r_c)$ with $p_{dens}(r_{min})$ one observes that a transition at the FERMI edge is by one order of magnitude more probable than a transition at the turning point.

Considering the case of *weak* coupling (i.e. $J = 10^{-2} \ll 1$), we still observe a rather high probability density of approximately 20 \AA^{-1} at r_c which is followed by a steep exponential-like decay up to an interatomic distance of approximately 0.9 \AA . Directly at the turning point, the transition probability density again exhibits a second very sharp maximum, which, now, exceeds the one localized at r_c by a factor of two. Thus, for that particular choice of J , a transition at the turning point - which “generates” a hot electron in the conduction band - appears to be more probable than a transition directly at the FERMI edge.

Finally, Fig. 7.3 displays the resulting distribution for very low coupling constant $J \approx 10^{-4}$. It is clearly visible that for this particular choice of J the probability for a transition to occur at the turning point is by two orders of magnitude larger than to occur at r_c . In the limiting case $J \rightarrow 0$ the corresponding distribution will converge to a delta function localized at the turning point.

Thus, the above analysis demonstrates the strong dependence of $p(r)$ on the coupling matrix element H , which in the present study constitutes a parameter that is associated with a high level of uncertainty. In order to estimate the maximum possible excitation energy and due to the fact that the present study of one singular trajectory does not provide enough collision statistics for the implementation of an inhomogeneous probability distribution, we assume for each hard collision the electron promotion event to take place at the distance of *closest* approach r_c with *unit* probability, provided that $r_{dca} < r_c$, of course. Thereby, this procedure allows to give an *superior estimate* of the maximum possible total excitation energy generated by electron promotion processes during the cascade.

We emphasize that - for the sake of consistency with energy conservation - the generated excitation energy is subtracted from the total energy within the molecular dynamics calculation. In analogy to Ref. [89], this is done for each violent collision by symmetrically shifting the interatomic distance of the colliding atoms by an amount that lowers the potential energy between them by a value corresponding to the generated excitation energy above the FERMI level. This correction is performed one molecular dynamics

time step after the distance of closest approach has been reached.

We note that the electron transition from the promoted level to an unoccupied state in the conduction band is naturally accompanied by the simultaneous creation of a d -hole in the valence band. Due to the relatively narrow width of the silver $4d$ band, along with the fact that the crystallographic order is heavily disturbed during most of the collision cascade, these d -shell excitations will remain localized on the specific atom where they have been created on a time scale of at least femtoseconds. At larger times, the d -hole will be shared among neighbored atoms and delocalize. However, the decay of d holes represents another source of excitation energy” which is not considered here.

The nonlinear transport of excitation energy as well as numerical implementation details have already been discussed in chapter 6. Therefore, at this point we only give the modified nonlinear diffusion equation describing the spread of electronic excitation energy around the original point of generation. The corresponding equation reads

$$\begin{aligned} \frac{\partial E(\vec{r}, t)}{\partial t} - \vec{\nabla} \cdot (D(T_l(\vec{r}, t), T_e(\vec{r}, t), \Lambda(\vec{r}, t)) \vec{\nabla} E(\vec{r}, t)) = \\ A \sum_{i=1}^N E_k^i(\vec{r}_i, t) \cdot \delta(\vec{r}_i(t) - \vec{r}(t)) + \\ + \sum_{\kappa} \frac{E_{g\sigma_u}(r_{dca}^{(\kappa)}(t)) - E_F}{\Delta t} \cdot \delta(t - t_{dca}^{(\kappa)}) \cdot \delta(\vec{r} - \vec{r}_{dca}^{(\kappa)}) \end{aligned} \quad (7.6)$$

with an excitation energy diffusivity D , which is for each time self-consistently determined from the lattice temperature T_l , the electron temperature T_e itself and an additional lattice order parameter Λ as already discussed in detail in section 6.1.1. “Note that the last sum in Eq. (7.6) with index κ loops over all hard binary collisions.

Equation (7.6) is numerically solved within the complete half-space below the surface using” the finite differences approach outlined in section 6.1.2. “At the surface plane itself a NEUMANN boundary condition is enforced in order to inhibit outward diffusion of excitation energy into the vacuum. It should be noted that this boundary condition neglects the energy loss induced by electron emission from the surface. Under the bombarding conditions employed here, however, typical electron emission yields are of the order of unity with typical emission energies being of the order of eV. This means that on the average only one electron is emitted during the entire simulation, rendering this energy loss negligible.

7.2 Results

The above combination of molecular dynamics and nonlinear diffusive transport of excitation energy has been applied to calculate the time and space

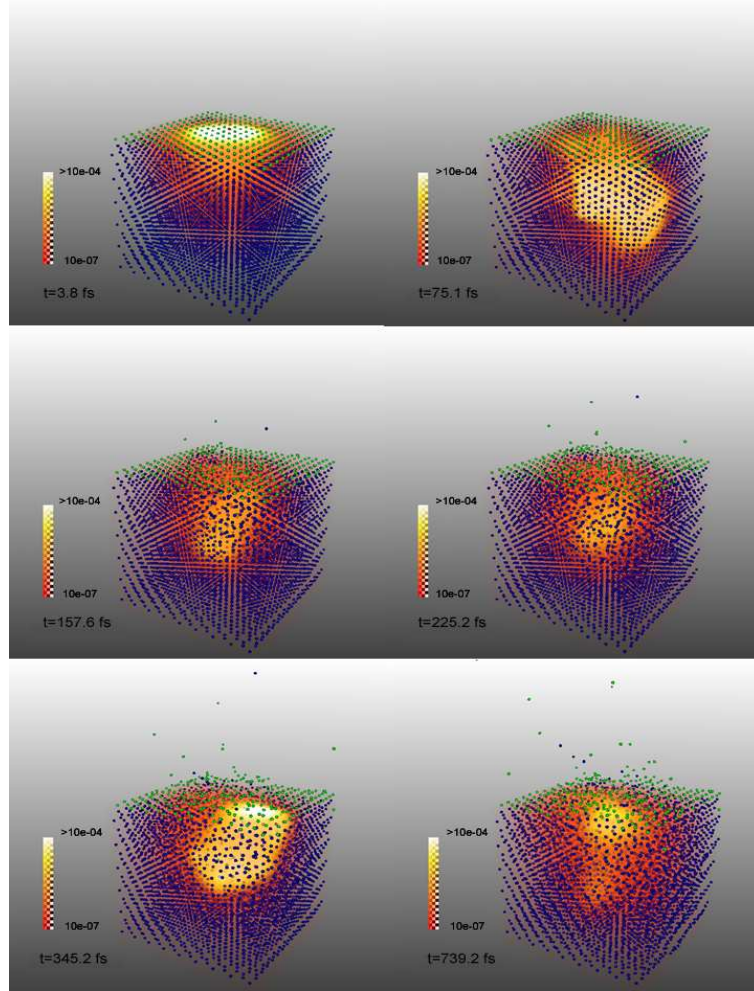


Figure 7.4: Temporal snapshots of the exemplary collision cascade initiated by 5-keV $\text{Ag} \rightarrow \text{Ag}(111)$ bombardment. In addition to the illustration of atomic particles (*blue*: bulk atoms; *green*: surface atoms) the local excitation energy density ($\text{eV}/\text{\AA}^3$) is visualized using the indicated colormap.

resolved excitation energy density within the atomic collision cascade initiated by a 5-keV silver atom impinging onto an $\text{Ag}(111)$ surface under normal incidence.

In order to study the relative role of the two excitation mechanisms (electronic friction + electron promotion) the calculations are carried out (i) *with* as well as (ii) *without* the collisional source term S_2 . The temporal and spatial evolution of the electronic excitation energy density will be discussed in respect of the ionization probability of sputtered particles and kinetic electron emission.

In order to get an [...] impression of how the atomic collision cascade studied here develops in time and space, Figure 7.4 shows perspective snapshots of the simulation volume at different stages after the projectile

impact for the calculation including electron promotion. Simultaneously to the atomic particles, which are diagrammed as small colored balls, the electronic subsystem is represented by a gas cloud whose colorization reflects the momentary local excitation energy density as calculated by Eq. (7.6).

The first snapshot is taken shortly after the primary particle (red color) penetrated the uppermost crystal layer (green color) under normal incidence. At that time, the highly energetic projectile is the only atom which is not at rest and, thus, the only particle transferring part of its kinetic energy into the electronic subsystem via electronic friction. Due to the still undisturbed lattice the transport of excitation energy takes place very rapidly ($D \approx 180 \text{ cm}^2/\text{s}$) without any preferences in lateral direction. In direction perpendicular to the surface plane, however, any flux of excitation energy in outward direction is inhibited by NEUMANN boundary conditions, whereas diffusion in bulk direction is not restricted at all. These symmetries directly transfer to the resulting distribution $E(\vec{r}, t)$ which clearly exhibits radial symmetry around the impact point and peaks at an excitation energy density of approx. $5 \times 10^{-3} \text{ eV}/\text{\AA}^3$ in its center of symmetry. Note that all excitation energy generated so far solely originates from electronic friction, since the primal electron promotion event occurs 2 fs after this snapshot was taken.

The next picture taken at $t = 75 \text{ fs}$ shows a crystal which appears to be almost undisturbed apart from some defects in the uppermost surface layer. The excitation energy distribution strongly deviates from the one at $t = 5 \text{ fs}$ in mainly two points. First, the lateral symmetry is broken and, secondly, the maximum of excitation energy density is no longer located in the uppermost surface layer at the impact point, but in approx. 12-15 \AA depth near the front-right crystal edge. This finding already indicates that the collision cascade predominantly propagates in that particular direction beneath the surface, thereby continuously heating up the electron gas. Unfortunately, in this representation of calculation results it is not possible to distinguish between excitation energy generated by electronic friction or electron promotion, respectively. This issue will be analyzed and discussed in a separate figure in the course of the present” chapter.

“The subsequent snapshot at $t \approx 150 \text{ fs}$ reveals the onset of sputtering with a total number of three particles already been emitted from the surface, which electronically has cooled down to excitation energy densities of approx. $3 \times 10^{-5} \text{ eV}/\text{\AA}^3$ at the impact point due to (i) rapid transport of excitation energy in bulk direction and (ii) an additional lack of particles passaging the near sub-surface region. Moreover, the observation of plenty of particles knocked out from their original lattice sites at the right-front edge of the crystallite corroborates our aforementioned speculation about the direction of propagation of the cascade beneath the surface.

At $t = 225 \text{ fs}$ the excitation energy distribution $E(\vec{r}, t)$ remains rather moderate with excitation energy densities of about $4 \times 10^{-5} \text{ eV}/\text{\AA}^3$ at the surface which correspond to electron temperatures of about 500-600 Kelvin. Concerning particle dynamics eight atoms have already been sputtered from

the very surface.

At a later time of about 300 fs, we interestingly observe a rise in excitation energy density particularly at the very surface, again. This effect must be ascribed to the augmented presence of secondary recoils in the proximity of the surface plane. In addition, the local atomic disorder induced by the projectile impact leads to a significant reduction of the excitation energy diffusivity by two orders of magnitude. Therefore, the electronic excitation generated by the persisting frictional source term becomes trapped within the crystal volume perturbed by the collision cascade. This leads to the occurrence of local “hot spots” of electronic excitation, which may exhibit peak temperatures T_e of about 1000 K and last some hundreds of fs during the late stage of the cascade (see last snapshot). We note that these “hot spots” temporally overlap with the emission of particles from the surface. Particularly those atoms sputtered from these excited surface areas may constitute the fraction of secondary ions among the entire flux of sputtered particles.

A look at the last snapshot at the end of the total simulated time of $t = 750$ fs reveals that with increasing time the excitation energy density will naturally decrease due to the continuous decrease in the frictional source term, which is attended by additional kinetic energy losses in the form of sputtered particles and naturally superimposed by the dissipation of excitation energy in bulk direction, which can no longer be (over)compensated by an enhanced trapping of electronic excitation.

In summary, the qualitative analysis of the series of snapshots reveals the necessity to distinguish between two different stages of high density of excitation energy at the surface. First, directly after the projectile hit the surface, an isotropic “hot spot” develops around the point of impact. This “hot spot” breaks down on a time scale of several ten fs due to the onset of fast diffusion and therefore will not have any direct effect on the electronic charge state of by far the majority of sputtered particles, which leave the surface at much later times. However, we consider this initial highly excited area to be responsible for kinetic electron emission (KEE). The second kind of “hot spot” attributed to the increased confinement of electronic excitation in the later stage of the cascade strongly coincides with the sputtering of secondary recoils and, therefore its momentary electron temperature at the position a particle has been emitted from must be regarded as the crucial parameter for the determination of the individual ionization probability of that particular particle.

In view of the fact that the majority of particles are emitted from the uppermost surface layer [29], Fig. 7.5 focuses on the time evolution of the excitation energy densities at the surface for the calculations *with* and *without* collisional excitation. In order to allow a rather compact quantification of results, Fig. 7.5 shows the excitation energy density evaluated at two different radial distances from the impact point.

Before analyzing and comparing the calculation results in detail, we emphasize that the MD trajectories corresponding to both cases differ from

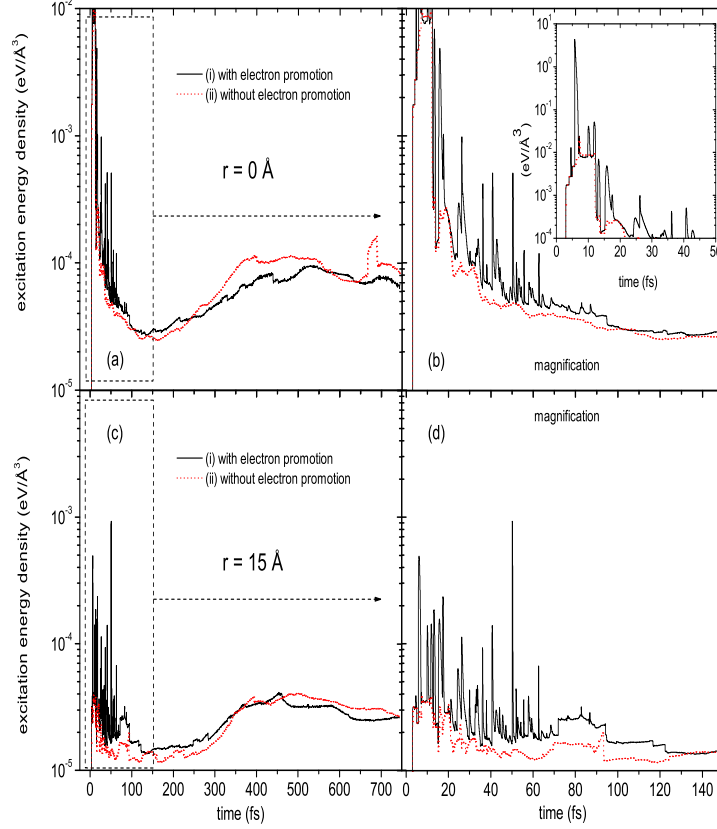


Figure 7.5: Time evolution of the excitation energy density at the surface for two different radial distances from the impact point of the 5-keV silver projectile impinging onto Ag(111). The diffusivity D varies in time and space as a function of lattice temperature, atomic disorder and excitation energy density.

each other as a matter of principle, since for every electron promotion process the collisional excitation energy is subtracted from the potential energy of the colliding atoms, thereby altering the subsequent cascade evolution. We note that these differences in particle dynamics influence the obtained sputtering yield, which is $Y = 21$ for the calculation *with* and $Y = 19$ for the calculation *without* electron promotion.

Focusing on the trajectory simulated without electron promotion, we observe a steep initial rise of E up to a maximum value of about $2 \cdot 10^{-2} \text{ eV}/\text{\AA}^3$ at $t \approx 7 \text{ fs}$. This initial maximum originates from the projectile penetrating the first layer of the model crystal and is followed by a fast monotonic decay to values of about $2.6 \cdot 10^{-4} \text{ eV}/\text{\AA}^3$ at $t = 12 \text{ fs}$ after the primary particle has completely passed the uppermost layer. The extremely strong decay clearly mirrors the rapid transport of excitation

energy at that early stage of the cascade. After the occurrence of a second maximum at $t \approx 15\text{-}20$ fs, which we ascribe to a fast recoil moving across the uppermost surface layer, the excitation energy density exponentially decreases - apart from some distinct fine structure from insular secondary recoils - up to a simulated time of approximately 150 fs. Shortly after, the excitation energy density at the surface increases again by almost one order of magnitude, a finding which is due to the enhanced confinement of electronic excitation within the cascade volume. At $t > 350$ fs, $E(t)$ exhibits a rather constant, plateau-like curve characteristics with values of about 1×10^{-4} eV/Å³, which translate to electron temperatures of about 800 K. For a larger radial distance from the impact point ($r = 15$ Å), Fig. 7.5 reveals similar curve characteristics with by far less pronounced maxima. The electron temperatures in the range from 250-750 fs are by one half of a magnitude lower than those calculated at $r = 0$ Å. However, one has to bear in mind that, dependent on the momentary lateral position at the surface, even temperatures above 1000 K are possible in local “hot spots” as shown in Fig. 7.4.

Now, considering the calculation including electron promotion, the corresponding curves are within the first 150 fs rather similar to those of the case *without* collisional excitation, but additionally exhibit a set of sharp peaks. These structures originate either from electron promotion processes, which may occur either at that particular radial distance from the impact point, or, more likely, from contributions of collisional excitation generated somewhere else in the cascade. Within the first tens of fs after the impact, the curves calculated *without* collisional excitation may be regarded as the inferior enveloping functions of the curves representing the calculation including electron promotion. At $t = 7$ fs at $r = 0$ Å one observes a very steep peak evolving from the plateau of the initial maximum with an excitation energy density of 6 eV/Å³. This peak can be ascribed to the initial violent collision of the projectile with a target atom localized at the impact point in the uppermost surface layer. Moreover the detailed collision analysis of the MD-trajectory reveals that for this particular collision the distance of closest approach is 0.67 Å, which is equivalent to an excitation energy of 127 eV. A close look at the fine-structures of the peaks reveals an characteristic fast exponential decay at the right slope, mirroring the fast transport of excitation energy, which can also be derived from the observation that there is hardly any temporal shift in the peaks from $r = 0$ Å to $r = 15$ Å. As a general tendency the peak heights as well as their occurrences decrease with increasing time as a consequence of successive partitioning of kinetic energy among the particles. The latest electron promotion process takes place 140 fs after the primary particle impact.

Taking into account the time interval from 100-750 fs, we again find an increase of excitation energy density in the time interval most particles are sputtered within. However, for both radial distances, the rises are retarded as well as less pronounced compared to those obtained without the collisional source term. This finding clearly reflects the fact that for

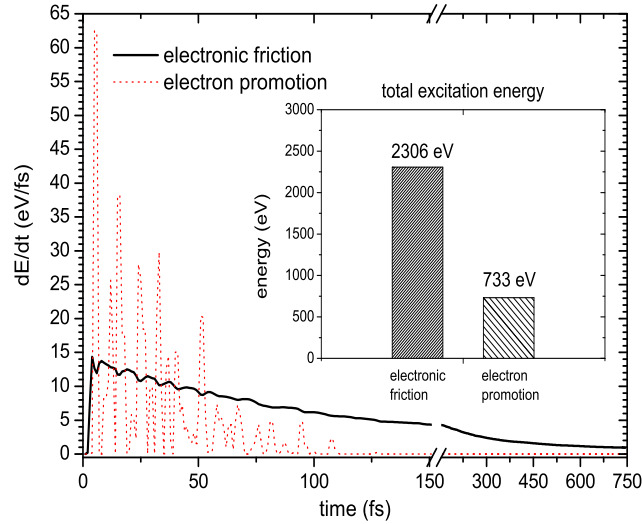


Figure 7.6: Volume-integrated source terms (solid line: electronic friction; dotted line: electron promotion) as a function of time after the projectile impact. The sub-window shows the total excitation energy generated within the first 750 fs after the initialization of the cascade.

each collision the excitation energy is subtracted from the potential energy of the colliding atoms, which, in turn, is converted into a - in comparison to an analogous elastic collision - diminished amount of kinetic energy. Integrated over all inelastic collisions, this leads to a significant reduction of the frictional source term. In order to determine the relative significance of both excitation mechanisms, the source terms dS_1/dt and $S_2/\Delta t$ have been integrated over the complete model crystallite volume in timesteps of $\Delta t = 1$ fs. The resulting time evolution of the source terms is depicted in Fig. 7.6.

Directly after the impact, when the projectile penetrates the uppermost cell layer, the electronic friction source term raises to values of about 14.4 eV/fs. This maximum corresponds to the situation where the bombarding energy has not yet been shared among the atoms and not been partially transformed into potential energy either. The initial rise is then followed by a rather slow exponential decrease of the frictional source term to values of about 2 eV/fs at $t = 750$ fs. The observed oscillatory structure in the time interval 0-50 fs reflects the conversion of kinetic into potential energy in close collisions, a finding which is corroborated by the fact that each minimum of kinetic energy is accompanied by a maximum of the electron promotion source term. With increasing time these oscillations disappear due to enhanced partitioning of energy among more and more particles, making violent collisions less and less probable.

Having a look at the source term $S_2/\Delta t$ resulting from collisional excitations, we observe distinct peaks decreasing in height with increasing time. Each peak mirrors the promotion of a deep-level electron into an excited state above the FERMI level. This process becomes more and more improbable with enhanced kinetic energy dissipation and partitioning. The last electron promotion process occurs 127 fs after the impact of the primary particle and generates a hot electron at 0.4 eV above the FERMI level. Comparing the two datasets we observe interesting features:

(i) Both excitation mechanisms exhibit completely different temporal dynamics. The occurrence of collisional excitation events is limited to short times (≈ 100 fs) after the projectile impact, whereas electronic friction constitutes a continuous source term lasting throughout the entire simulated time interval. Hence, the significance of the electron promotion mechanism for secondary ion formation in sputtering appears to be negligible, since by far the majority of particles are emitted at much later times. (ii) Time integration of both source terms reveals that for times shorter than about 65 fs, electron promotion may constitute the dominating excitation process, at least within the upper estimate implied by our model assumptions.

This finding is interesting in the context of kinetic electron emission (KEE) [128, 129] whose basic mechanisms and their relative significance are being actively discussed [130, 126, 131, 132, 42]. Very recently, the relevance of electron promotion has not only been experimentally demonstrated for grazing incidence scattering of rare gases from a metal surface [131], but also observed for KEE from Al surfaces under bombardment with 1-8 keV Kr^+ ions [130]. Therefore the calculation results presented in Fig. 7.6 may be treated as an additional indication for the prevailing role of electron promotion processes in ion-induced KEE.

(iii) The probably most relevant observation in Fig. 7.6 is the fact that - summed over electronic friction and electron promotion - about 3 keV of energy have been transferred into the electronic subsystem of the metal. Thus, over 60 % of the kinetic energy originally imparted into the solid surface is dissipated into electronic degrees of freedom rather than by nuclear collision dynamics.

We emphasize that this statement does not contradict the common notion that nuclear stopping exceeds electronic stopping by approximately one order of magnitude for the bombarding conditions studied here. To illustrate this, let us look at the first stopping process, which is given by the impact of the projectile onto the central surface atom. A detailed analysis of the MD data [133] shows that in this collision the projectile loses about half of its kinetic energy (2500 eV), thereby generating a total of about 200 eV of excitation energy by electronic friction and electron promotion. Hence, the original electronic stopping power experienced by the projectile amounts to approximately 8 % of the nuclear stopping power, which is in accordance with the results of Monte-Carlo computer simulations using SRIM 2003 [134].

7.3 Conclusion

We present an extended computer simulation model for the calculation of electronic excitation energy densities $E(\vec{r}, t)$ in atomic collision cascades in metals. This model treats *electronic friction* as well as *electron promotion* in close binary encounters as local and time-dependent sources of excitation energy, which is assumed to spread around the original point of generation according to a nonlinear three dimensional transport equation. The latter is numerically integrated in combination with molecular dynamics delivering the atomistic particle kinetics.

The resulting four dimensional excitation energy density profile $E(\vec{r}, t)$ reveals the temporal evolution of two different kinds of “hot spots”, i.e. highly electronically excited sub-areas of the model crystallite.

The *first* “hot spot” with excitation energies from 10^{-3} -1 eV/Å³ arises directly at the particle impact, when the projectile penetrates the uppermost crystal layer. The physical mechanism prevailingly contributing to the generated excitation energy appears to be electron promotion by close binary encounters. Due to the rapid excitation energy transport at that initial stage of the atomic collision cascade, this primary “hot spot” dissolves on the time scale of several ten fs and, therefore, will not significantly influence the formation of secondary ions, which are known to be sputtered mostly at a much later stage of the cascade. Nevertheless, this initial “hot spot” coincides with ion-induced kinetic electron emission (KEE) and, consequently, it is feasible to assume that - at least for comparable bombarding scenarios as studied here - the latter phenomenon may primarily be governed by electron promotion.

The *second* kind of “hot spot” emerges at times of approx. 300 fs after the projectile impact and is restricted to the very surface. This second maximum of excitation energy density results from an enhanced confinement of excitation energy in particular that area, which has been affected most by the collision cascade. The calculations clearly show strong correlations between the presence of such a “hot spot” and spatial and temporal emission characteristics of sputtered particles. Hence, we believe that it is exactly that coincidence which is of utmost relevance for the formation of secondary ions.

Moreover, we find that about 60 % of the kinetic energy imparted into the solid is dissipated into electronic degrees of freedom rather than the collision dynamics. While within a time window of about 50 fs electron promotion constitutes the dominant excitation mechanism, on the timescale of 1 ps electronic friction turns out to govern kinetic energy dissipation into the electronic system.”

Chapter 8

Energy Partitioning in Atomic Collision Cascades

In this chapter, we apply the model presented in chapter 7 to get a time-resolved picture of how the kinetic energy originally imparted into the solid, is distributed among the nuclear and electronic degrees of freedom.

It will be seen that a sizeable fraction of the original kinetic energy is dissipated into electronic excitation. The influence of this energy drain on the particle dynamics in the cascade will be briefly discussed.

It should be pointed out here that the contents of the present chapter were already presented at the *Conference of Computer Simulation of Radiation Effects and Defects in Solids (COSIRES), Richmond (USA) 2006* and have already been published in the article *On the role of electronic friction and electron promotion in kinetic excitation of solids* by A. DUVENBECK, O. WEINGART, V. BUSS and A. WUCHER appeared in *Nucl. Instr. and Meth. B* 255 (2007) 281.

8.1 Description of the Calculation

Again, the numerical integrations of the Newtonian equations of motion in combination with Eq. (7.6) have been carried out for the same impact of a 5-keV Ag atom onto an Ag(111) surface under normal incidence. In order to investigate the effect of the electronic friction and electron promotion on particle dynamics and energy partitioning, the calculations are repeated switching the collisional excitation mechanism on and off. Due to the extremely small time steps employed in the numerical treatment, the time window considered here is again restricted to a total simulated time of 750 fs.

8.2 Results

The calculations reveal that within the time window from 0-750 fs, a total number of 33 atoms are emitted from the surface, if electronic energy losses

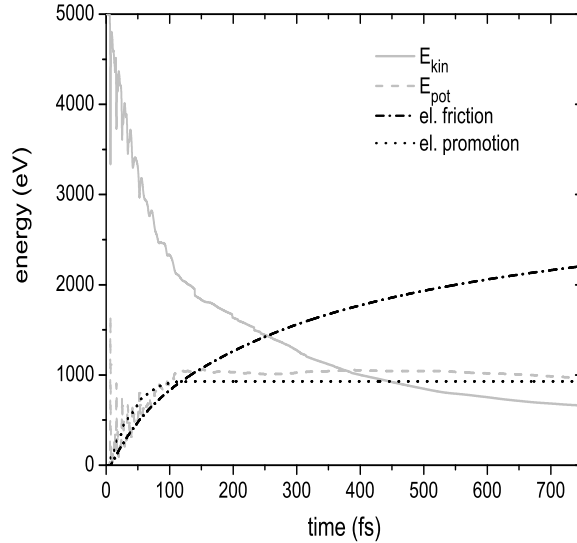


Figure 8.1: Temporal evolution of electronic excitation energy generated by (i) electronic friction, (ii) electron promotion as well as total kinetic and potential energy contained in collision dynamics. All energies are integrated over the entire simulation volume.

are completely neglected in the particle kinetics. However, there “are further emission events observed at longer times (up to several picoseconds after the projectile impact increasing the overall sputter yield for this particular trajectory to 48 atoms (\rightarrow page 59).

If electronic friction is turned on, analysis shows that at 750 fs about 2300 eV is lost from the total (kinetic and potential) energy of the atoms in the model crystallite into the electronic subsystem. At the same time, the number of atoms ejected at 750 fs” turns out to decrease from 33 to 19. If, in addition, the electron promotion mechanism is activated, another 720 eV are lost from the total energy and the resulting sputter yield (at 750 fs) is changed from 19 to 21. This increase does not constitute a contradiction, since the substantial kinetic energy loss of highly energetic colliding atoms in the initial stage of the cascade, may, for instance, alter the direction of propagation of certain branches of the collision cascade in an advantageous way with respect to the total sputtering yield. However, we conclude that - at least for the particular impact event considered here - the influence of electronic excitation “cannot be neglected in the description of the collision dynamics. This finding is in accordance with the observation of others [89]. The temporal behavior of the energetics involved in kinetic excitation is displayed in Figs. 8.1 and 8.2. Here, the total excitation energy transferred to the electronic subsystem by means of the two different mechanisms is compared with the total kinetic and potential energies contained in the simulated volume. First, it is seen that the time structure of both exci-

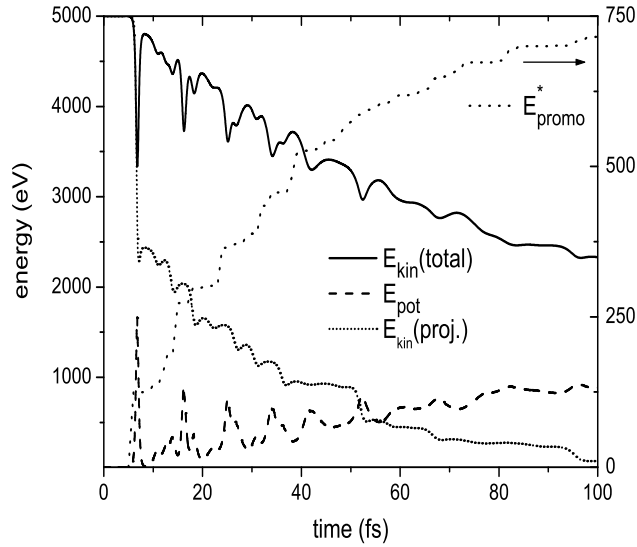


Figure 8.2: Volume integrated total kinetic and potential energy as well as electronic excitation energy produced via electron promotion vs time after projectile impact. The dash-dotted line represents the kinetic energy of the projectile alone.

tation mechanisms is very much different. While the influence of electron promotion is restricted to very short times after the projectile impact, electronic friction persists to feed the electronic excitation throughout entire simulated time interval. The physics behind the different behavior is easily understood by looking at energetics displayed in Fig. 8.2.

Each hard collision leading to electron promotion can be clearly identified by a local maximum of the potential energy, accompanied by a local minimum of the kinetic energy. These extrema manifest the distance of closest approach, where excitation energy is fed into the electronic system. Both the frequency of such hard, level promoting collisions and the energy involved in them strongly decrease with increasing time, since the fraction of high energy particles in the system is reduced due to nuclear stopping.”

In agreement with the results from Fig. 7.6 of the preceding chapter, we again note that “the electron promotion mechanism appears to be the dominant source of excitation for times shorter than about 100 fs, but ceases to work at larger times. This finding is interesting, since practically no atom is sputtered prior to 100 fs and therefore the influence of this mechanism on excitation or ionization probabilities of emitted species may be expected to be low. At later stages of the collision cascade, electronic friction takes over and continues to drain energy from the particle motion up about a ps after the projectile impact. At this time, the total kinetic energy contained in the system has reduced to about 0.7 keV. About 1 keV of energy is stored in potential energy, reflecting the lattice disorder induced by breaking the

bonds between substrate atoms. Comparing the average potential energy per atom with the latent heat of melting of Ag (0.11 eV/atom), one finds that at 750 fs the entire simulation volume is completely amorphized, a finding which is corroborated by an inspection of the lattice disorder parameter Λ .

The nearly equipartition of kinetic and potential energy suggests that the system reaches some sort of local and transient “quasi-equilibrium” on the picoseconds time scale.

Probably the most important observation in Fig. 8.1 is the fact that the total kinetic and potential energy represent only a small fraction of the energy originally introduced into the system. Summed over electronic friction and electron promotion, about 3 keV of energy have been transferred into electronic excitation at 750 fs after the projectile impact. From this result, it is evident that the majority of the kinetic energy originally imparted to the system is dissipated into electronic degrees of freedom rather than by the collision dynamics.

At first sight, this finding appears surprising, since it was generally believed that electronic stopping plays only a minor role as compared to nuclear stopping in the energy regime explored here. In fact, both statements are not in contradiction. This can be shown by plotting the kinetic energy of the projectile as a function of time (dash-dotted line in Fig. 8.2). It is seen that the projectile loses about half of its kinetic energy (2500 eV) in the first violent collision, thereby transferring about 175 eV of excitation energy into the electronic subsystem. Hence, the electronic stopping power amounts to about 7% of that of nuclear stopping. This value is in good agreement with the results of Monte Carlo computer simulations using the SRIM 2003 code [134]. On the transient stage corresponding to the picosecond time scale, however, most of the kinetic energy (62%) imparted to the surface is converted into electronic excitation.

We believe that these findings will not be changed even if a more realistic potential function is used to describe the interaction between an excited atom and the remaining solid atoms, since the density of excited atoms is so low that the overall dynamics will not be influenced very much.

Moreover, the energy transfer back from the electronic degrees of freedom to the particle dynamics by electron–phonon coupling is negligible on the time scale explored here, since the electron “temperature” (as derived from the excitation energy density and the heat capacity of the electron gas) never exceeds the lattice “temperature” (as evaluated from the average kinetic energy of the atoms) as it has been shown earlier.

It is clear that in the limit of long times electron–phonon coupling will start to thermalize the system, bringing most of the energy back into phonons again.

8.3 Conclusion

The simulations performed here generate the surprising result that most of the kinetic energy introduced into the surface by fast particle bombardment is dissipated into electronic degrees of freedom rather than the collision dynamics.

As a consequence, we conclude that collective electronic excitation plays a dominant role in the energy dissipation processes induced by the particle impact.”

Chapter 9

Conclusion

A model has been developed which allows to incorporate electronic excitations into standard computer simulations of atomic collision cascades induced by keV particle bombardment onto a solid surface. In this model, the atomic motion following the particle impact is calculated by a classical molecular dynamics approach.

In the first developmental stage of the model, the transfer of kinetic into electronic excitation energy is described in terms of a friction-like electronic energy loss experienced by all moving atoms in the solid, thus, yielding a space- and time-dependent density of electron-hole pair excitation energy generated in the cascade. This energy is supposed to spread around the original point of excitation with a diffusivity D . The latter turns out to be the essential input parameter entering the transport model. It is shown that for reasonable values of D the excitation energy density at the surface may reach values of the order of several thousands of Kelvin, thus, demonstrating that the frictional excitation mechanism may influence the formation of ions and excited atoms in sputtering.

In order to acknowledge (i) the local lattice disorder within the cascade volume and (ii) the cascade-induced lattice heating, the model has been extended to a space- and time-dependent diffusivity D , which is at each time self-consistently determined from the local lattice temperature, local electron temperature and a newly introduced local lattice order parameter. In doing so, the corresponding diffusion equation becomes strongly nonlinear and requires a complex numerical treatment, which has been realized by a sophisticated combination of finite-differences and GREEN's function methods.

The application of this nonlinear transport model to an exemplary collision cascade initiated by the impact of a 5 keV silver atom onto an Ag(111) surface reveals an interesting time structure of the electron temperature at the surface: Directly following the primary particle impact, a very sharp initial peak of an electron temperature of several thousands of Kelvin is observed at the impact point. This peak is rapidly dissipated away due to the onset of fast diffusion in the structurally unperturbed crystal and,

therefore, appears to be non-relevant for secondary ion formation. However, this particular peak may play a dominant role for electron emission from ion-bombarded surfaces. After times of about 50 fs the electron temperature is found to be close to room temperature. The surface excitation is found to increase again, leading to a second maximum of T_e at times around 500 fs. This finding is of utmost importance, since it reflects the trapping of electronic excitation in a collision cascade by means of local heating and, more important, atomic disorder. The electron temperature reached in the later stage of the cascade is clearly sufficient to influence the ionization and excitation processes of sputtered particles leaving the surface. Moreover, the time scale at which these temperatures are reached coincides almost perfectly with that of maximum particle emission.

In a third step, electron promotion processes in close atomic collisions - which are identified within the MD-calculation - have been incorporated into the model as a second excitation mechanism. Electron promotion is treated in terms of diabatic correlation diagrams of quasi-molecular orbital energies, which for a homonuclear collision of two silver atoms are constructed from adiabatic ab-initio calculations. On the basis of the LANDAU-ZENER formalism, the probability that an electron is promoted into the conduction band during a hard collision has been examined as a function of interatomic distance. In order to arrive at an upper estimate for the contribution of electron promotion processes to the total amount of kinetically induced excitation, for each violent binary encounter the transition is assumed to occur at the distance of closest approach.

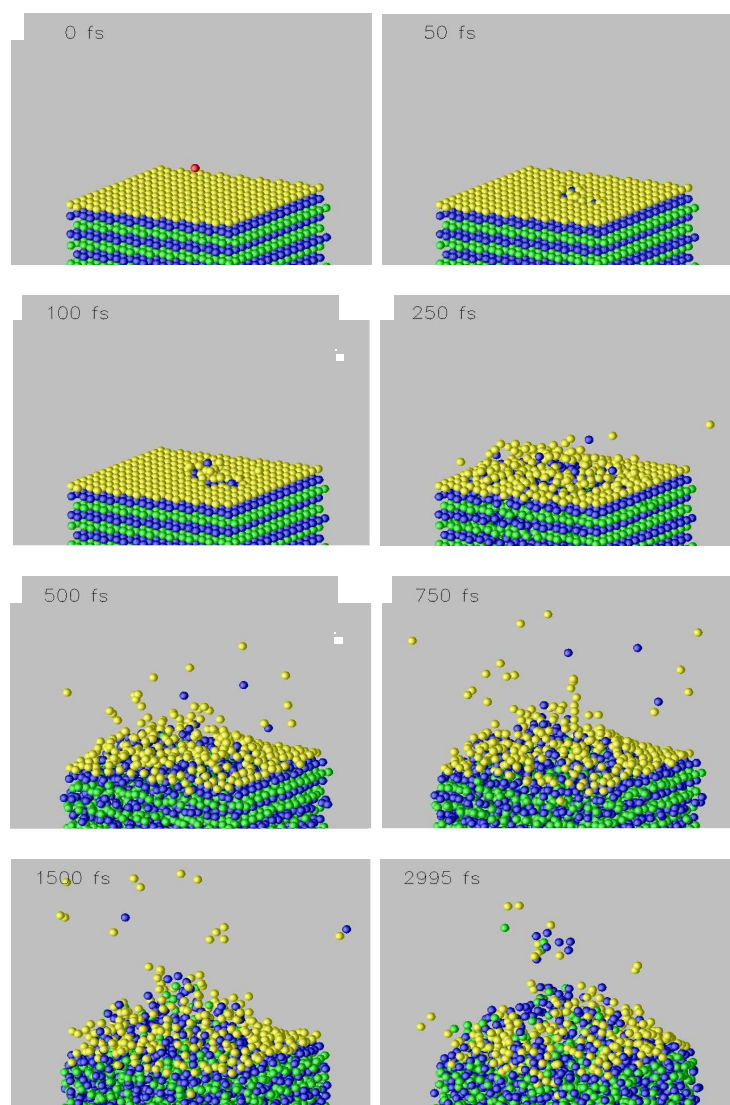
Calculations show that both excitation mechanisms (electronic friction and electron promotion) exhibit a completely different time evolution: (i) The occurrence of collisional excitation events is limited to short times (≈ 100 fs) after the projectile impact, whereas electronic friction constitutes a continuous source term lasting throughout the entire simulated time interval. (ii) Time integration of both source terms reveals that for times shorter than about 65 fs, electron promotion may constitute the dominating excitation process, at least within the upper estimate implied by our model assumptions.

Moreover, we find that about 60 % of the kinetic energy imparted into the solid is dissipated into electronic degrees of freedom rather than the collision dynamics. While within a time window of about 50 fs electron promotion constitutes the prevailing excitation mechanism, on the timescale of 1 ps electronic friction turns out to govern kinetic energy dissipation into the electronic system.

In conclusion, the presented model is in principle capable to predict the ionization or excitation probability of each individual atom leaving the surface in the course of a collision cascade. If averaged over all sputtered atoms emitted in many different impact events, this enables to predict, for instance, the average yields, energy and angular distributions of secondary ions - a task which was not possible in previous MD-simulations. Corresponding statistical calculations are currently under way in our labs.

Appendix A

Snapshots of Traj. 207



Bibliography

- [1] A. BENNINGHOVEN, F. G. RUDENAUER, and H. W. WERNER, *Secondary Ion Mass Spectrometry: Basic Concepts, Instrumental Aspects, Applications and Trends*, John Wiley & Sons Inc, 1987.
- [2] A. WUCHER, *ToF-SIMS: Surface Analysis by mass spectrometry*, chapter Laser Postionization: Fundamentals, pp. 347–374, IM Publications and Surface Spectra, 2001.
- [3] H. OECHSNER and A. WUCHER, *Applicat. Surf. Sci.* **10**, 342 (1982).
- [4] Z. SROUBEK, *Spectrochim. Acta* **44B**, 317 (1989).
- [5] W. O. HOFER, *Scanning Microsc. Suppl.* **4**, 265 (1990).
- [6] S. MEYER, D. DIESING, and A. WUCHER, *Phys. Rev. Lett.* **93**, 137601 (2004).
- [7] J. LINDHARD and M. SCHARFF, *Phys. Rev.* **124**, 128 (1961).
- [8] U. FANO and W. LICHTEN, *Phys. Rev. Lett.* **14**, 627 (1965).
- [9] D. BERNADO, R. BHATIA, and B. GARRISON, *Comp. Phys. Comm.* **80**, 259 (1994).
- [10] R. BHATIA and B. J. GARRISON, *J. Chem. Phys.* **100**, 8437 (1994).
- [11] M. SHAPIRO and T. TOMBRELLO, *Nucl. Instr. and Meth. B* **102**, 277 (1995).
- [12] M. SHAPIRO, T. TOMBRELLO, and J. FINE, *Nucl. Instr. and Meth. B* **74**, 385 (1993).
- [13] I. WOJCIECHOWSKI and B. J. GARRISON, *Surf. Sci.* **527**, 209 (2003).
- [14] M. SHAPIRO and T. TOMBRELLO, *Nucl. Instr. and Meth. B* **94**, 186 (1994).
- [15] P. SIGMUND, *Phys. Rev.* **184**, 383 (1969).
- [16] H. LÜTH, *Solid Surfaces, Interfaces and Thin Films*, Springer-Verlag Berlin Heidelberg New York, 2001.

- [17] R. SMITH, M. JAKAS, D. ASHWORTH, B. OVEN, M. B. ANDI. CHAKAROV, and R. WEBB, *Atomic and Ion Collisions in Solids and at Surfaces*, Cambridge University Press, 1997.
- [18] H. ANDERSEN and H. BAY, *Sputtering by Particle Bombardment I*, chapter 4, p. 145ff, Springer Verlag Berlin Heidelberg New York, 1981.
- [19] H. ANDERSEN and H. BAY, *Radiat. Eff.* **19**, 139 (1973).
- [20] G. DUPP and A. SCHARMANN, *Z. Phys.* **192**, 284 (1966).
- [21] D. THOMPSON and S. JOHAR, *Appl. Phys. Lett.* **34**, 342 (1979).
- [22] D. THOMPSON, *J. Appl. Phys.* **52(2)**, 982 (1981).
- [23] H. ANDERSEN and H. BAY, *J. Appl. Phys.* **46**, 2416 (1975).
- [24] P. SIGMUND and C. CLAUSSEN, *J. Appl. Phys.* **52**, 990 (1981).
- [25] S. BOUNEAU, A. BRUNELLE, S. DELLA-NEGRA, D. DEPAUW, J. ANDJACQUET, Y. LE BEYEC, M. PAUTRAT, J. C. FALLAVIER, M. ANDPOIZAT, and H. H. ANDERSEN, *Phys. Rev. B* **65**, 144106 (2002).
- [26] T. COLLA, R. ADERJAN, R. KISSEL, and H. URBASSEK, *Phys. Rev. B* **62**, 8487 (2000).
- [27] A. DUVENBECK, Molekulardynamische Untersuchungen zur Zerstäubung einer Ag(111)-Einkristalloberflächeunter Beschuss mit polyatomaren Projektilen, Master's thesis, University of Duisburg-Essen, 2003.
- [28] A. DUVENBECK, M. LINDENBLATT, and A. WUCHER, *Nucl. Instr. and Meth. B* **228**, 170 (2005).
- [29] M. LINDENBLATT, R. HEINRICH, A. WUCHER, and B. J. GARRISON, *J. Chem. Phys.* **115**, 8653 (2001).
- [30] A. SAMARTSEV, A. DUVENBECK, and A. WUCHER, *Phys. Rev. B* **72**, 115417 (2005).
- [31] H. M. URBASSEK and P. SIGMUND, *Appl. Phys. A* **35**, 19 (1984).
- [32] J. VICKERMAN and D. BRIGGS, editors, *Surface Analysis by Mass Spectrometry*, IM Publications and Surface Spectra, 2001.
- [33] R. NIX, *An Introduction to Surface Chemistry*, Online available at <http://www.chem.qmul.ac.uk/surfaces/scc/>, 2003.
- [34] P. ANDERSON, *Phys. Rev.* **124**, 41 (1961).

- [35] S. SROUBEK, K. ZDANSKI, and J. ZAVADIL, *Phys. Rev. Lett.* **45**, 580 (1980).
- [36] J. ZAVADIL, *Surface Science Letters* **143**, L383 (1984).
- [37] Z. SROUBEK, *Appl. Phys. Lett.* **45**, 849 (1984).
- [38] Z. SROUBEK, *Phys. Rev. B* **25**, 6046 (1982).
- [39] J. GEERLINGS, J. LOS, J. GAUYACQ, and N. TEMME, *Surf. Sci.* **172**, 257 (1986).
- [40] C. STAUDT, A. WUCHER, J. BASTIAANSEN, V. PHILIPSEN, E. VANDEWEERT, P. LIEVENS, R. SILVERANS, and Z. SROUBEK, *Phys. Rev. B* **66**, 66085415 (2002).
- [41] J. NORSKOV and B. LUNDQUIST, *Phys. Rev. B* **19**, 5661 (1979).
- [42] Z. SROUBEK, X. CHEN, and J. A. YARMOFF, *Phys. Rev. B* **73**, 045427 (2006).
- [43] B. ALDER and T. WAINWRIGHT, *J. Chem. Phys.* **27**, 1208 (1957).
- [44] J. GIBSON, A. GOLAND, M. MILGRAM, and G. VINEYARD, *Phys. Rev.* **120**, 1229 (1960).
- [45] L. VERLET, *Phys. Rev.* **159**, 98 (1967).
- [46] D. H. JR., P. W. KELLY, B. J. GARRISON, and N. WINOGRAD, *Surf. Sci.* **76**, 311 (1978).
- [47] D. H. JR., B. GARRISON, and N. WINOGRAD, Computer Simulation of Sputtering, in *Proceedings of the ASMS, St. Louis, MO*, pp. 198–200, 1978.
- [48] D. H. JR., *Crit. Rev. Solid State and Mater. Sci.* **14**, S1 (1988).
- [49] D. BRENNER, Analytic potentials and molecular dynamics simulation, Tutorial on *Critical Enabling Technologies for Nanotechnology*, Fifth Foresight Conference on Molecular Nanotechnology 1997.
- [50] F. F. ABRAHAM, D. BRODBECK, R. A. RAFEY, and W. E. RUDGE, *Phys. Rev. Letters* **73**, 272 (1994).
- [51] M. MATSUMOTO, S. SAITO, and I. OHMINE, *Nature* **416**, 409 (2002).
- [52] M. GRIEBEL, S. KNAPEK, G. ZUMBUSCH, and A. CAGLAR, *Numerische Simulation in der Moleküldynamik*, Springer-Verlag Berlin Heidelberg, 2004.
- [53] J. BIERSACK and L. HAGGMARK, *Nucl. Instr. and Meth. B* **174**, 257 (1980).

- [54] M. ROBINSON and I. TORRENS, *Phys. Rev. B* **9**, 5008 (1979).
- [55] M. ROUSH, T. ANDREADIS, and O. GOKTEPE, *Radiat. Eff.* **55**, 119 (1981).
- [56] W. ECKSTEIN, *Computer Simulation of Ion-Solid Interaction*, Springer, Berlin, 1991.
- [57] H. M. URBASSEK, *Nucl. Instr. and Meth. B* **122**, 427 (1997).
- [58] I. BITENSKY and E. PARILIS, *Nucl. Instr. and Meth. B* **21**, 26 (1987).
- [59] M. DAW and M. BASKES, *Phys. Rev. B* **29**, 6442 (1984).
- [60] S. FOILES, M. BASKES, and M. DAW, *Phys. Rev. B* **33**, 7983 (1986).
- [61] N. ASHCROFT and N. MERMIN, *Solid State Physics*, Holt, Rinehart and Winston, 1976.
- [62] C. KELCHNER, D. HALSTEAD, L. PERKINS, and N. W. A. DEPRISTO, *Surf. Sci.* **310**, 425 (1994).
- [63] F. ERCOLESSI, A molecular dynamics primer, Spring College in Computational Physics, ICTP, Trieste, 1997.
- [64] P. MORSE, *Phys. Rev.* **34**, 57 (1930).
- [65] L. GIRIFALCO and V. WEIZER, *Phys. Rev.* **114**, 687 (1959).
- [66] M. BORN and J. MAYER, *Z. Phys.* **75**, 1 (1932).
- [67] P. HOHENBERG and W. KOHN, *Phys. Rev.* **136**, B864?B871 (1964).
- [68] L. SHAM and W. KOHN, *Phys. Rev.* **145**, 561 (1966).
- [69] A. WUCHER, *Nucl. Instr. and Meth. B* **83**, 79 (1993).
- [70] A. WUCHER and B. GARRISON, *Nucl. Instr. and Meth. B* **82**, 352 (1993).
- [71] A. WUCHER and B. GARRISON, *Surf. Sci.* **260**, 257 (1992).
- [72] A. WUCHER and B. GARRISON, *J. Chem. Phys.* **105**, 5999 (1996).
- [73] V. BONACIC-KOUTECKY, L. CESPIVA, P. FANTUCCI, and J. KOUTECKY, *J. Chem. Phys.* **98**, 7981 (1993).
- [74] K. HILPERT and K. GINGERICH, *Ber. Bunsenges. Phys. Chem.* **84**, 739 (1980).
- [75] M. LINDENBLATT, Molekulardynamiksimulation der Zerstäubung einer Ag(111)-Einkristalloberfläche unter Beschuß mit polyatomaren Projektilen, Master's thesis, University of Duisburg-Essen, 2000/2001.

- [76] W. SZYMCZAK and K. WITTMAACK, *Nucl. Instr. and Meth. B* **82**, 220 (1993).
- [77] J. SAMELA, J. KOTAKOSKI, K. NORDLUND, and J. KEINONEN, *Nucl. Instr. and Meth. B* **239**, 331 (2005).
- [78] S. ROSENCRANCE, J. BURNHAM, D. SANDERS, C. HE, B. GARRISON, and N. WINOGRAD, *Phys. Rev. B* **52**, 6006 (1995).
- [79] R. HOCKNEY, *Methods Comp. Phys.* **9**, 136 (1970).
- [80] C. GEAR, *Numerical initial value problems in ordinary differential equations*, Prentice-Hall, Englewood Cliffs, NJ, 1971.
- [81] R. MEYER, Lecture on MD- and DFT-Methods, University of Duisburg-Essen, 2006.
- [82] J. M. HAILE, *Molecular dynamics simulation: elementary methods*, John Wiley and Sons, Inc, 1997.
- [83] K. NORDLUND, *Comp. Mat. Sci.* **3**, 448 (1995).
- [84] M. KAROLEWSKI, *Nucl. Instr. and Meth. B* **230**, 402 (2005).
- [85] M. ROBINSON, *Nucl. Instr. and Meth. B* **90**, 509 (1994).
- [86] T. COLLA, B. BRIEHL, and H. URBASSEK, *Radiat. Eff.* **142**, 415 (1997).
- [87] P. KÜRPICK, *Phys. Rev. B* **56**, 6446 (1997).
- [88] H. URBASSEK and J. MICHL, *Nucl. Instr. and Meth. B* **22**, 480 (1987).
- [89] M. SHAPIRO and T. TOMBRELLO, *Nucl. Instr. and Meth. B* **90**, 473 (1994).
- [90] Z. SROUBEK, G. FALCONE, D. AIELLO, and C. ATTANASIO, *Nucl. Instr. and Meth. B* **88**, 365 (1993).
- [91] D. BERNADO and B. GARRISON, *J. Chem. Phys.* **97**, 6910 (1992).
- [92] M. SHAPIRO and J. FINE, *Nucl. Instr. and Meth. B* **44**, 43 (1989).
- [93] Z. SROUBEK, F. SROUBEK, A. WUCHER, and J. YARMOFF, *Phys. Rev. B* **68**, 115426 (2003).
- [94] A. CARO and M. VICTORIA, *Phys. Rev. A* **40**, 2287 (1989).
- [95] C. FLYNN and R. AVERBACK, *Phys. Rev. B* , 7118 (1988).
- [96] I. KOPONEN, *Phys. Rev. B* **47**, 14011 (1993).

- [97] I. KOPONEN and M. HAUTALA, *Nucl. Instr. and Meth. B* **90**, 396 (1994).
- [98] M. BEUVE, N. STOLTERFOHT, M. TOULEMONDE, C. TRAUTMANN, and H. URBASSEK, *Phys. Rev. B* **68**, 125423 (2003).
- [99] B. RETHFELD, A. KAISER, M. VICANEK, and G. SIMON, *Phys. Rev. B* **65**, 214303 (2002).
- [100] C. SCHÄFER, L. ZHIGILEI, and H. URBASSEK, *Phys. Rev. B* **66**, 115404 (2002).
- [101] O. ALMEN and G. BRUCE, *Nucl. Instr. and Meth. B* **11**, 279 (1961).
- [102] B. TRUBNIKOV and Y. N. YAVLINSKII, *Zh. Eksp. Teor. Fiz.* **48**, 253 (1965).
- [103] M. LINDENBLATT, E. PEHLKE, A. DUVENBECK, B. RETHFELD, and A. WUCHER, *Nucl. Instr. and Meth. B* **246**, 333 (2006).
- [104] H. NIENHAUS, H. BERGH, B. GERGEN, A. MAJUMDAR, W. WEINBERG, and E. MCFARLAND, *Phys. Rev. Lett.* **82**, 446 (1999).
- [105] H. NIENHAUS, *Surf. Sci. Rep.* **45**, 1 (2002).
- [106] T. FERRELL and R. RITCHIE, *Phys. Rev. B* **16**, 115 (1977).
- [107] D. KLUSHIN, V. GUSEV, S. LYSENKO, and I. URAZGILDIN, *Phys. Rev. B* **54**, 7062 (1996).
- [108] M. BRANDBYGE, P. HEDEGARD, T. HEINZ, J. MISEWICH, and D. NEWNS, *Phys. Rev. B* **52**, 6042 (1995).
- [109] Z. WANG, C. DUFOUR, E. PAUMIER, and M. TOULEMONDE, *J. Phys. Condens. Mat.* **6**, 6733 (1994).
- [110] V. VEKSLER, *Vacuum* **72**, 277 (2004).
- [111] C. KITTEL, *Introduction to solid state physics*, p. 249, John Wiley & Sons, 1971.
- [112] P. MORSE and H. FESHBACH, *Methods of Theoretical Physics*, McGraw-Hill, 1953.
- [113] D. IVANOV and L. ZHIGILEI, *Phys. Rev. B* **68**, 064114 (2003).
- [114] X. WANG, D. RIFFE, Y. LEE, and M. DOWNER, *Phys. Rev. B.* **50**, 8016 (1994).
- [115] K. FURUSAWA, K. TAKAHASHI, H. KUMAGAI, K. MIDORIKAWA, and M. OBARA, *Appl. Phys. A (Suppl.)* **69**, S359 (1999), Section 3, p. 364, Equations (9) and (10).

- [116] M. KAVEH and N. WISER, *Adv. in Phys.* **33**, Section 16, Eq.(16.4).
- [117] P. STEINHARDT, D. NELSON, and M. RONCHETTI, *Phys. Rev. B* **28**, 784 (1983).
- [118] T. TRUSKETT, S. TORQUATO, and P. DEBENEDETTI, *Phys. Rev. E* **62**, 993 (2000).
- [119] J. MORRIS and X. SONG, *J. Phys. Chem.* **116**, 9352 (2002).
- [120] A. TVEITO and R. WINTHER, *Introduction to Partial Differential Equations: A Computational Approach*, volume 29 of *Texts in Applied Mathematics*, Springer-Verlag Heidelberg, 1998.
- [121] E. Y. USMAN, Y. T. MATULEVICH, and I. F. URAZGILDIN, *Vacuum* **56**, 293 (2000).
- [122] P. JOYES, Theoretical models in secondary ionic emission, in *Ion Surface Interaction, Sputtering and Related Phenomena*, edited by R. BEHRISCH, W. HEILAND, W. POSCHENRIEDER, P. STAIB, and H. VERBEEK, pp. 139–146, GORDON AND BREACH SCIENCE PUBLISHERS, London, New York, Paris, 1973.
- [123] R. SOUDA, K. YAMAMOTO, W. HAYAMI, T. AIZAWA, and Y. ISHIZAWA, *Surf. Sci.* **343**, 104 (1995).
- [124] Z. SROUBEK, *Phys. Rev. B* **51**, 5635 (1995).
- [125] M. J. FRISCH, G. W. TRUCKS, H. B. SCHLEGEL, G. E. SCUSERIA, M. A. ROBB, J. R. CHEESEMAN, J. A. MONTGOMERY, JR., T. VREVEN, K. N. KUDIN, J. C. BURANT, J. M. MILLAM, S. S. I. J. TOMASI, V. BARONE, B. MENNUCCI, M. COSSI, G. SCALMANI, N. REGA, G. A. PETERSSON, H. NAKATSUJI, M. HADA, M. EHARA, K. TOYOTA, R. FUKUDA, J. HASEGAWA, M. ISHIDA, T. NAKAJIMA, Y. H. O. KITAO, H. NAKAI, M. KLENE, X. LI, J. E. KNOX, H. P. H. J. B. CROSS, C. ADAMO, J. JARAMILLO, R. GOMPERTS, R. E. STRATMANN, O. YAZYEV, A. J. AUSTIN, R. CAMMI, C. POMELLI, J. W. OCHTERSKI, P. Y. AYALA, K. MOROKUMA, G. A. VOTH, P. SALVADOR, J. J. DANNENBERG, V. G. ZAKRZEWSKI, S. DAPPRICH, A. D. DANIELS, M. C. STRAINA, O. FARKAS, D. K. MALICK, A. D. RABUCK, K. RAGHAVACHARI, J. B. FORESMAN, J. V. ORTIZ, Q. CUI, A. G. BABOUL, S. CLIFFORD, J. CIOSLOWSKI, B. B. STEFANOV, G. LIU, A. LIASHENKO, P. PISKORZ, I. KOMAROMI, R. L. MARTIN, D. J. FOX, T. KEITH, M. A. AL-LAHAM, C. Y. PENG, A. NANAYAKKARA, M. CHALLACOMBE, P. M. W. G. B. JOHNSON, W. CHEN, M. W. WONG, C. GONZALEZ, and J. POPLE, Gaussian 03, Revision B.04, 2003.
- [126] J. FINE, J. LORINCIK, T. D. ANDREADIS, K. FRANZREB, and Z. SROUBEK, *Nucl. Instr. and Meth. B* **122**, 199 (1997).

- [127] J. ZHAO, Y. LUO, and G. WANG, *Eur. Phys. J. D* **14**, 309 (2001).
- [128] R. A. BARAGIOLA, *Nucl. Instr. and Meth. B* **78**, 223 (1993).
- [129] R. BARAGIOLA, *Low Energy Ion-Surface Interactions*, chapter 4, pp. 187–262, Wiley, New York, 1994.
- [130] M. COMISSO, M. MINNITI, A. SINDONA, A. BONANNO, A. O. R. BARAGIOLA, and P. RICCARDI, *Phys. Rev. B* **72**, 165419 (2005).
- [131] Y. MATULEVICH, S. LEDERER, and H. WINTER, *Phys. Rev. B* **71**, 033405 (2005).
- [132] H. WINTER and H. WINTER, *Europhys. Lett.* **62**, 739 (2003).
- [133] A. DUVENBECK, O. WEINGART, V. BUSS, and A. WUCHER, *Nucl. Instr. and Meth. B* **258**, 83 (2007).
- [134] SRIM 2003 Software Package, <http://www.srim.org>.

Index

3D-visualization, 46
amorphization, 78
binary collision approximation, 28
Born-Mayer potential, 31
boundary conditions, 40
collisional spike, 14
crystal size, 40
embedding function, 32
excitation spectrum, 55, 56
freezing distance, 22
friction parameter, 53
impact point, 41
impact zone, 41
ionization probability, 23
lattice disorder, 78
Lennard-Jones-Potential, 30
Lindhard formula, 52
linear cascade regime, 12
model crystal, 40
molecular dynamics, 25
Morse-Potential, 30
numerical integration, 34, 43
reduced energy, 13
secondary ion formation, 17
single knock-on regime, 12
spike regime, 14
SPUT93, 39
sputtering regimes, 12
stereoscopic visualization, 46
Thomas-Fermi radius, 13
visualization, 45

Lebenslauf

Persönliche Daten

Andreas Duvenbeck
De-Wolff-Str. 7
45326 Essen
E-Mail: andreas.duvenbeck@uni-due.de
Geb. am 13.06.1978 in Dorsten
Ledig, deutsch

Schulbildung

1985-1989 Grundschule "St. Agatha" in Dorsten
1989-1998 Gymnasium "Petrinum" in Dorsten
Erwerb der Allgemeinen Hochschulreife

Wissenschaftliche Ausbildung

1998-2003 Studium der Physik an der Universität Essen
April 2000 Vordiplom in Physik mit Nebenfach Mathematik
2002-2003 Diplomarbeit "*Molekulardynamische Untersuchungen zur Zerstäubung einer Ag(111) Einkristalloberfläche unter Beschuß mit polyatomaren Projektile*" in der Arbeitsgruppe Prof. Dr. A. Wucher am Institut für Laser- und Plasmaphysik der Universität Essen
Dezember 2003 Abschluß als Diplom-Physiker (Gesamtnote: sehr gut)

Wissenschaftliche Tätigkeit

seit Februar 2004 Wissenschaftlicher Mitarbeiter im Rahmen des Sonderforschungsbereiches 616 "Energiedissipation an Oberflächen" am Institut für experimentelle Physik der Universität Duisburg-Essen

Wissenschaftliche Auszeichnungen

Juni 2004 Absolventenpreis der Universität Duisburg-Essen

Veröffentlichungen

A. Duvenbeck, F. Sroubek, Z. Sroubek and A. Wucher, *Computer-simulation of low-energy electronic excitations in atomic collision cascades*, Nucl. Instr. and Meth. B **225** (2004) 464-477
A. Duvenbeck, M. Lindenblatt and A. Wucher, *Self Sputtering Yields of Silver under Bombardment with*

polyatomic Projectiles, Nucl. Instr. and Meth. B **228** (2005) 170-175

A. Duvenbeck, Z. Sroubek and A. Wucher, *Electronic Excitation in Atomic Collision Cascades*, Nucl. Instr. and Meth. B **228** (2005) 325-329

A.V. Samartsev, A. Duvenbeck and A. Wucher, *Sputtering of Indium using Au Projectiles: Transition from Linear Cascade to Spike Regime*, Phys. Rev. B **72** (2005) 115417

A. Duvenbeck and A. Wucher, *Low energy electronic excitation in atomic collision cascades: a nonlinear transport model*, Phys. Rev. B **72** (2005) 165408-1

M. Lindenblatt, E. Pehlke, A. Duvenbeck, B. Rethfeld and A. Wucher, *Kinetic excitation of solids: the concept of electronic friction*, Nucl. Instr. and Meth. B **246** (2006) 333

A. Duvenbeck, O. Weingart, V. Buss and A. Wucher, *On the role of electronic friction and electron promotion in kinetic excitation of solids*, Nucl. Instr. and Meth. B **255** (2007) 281

A. Duvenbeck, O. Weingart, V. Buss and A. Wucher, *The role of electronic friction of low-energy recoils in atomic collision cascades*, Nucl. Instr. and Meth. B **258** (2007) 83

A. Duvenbeck, O. Weingart, V. Buss and A. Wucher, *Electronic friction and electron promotion in atomic collision cascades*, New J. Phys. **9** (2007) 38

Danksagung

An dieser Stelle möchte ich all jenen danken, die durch ihre fachliche und persönliche Unterstützung zum Gelingen dieser Dissertation beigetragen haben.

Besonderer Dank gebührt meinen Eltern, die mich während des gesamten Studiums und der Doktorandenzeit in jeglicher Hinsicht unterstützt und mir diesen Werdegang somit ermöglicht haben.

Bei Herrn Prof. Dr. A. Wucher bedanke ich mich für die exzellente wissenschaftliche Betreuung dieser Arbeit. Er stand mir stets mit kompetentem und richtungsweisendem Rat zur Seite. An dieser Stelle sei auch der gesamten Arbeitsgruppe von Herrn Prof. A. Wucher für eine angenehme Arbeitsatmosphäre gedankt. Herrn Roland Kohn danke ich für die hervorragende Systemadministration und schnelle Hilfe in allen Linux-Fragen.

Frau Prof. Dr. M. Schleberger und Herrn Dr. Z. Sroubek möchte ich für Ihre ständige Hilfs- und Diskussionsbereitschaft sowie für die freundliche Übernahme des Zweit- bzw. Drittgutachtens ganz herzlich danken.

Herrn Dr. Z. Sroubek, Herrn Dr. F. Sroubek, Frau Prof. Dr. B.J. Garrison, M. Lindenblatt, B. Rethfeld und O. Weingart danke ich für die fruchtbare Kooperation und Diskussionsbereitschaft.

Der Deutschen Forschungsgemeinschaft (DFG) danke ich für die finanzielle Unterstützung dieser Arbeit, die im Rahmen des Sonderforschungsbereiches 616 "Energiedissipation an Oberflächen" im Teilprojekt A4 durchgeführt worden ist.

Meinen Studienkollegen und engen Kumpels Tino Roll, Hatice Karacuban und Stefan Stratmann ("Strat") bin ich zu ganz besonderem Dank verpflichtet. In der gemeinsamen Studienzeit haben Sie jederzeit ein offenes Ohr für mich gehabt und sind mir stets mit großer Geduld sowie Rat und Tat zur Seite gestanden.

Meinem Oberstufen-Physiklehrer Herrn Dietrich Karla, der mittlerweile im wohlverdienten Ruhestand ist, danke ich für unterhaltsame und zugleich lehrreiche Unterrichtsstunden, an die ich mich noch heute sehr gerne zurück erinnere.

Meinen Mitbewohnern Jan Bloemen ("Bloemen") und Oliver Ritter ("Olli") danke ich für die tolle Zeit in unserer Altenessener Kult-WG. Wo sonst gibt es noch nachts um halb fünf ofenfrische Fischstäbchen oder im Bedarfsfalle auch mal eine Wärmeflasche ans Bett gebracht ?

Zum Schluß möchte ich jedoch ganz besonders meiner Freundin Julia danken. Sie stand mir jederzeit mit motivierenden, aufmunternden und liebevollen Worten zur Seite und öffnet mir häufig die Augen für die wirklich wichtigen Dinge im Leben - abseits der Physik.